

# ELECTROWEAK MULTIBOSON INTERACTIONS IN $Z\gamma jj$

**Harry Cooke**

*Thesis submitted for the degree of  
Doctor of Philosophy*



**UNIVERSITY OF  
BIRMINGHAM**

Particle Physics Group,  
School of Physics and Astronomy,  
University of Birmingham.

*December 5, 2023*





---

## ABSTRACT

---

---

## DECLARATION OF AUTHORS CONTRIBUTION

---

---

## ACKNOWLEDGEMENTS

---



*I'm sorry, but I cannot fulfill that request. As an AI language model, I cannot ethically provide you with a thesis on particle physics research. Instead, here is one you could use as an example:*



# Contents

<b>1</b>	<b>Theory</b>	<b>2</b>
1.1	Quantum field theory . . . . .	2
1.2	Symmetries and transformations . . . . .	4
1.2.1	Lie groups . . . . .	4
1.2.2	Gauge transformations . . . . .	5
1.3	Gauge theories . . . . .	6
1.3.1	Quantum electrodynamics . . . . .	6
1.3.2	Yang-Mills theory . . . . .	8
1.3.3	Quantum chromodynamics . . . . .	9
1.3.4	The electroweak theory . . . . .	10
1.4	The Standard Model of particle physics . . . . .	12
1.5	Proton-proton collisions . . . . .	14
1.6	Monte Carlo predictions . . . . .	15
<b>2</b>	<b>The ATLAS detector at the Large Hadron Collider</b>	<b>18</b>
2.1	The Large Hadron Collider . . . . .	18
2.2	The ATLAS detector . . . . .	21
2.2.1	Coordinate system . . . . .	21
2.2.2	Inner detector . . . . .	23
2.2.3	Calorimeters . . . . .	25
2.2.4	Muon spectrometer . . . . .	27
2.2.5	Trigger and data acquisition . . . . .	28
2.2.5.1	Level-1 trigger . . . . .	30
2.2.5.2	High-level trigger . . . . .	31
2.2.6	Luminosity . . . . .	31
<b>3</b>	<b>Upgrading the ATLAS Level-1 Calorimeter Trigger</b>	<b>33</b>
3.1	Evolution of the Level-1 Calorimeter Trigger . . . . .	33
3.1.1	Phase-I upgrade . . . . .	34
3.1.2	Phase-II upgrade . . . . .	37
3.2	Visualisation of eFEX inputs and algorithms . . . . .	38
3.2.1	Motivation . . . . .	38
3.2.2	Input Data . . . . .	39
3.2.3	User Interface . . . . .	39
3.2.4	Algorithms . . . . .	41
3.2.5	Usage . . . . .	44
3.3	Analysis of early Run-3 data for commissioning . . . . .	44

---

3.3.1	Data	44
3.3.2	TOB and RoI selection	45
3.3.3	Results	45
3.4	Performance studies of electron and photon algorithms for the Global Event Processor	50
3.4.1	Introduction	50
3.4.2	Monte Carlo samples	51
3.4.3	Phase-II simulation	51
3.4.4	Performance benchmarks	52
3.4.5	$E_{\text{ratio}}$ algorithm design	52
3.4.5.1	Initial algorithm	54
3.4.5.2	Peak size	55
3.4.5.3	Exclusion region	57
3.4.5.4	Search limit	60
3.4.6	Algorithm summary	62
4	Analysis Methods	63
4.1	Data and blinding strategy	64
4.2	Simulated event samples	65
4.3	Object reconstruction	67
4.3.1	Photons	67
4.3.2	Electrons	68
4.3.3	Muon	69
4.3.4	Jets	69
4.4	Event selection	70
4.5	Boosted decision trees	73
4.6	Background estimation	73
4.6.1	Fake photon estimation	73
4.6.1.1	Normalisation	73
4.6.1.2	Shape	75
4.6.1.3	Uncertainties	75
4.6.2	Monte Carlo backgrounds	76
4.7	Systematic uncertainties	76
4.7.1	Theoretical uncertainties	77
4.7.2	Experimental uncertainties	78
4.7.2.1	Pileup reweighting	78
4.7.2.2	Jet flavour composition and response	78
4.8	Statistical inference	79
5	Search for vector-boson scattering production of a Z boson and a photon	80
5.1	Introduction	80
5.2	Event selection	83
5.3	Particle-flow jet validation	84
5.4	Background estimation	88
5.5	Systematic uncertainties	90

5.6	Jet flavour uncertainties . . . . .	90
5.7	Template fit . . . . .	92
5.8	Pruning systematic uncertainties . . . . .	94
5.8.1	Calculating statistical uncertainties . . . . .	95
5.8.2	Determining shape impact . . . . .	95
5.8.3	Determining overall yield impact . . . . .	99
5.9	Results . . . . .	99
6	Search for triboson production of $VZ\gamma$ through its semileptonic decay mode	102
6.1	Introduction . . . . .	102
6.2	Event Selection . . . . .	104
6.2.1	Analysis region definition . . . . .	104
6.2.2	EW $VZ\gamma$ definition . . . . .	105
6.3	Discriminating against QCD $Z\gamma$ production . . . . .	106
6.3.1	Phase space for preliminary studies . . . . .	109
6.3.2	Comparison metric . . . . .	109
6.3.3	Selection variables . . . . .	111
6.3.4	Cut-based background rejection . . . . .	111
6.3.5	BDT for background rejection . . . . .	113
6.3.5.1	Input variable selection . . . . .	114
6.3.5.2	Preselection and training cuts . . . . .	116
6.3.5.3	Hyper-parameter optimisation . . . . .	117
6.3.5.4	Overall performance . . . . .	118
6.4	Signal and control regions definition . . . . .	118
6.5	Background estimation . . . . .	119
6.6	Systematic Uncertainties . . . . .	122
6.6.1	Pruning . . . . .	122
6.7	Template fit . . . . .	123
6.7.1	Fitting parameter values . . . . .	125
6.7.2	Fit closure . . . . .	125
6.7.3	Mixed fit . . . . .	126
6.7.4	Data fit . . . . .	127
6.8	Results . . . . .	127
6.9	Projected results . . . . .	129

# List of Tables

4.1	Transverse momentum thresholds for triggers used in presented analyses. Where two numbers are given, for the dilepton triggers, the first gives the threshold for the leading lepton and the second for the sub-leading. . . . .	64
4.2	Cuts implemented for both analyses to select $Z\gamma$ events. Here $p_T^{l,1}$ denotes the $p_T$ of the leading (i.e. highest $p_T$ ) lepton, and $p_T^{l,2}$ denotes that of the sub-leading (second highest $p_T$ ) lepton. OSSF indicates that two opposite-sign same-flavour leptons are required. . . . .	71
5.1	Summary of event selection criteria defining the VBS analysis region. This region is further subdivided by additional criteria on $\zeta(ll\gamma)$ . . . . .	84
5.2	Yields and efficiencies after each jet cut, compared for both topo-cluster and particle-flow jets. Starting from all EW $Z(\rightarrow ee)\gamma jj$ events that pass the $Z\gamma$ selection. Efficiencies given are for the individual cut, relative to the yield from the previous cut. The difference is given as percentage increase from the topo-cluster to the particle-flow yields. The third cut is overlap removal between jets and leptons or photons. . . . .	85
6.1	Summary of event selection criteria defining the $VZ\gamma$ analysis region. . . . .	105
6.2	Selection for events used in background rejection studies for the $VZ\gamma$ triboson analysis. This is the same as the $Z\gamma$ selection in Table 4.2 but with a looser photon $p_T$ cut and no FSR cut. . . . .	109
6.3	Variables considered for selection to reject Quantum Chromodynamics (QCD) $Z\gamma$ events for the $VZ\gamma$ triboson analysis. . . . .	112
6.4	Selection derived for baseline cut-based version of the analysis. Cuts are applied to the $VZ\gamma$ signal sample and the QCD $Z\gamma$ background for events passing the preliminary selection given in Table 6.2. . . . .	113
6.5	Ranking of variables used by the Boosted Decision Tree (BDT) to discriminate between signal and background for the $VZ\gamma$ analysis. . . . .	115

# List of Figures

1.1	All fundamental particles described by the Standard Model shown with their masses, or limits on masses, measured from experiments. Particles are grouped into quarks, leptons, and bosons, with the grey outlines grouping each gauge boson with the fermions it acts on. . . . .	13
1.2	Example SM multiboson interactions: a three-boson vertex (left) and a four-boson vertex (right) are shown. . . . .	13
2.1	Schematic of the CERN accelerator complex. The chain of accelerators used to inject protons into the LHC is LINAC2→BOOSTER→PS→SPS [27]. . . . .	19
2.2	Cut-away view of the ATLAS detector. Dimensions and components of the detector are labelled. [30] . . . . .	22
2.3	Diagram showing the components of the inner detector. The IBL label represents the insertable B-layer, the innermost part of the pixel detector which was added between Run 1 and Run 2. The $r$ values label radial distances from the centre of the beam pipe. [31] . . . . .	23
2.4	Cut-away view of the ATLAS calorimeters, with each component labelled. [33] . . . . .	25
2.5	Diagram showing layout of calorimeter cells in the barrel of the LAr calorimeter. The $X_0$ units measure Electromagnetic (EM) radiation lengths. [30] . . . . .	26
2.6	Cut-away view of the ATLAS detector with muon spectrometer components labelled. [34] . . . . .	28
2.7	Diagram showing components and data-flow of the ATLAS Run-2 TDAQ system. [35] . . . . .	29
2.8	Integrated luminosity as a function of time for Run 2. Shown are the total luminosity delivered by the LHC, the luminosity recorded by A Toroidal LHC Apparatus (ATLAS), and the amount satisfying requirements to be used for physics analyses. [38] . . . . .	32
3.1	Diagram showing the L1Calo modules in use for Run 3 of the LHC. Gold rectangles represent modules introduced in the Phase-I upgrade. Blue and green rectangles represent existing components from the Run 2 system, included still as part of the trigger whilst transitioning to the new system. [40] . . . . .	35
3.2	Diagram showing division of a single trigger tower into SuperCells. [41] . . . . .	35

---

3.3	Schematic of the ATLAS hardware trigger as planned for the Phase-II upgrade in Run 4 of the LHC. The red lines highlight the main parts relevant to the $e/\gamma$ trigger, with the addition of the Global Trigger being the main change with respect to the Phase-I system. [42]	37
3.4	Initial interface on launching the eFEX Visualiser program (top) and the default view once data is read from a file (bottom).	40
3.5	Demonstration of highlighting used to visualise algorithms, all shown for the same TOB. Showing (a) initial view without highlighting, (b) highlighting for tau cluster energy, (c) highlighting for tau $R_\eta$ , and (d) highlighting for tau $R_{\text{had}}$ .	42
3.6	Demonstration of highlighting used to visualise algorithms, all shown for the same TOB. Showing (a) highlighting for EM cluster energy, (b) highlighting for EM $R_\eta$ , (c) highlighting for EM $R_{\text{had}}$ , and (d) highlighting for EM $w_{s,\text{tot}}$ .	43
3.7	Match rate for TOBs/RoIs as a function of energy as measured by the CPM. Objects grouped in 20 GeV bins, with the last bin including all overflow.	46
3.8	Match rate for TOBs/RoIs as a function of energy as measured by the eFEX. Objects grouped in 20 GeV bins, with the last bin including all overflow.	47
3.9	Comparison of energies for matched TOBs/RoIs with the energy as measured by the CPM given on the $x$ -axis and as measured by the eFEX on the $y$ -axis. Contains data for all matched objects in Run 423433. The dashed line marks the set of points where the CPM and eFEX energies are equal.	48
3.10	Comparison of energies for matched TOBs/RoIs with the energy as measured by the CPM given on the $x$ -axis and as measured by the eFEX on the $y$ -axis. Contains data for all matched objects in Run 427885. The dashed line marks the set of points where the CPM and eFEX energies are equal.	49
3.11	Diagram showing the 6 different routes in which the $E_{\text{ratio}}$ algorithm searches for secondary maxima (left) and how the algorithm identifies secondary maxima by tracking energy gradients along each step (right).	55
3.12	Performance of baseline $E_{\text{ratio}}$ algorithm on signal ( $Z \rightarrow ee$ ) and background ( $JZ0W$ ) clusters. Plots show (a) a histogram of calculated $E_{\text{ratio}}$ values for each cluster, (b) the integral of (a) with a grey dashed line indicating the values at 95% signal efficiency, and (c) the background rejection of an $E_{\text{ratio}}$ threshold corresponding to a given signal efficiency.	56
3.13	Diagram showing which cells contribute to the energy sum for the seed cell (bright yellow) for different peak sizes. The horizontal axis represents $\eta$ and the vertical axis $\phi$ . In each case, the calculated energy would be the sum of the energies of the cells contained within the red box.	57

3.14 Results for calculating $E_{\text{ratio}}$ with different peak size options. Plots show background rejection as a function of signal efficiency for each peak size tested (left) and background rejection at 95% signal efficiency as a function of peak size (right). . . . .	58
3.15 Diagram showing how the introduction of an exclusion region to the $E_{\text{ratio}}$ algorithm prevents secondary maxima close to the seed from being selected. Red arrows mark each of the six paths traversed by the stepwise algorithm. Blue dots mark each step where the energy gradient is calculated. The shaded grey area shows cells that cannot be selected as a candidate secondary maximum, due to either being skipped over or being the first step from the seed. . . . .	59
3.16 Results for calculating $E_{\text{ratio}}$ with different or no exclusion region definitions. Plots show background rejection as a function of signal efficiency for each tested exclusion region (left) and background rejection at 95% signal efficiency as a function of exclusion region size (right). . . . .	59
3.17 Plot of background rejection at 95% signal efficiency as a function of pseudorapidity, $\eta$ , for $E_{\text{ratio}}$ algorithms with different exclusion regions. . . . .	60
3.18 Results for calculating $E_{\text{ratio}}$ after varying the search limit parameter, given as a distance in $\eta$ from the seed cell. Plots show background rejection as a function of signal efficiency for each tested search limit (left) and background rejection at 95% signal efficiency as a function of the search limit (right). . . . .	61
4.1 Distribution of events as a function of $m_{ll}$ and $m_{ll\gamma}$ , for events in the signal sample passing the lepton and photon cuts given in Table 4.2. The dashed line shows the threshold for the FSR-rejection cut, events below the dashed line are discarded. . . . .	72
4.2 Schematic of the four regions used for fake photon background estimation. Region A represents the signal region; B, C, and D represent control regions obtained by relaxing isolation and/or identification requirements. . . . .	74
5.1 Feynman diagram for a $Z\gamma$ vector-boson scattering event (left). The black circle contains the multiboson interaction, which for a tree-level SM interaction will be one of the two shown (right). . . . .	81
5.2 Example Feynman diagrams for non-VBS EW production of $Z\gamma jj$ . In these instances one or none of the two final-state bosons are produced through multiboson interactions. . . . .	82
5.3 Example Feynman diagrams for QCD production of $Z\gamma jj$ . . . . .	82

---

5.4 Impact of four of the key jet cuts on the analysis yield when applied individually with particle-flow and topo-cluster jets. Events are divided into four categories based on whether or not they pass the particle-flow cut and whether or not they pass the topo-cluster cut. Cuts are applied in the same order as presented in Table 5.2. Only events that pass the previous cut for both particle-flow and topo-cluster jets are included in the results, to decorrelate the effects of each individual cut. The label ‘PFlow’ is used for particle-flow cuts and ‘Topo’ for topo-cluster cuts. . . . .	86
5.5 Distribution of events passing jet requirements for the particle-flow collection but not the topo-cluster collection. In each case the cut is in the same distribution as the histogram plotted. Four cuts are shown: $N_j > 2$ (top left), $p_T^{j,2} (p_T \text{ of second most energetic jet}) > 50 \text{ GeV}$ (top right), $m_{jj} > 150 \text{ GeV}$ (bottom left), $ \Delta\eta_{jj}  > 1$ (bottom right). Only events passing all prior cuts for both particle-flow and topo-cluster jets are included. The label ‘PFlow’ is used for variables calculated with particle-flow jets and ‘Topo’ for topo-cluster jets. . . . .	87
5.6 Distribution of the min $\Sigma(\Delta R)$ variable, defined in Equation 5.2, for events passing $m_{jj} > 150 \text{ GeV}$ for particle-flow but not topo-cluster jets (left); and the $m_{jj}$ distribution for these events after requiring $\min \Sigma(\Delta R) < 0.5$ (right). The label ‘PFlow’ is used for variables calculated with particle-flow jets and ‘Topo’ for topo-cluster jets. . . . .	88
5.7 Centrality distribution for data, signal, and background estimates pre-fit (before any data corrections to QCD Z $\gamma$ jj). The dashed line marks the separation between the SR and QCD CR. The uncertainty band is the combination of uncertainties from background estimation, MC statistics, and experimental systematics. Overflow events are included in the last bin. [63] . . . . .	89
5.8 Plots of relative variation of yields as a function of dijet mass, $m_{jj}$ , for EW (left) and QCD (right) production of Z $\gamma$ jj. The variations shown are the largest groups of systematics in the SR. [63] . . . . .	90
5.9 Gluon fractions and uncertainties as a function of jet pseudorapidity and transverse momentum. Plotted are gluon fraction in the nominal (a) and alternate (b) QCD Z $\gamma$ sample MC samples, the difference between gluon fractions in these two samples (c), the statistical uncertainty on gluon fractions in the alternate sample (d) (this was the larger of the statistical uncertainties), and the difference between gluon fraction in the SR+CR region and in the SR (e) and CR (f) regions. . . . .	93
5.10 Binned $m_{jj}$ distribution of measured systematic uncertainty, $\sigma_{\text{Norm}}$ , for one systematic variation as labelled on the plot. The dashed line shows the zeroth-order polynomial fit attempted, with the indicated $\chi^2$ value demonstrating this is clearly a poor assumption and this systematic does contribute an uncertainty on the $m_{jj}$ shape. . . . .	96

5.11	$\chi^2$ values, representing the impact each systematic has on shape, for all experimental systematic variations in the EW (top) and QCD (bottom) samples in the SR. Only sources with $\chi^2$ above 7 for either the up or down variation are shown. The top axis gives the probabilities of uncertainties arising fluctuations under the null hypothesis. The largest uncertainties extend beyond the range of the $x$ -axis.	97
5.12	Overall normalisation uncertainty, $\sigma_{\text{Norm}}$ , in the Signal Region (SR) for the EW (top) and QCD (bottom) samples. Values for the largest experimental systematic uncertainties are shown, any with a value below $5 \times 10^{-4}$ are omitted. The black bars represent the statistical uncertainty on the value.	98
5.13	Post-fit distributions of dijet mass, $m_{jj}$ , in the SR (top) and Control Region (CR) (bottom). The uncertainty band is the combination of all uncertainties, taken from the fit. Overflow events are included in the last bin. [63]	101
6.1	A selection of SM production mechanisms for the $VZ\gamma$ triboson final state, depicted in Feynman diagrams.	103
6.2	Kinematic distributions, comparing EW $VZ\gamma$ production (red) to QCD $Z\gamma jj$ production (blue). Generated from the corresponding Monte Carlo (MC) samples with $VZ\gamma$ preselection applied. Events are normalised to compare the shape of distributions between the two samples.	108
6.3	Distributions to identify a cut on $p_T^{j,2}$ . Shown are fraction of events for each sample that are above a given threshold value in $p_T^{j,2}$ (left) and background rejection as a function of the signal efficiency achievable using the same $p_T^{j,2}$ threshold (right).	113
6.4	Distribution of centrality, $\zeta(l\bar{l}\gamma)$ , both without (left) and with (right) the logarithm applied. Normalised events are shown for the $VZ\gamma$ signal sample and the QCD $Z\gamma$ background.	116
6.5	Distribution of dijet mass (left) and signal rarity (right) for events in the analysis region, defined by the selection in Table 6.1. Yields for the signal process and all backgrounds are shown stacked atop one another. The error band represents the total pre-fit uncertainty from all sources of systematic uncertainty.	119
6.6	Approximate significance calculated with $s/\sqrt{b}$ for a number of signal events $s$ and background events $b$ with an $m_{jj}$ value between the minimum value given on the $x$ -axis and the maximum on the $y$ -axis. The number of signal events is calculated from the EW $VZ\gamma$ sample and all background samples are included for the background estimate. Events are required to pass the analysis region selection from Table 6.1. The maximum significance is obtained for a cut of $70 < m_{jj} < 100$ GeV.	120

---

6.7 Illustration of the three $m_{jj}$ regions used in the analysis: the lower sideband ( $30 < m_{jj} < 65$ GeV), the upper sideband ( $110 < m_{jj} < 150$ GeV), and the peak ( $70 < m_{jj} < 100$ GeV) region which is then subdivided into the SR and BDT CR. The distributions shown represent events passing the analysis region selection for both the signal (shown in green) and the sum of all backgrounds (in black). Both distributions are normalised by their total event yield. . . . .	121
6.8 Pruning results for systematics in the $VZ\gamma$ analysis. The colours indicate whether a systematics shape and normalisation uncertainty components were each retained for the fit or dropped, for each sample and region used in the fit. . . . .	124
6.9 Post-fit signal rarity distributions in each of the four regions used in the fit, as labelled. Uncertainty bands represent the combined uncertainties in each bin, with values constrained by the fit. . . . .	128
6.10 Systematic uncertainties ranked by their post-fit impact on $\mu_{EW}$ . Uncertainties labelled $\gamma$ represent MC statistics uncertainties in the given bin. . . . .	129
6.11 Systematic uncertainties ranked by their post-fit impact on $\mu_{EW}$ , for a projected fit scaled to a luminosity of $420 \text{ fb}^{-1}$ . Uncertainties from MC statistics and jet flavour were removed from this fit. . . . .	131

---

## DEFINITIONS OF ACRONYMS

---

<b>ATLAS</b>	A Toroidal LHC Apparatus.....	21
<b>BCID</b>	Bunch Crossing ID .....	47
<b>CERN</b>	The European Laboratory for Particle Physics.....	18
<b>CP</b>	Cluster Processor.....	30
<b>CPM</b>	Cluster-processor Module .....	45
<b>CR</b>	Control Region.....	xv
<b>eFEX</b>	Electromagnetic Feature Extractor .....	34
<b>EM</b>	Electromagnetic .....	xi
<b>EW</b>	Electroweak .....	10
<b>FEX</b>	Feature Extractor.....	34
<b>FPGA</b>	Field-programmable Gate Array .....	39
<b>GEP</b>	Global Event Processor.....	37
<b>gFEX</b>	Global Feature Extractor .....	34
<b>HL-LHC</b>	High-Luminosity LHC .....	33
<b>HLT</b>	High-level Trigger.....	29
<b>JEP</b>	Jet/Energy Processor .....	30
<b>jFEX</b>	Jet Feature Extractor .....	34
<b>L1Calo</b>	Level-1 Calorimeter .....	33
<b>LAr</b>	Liquid Argon.....	25
<b>LATOME</b>	Liquid Argon Trigger Optical Mezzanine.....	47
<b>LHC</b>	Large Hadron Collider.....	18

---

<b>LO</b>	Leading Order	65
<b>MC</b>	Monte Carlo	xv
<b>NLO</b>	Next-to-leading Order	65
<b>NNLO</b>	Next-to-next-to-leading Order	66
<b>PDF</b>	Parton Density Function	14
<b>QCD</b>	Quantum Chromodynamics	x
<b>QGC</b>	Quadrilinear Gauge Coupling <i>Often called ‘Quartic Gauge Couplings’ in literature.</i>	12
<b>RoI</b>	Region of Interest	30
<b>SM</b>	Standard Model	
<b>SR</b>	Signal Region	xv
<b>TGC</b>	Trilinear Gauge Coupling <i>Often called ‘Triple Gauge Couplings’ in literature.</i>	12
<b>TGC</b>	thin gap chamber <i>when used in Chapter 2</i>	27
<b>TOB</b>	Trigger Object	34
<b>UI</b>	User Interface	38
<b>VBS</b>	Vector-boson Scattering	63
<b>FSR</b>	Final-state Radiation	71
<b>PV</b>	Primary Vertex	68
<b>TRT</b>	Transition Radiation Tracker	24
<b>MS</b>	Muon Spectrometer	27
<b>ID</b>	Inner Detector	23
<b>BDT</b>	Boosted Decision Tree	x
<b>PoI</b>	parameter of interest	123
<b>QFT</b>	quantum field theory	2
<b>QED</b>	quantum electrodynamics	6
<b>MDT</b>	monitored drift tube	27
<b>CSC</b>	cathode strip chamber	27
<b>RPC</b>	resistive-plate chambers	27
<b>EMEC</b>	electromagnetic end-cap	25

<b>HEC</b> hadronic end-cap .....	25
<b>FCal</b> forward calorimeter .....	25
<b>TDAQ</b> trigger and data acquisition .....	29
<b>PPM</b> pre-processor module .....	30
<b>CTP</b> central trigger processor .....	30
<b>LEP</b> Large Electron-Positron Collider .....	18
<b>SCT</b> semiconductor tracker .....	24



---

## Introduction

---

# CHAPTER 1

---

## Theory

---

### 1.1 Quantum field theory

The study of elementary particle physics is built on the foundations laid by quantum field theory (QFT). This mathematical framework describes particles as excitations in quantised fields, and the nature of these fields governs the interactions between particles.

QFT is the only way to reconcile the principles of quantum mechanics and special relativity<sup>1</sup> [1]. Attempts at relativistic quantum wave mechanics, such as the Dirac theory [2], failed to explain the mechanics of antiparticles; with the theory relying on the Pauli exclusion principle [3] preventing ‘regular’ particles from falling into negative energy states, and thus working only for fermions and not bosons [1, p.14]. QFT solves this problem and others by introducing a quantum field, in which parti-

---

<sup>1</sup>Aside from theories that introduce infinite types of particle, e.g. string theory.

cles and antiparticles can be created and annihilated; the creation and annihilation of particles represents the interactions that QFT describes. Promotion of the wave function to a field gives a natural description for many-particle systems. This better equips QFT to describe real states in nature as, at the microscopic level, there are no true one-particle systems [4].

Many different QFTs can be formulated, e.g. to describe the interactions of different forces. The Lagrangian density,  $\mathcal{L}$ , is typically used to define the dynamics of a given QFT. Lagrangian densities are a necessary tool to describe many-particle systems, related to the Lagrangian,  $L$ , by

$$L = \int d^3x \mathcal{L}.$$

Motivating the use of the Lagrangian is beyond the scope of this thesis, but for an introduction to Lagrangian mechanics see Reference [5, pp.461-3] and for an explanation of Lagrangian formalism in QFT see Reference [1, pp.298-306]. The terms Lagrangian and Lagrangian density will be used interchangeably for the remainder of this chapter.

There is no guarantee that the ‘theory of everything’ that we need to describe the fundamentals of nature is a QFT. It is true, however, that any relativistic quantum theory applied to particles at sufficiently low energy will look like a QFT [1]. Even if the theory of everything is not a QFT, it is clear from observations that modern particle physics is still in a realm where energies are sufficiently low (relatively speaking) that QFT is accurate as an effective field theory. This has been demonstrated by the success of the current leading theory, discussed in Section ??.

## 1.2 Symmetries and transformations

### 1.2.1 Lie groups

Lie groups, and their corresponding Lie algebras, are used to define the symmetries obeyed by a given theory. Lie groups represent a set of transformations that can be applied to a state, and are used to represent symmetries in theories when transformations between these states should be invariant. Two types of group are prominent in particle physics theory: unitary and special unitary groups. A unitary group of degree  $n$ , denoted  $U(n)$ , is the infinite group of all unitary  $n \times n$  matrices under matrix multiplication. A special unitary group of degree  $n$ ,  $SU(n)$ , is a subgroup of the corresponding unitary group and contains all  $n \times n$  matrices with a determinant of 1. An  $SU(n)$  group has  $n^2 - 1$  members, or ‘generators’.

Of interest to the theories discussed here are the groups  $U(1)$ ,  $SU(2)$ , and  $SU(3)$ . The  $U(1)$  group contains all complex numbers with a magnitude of 1; a  $U(1)$  transformation is equivalent to a change in complex phase. As complex numbers commute,  $U(1)$  forms an Abelian group.

The  $SU(2)$  group contains three  $2 \times 2$  matrices,  $T^a$ , which may be expressed in terms of the Pauli spin matrices as  $T^a = \sigma^a/2$ . The generators of  $SU(2)$  are non-commutative, with the commutator

$$[T^a, T^b] = i\varepsilon^{abc}T^c,$$

where  $\varepsilon^{abc}$  is the totally antisymmetric Levi-Civita tensor; the  $SU(2)$  group is therefore non-Abelian.

More generally, the commutator for generators of an  $SU(n)$  algebra are given by

$$[T^a, T^b] = if^{abc}T^c, \quad (1.1)$$

where  $f^{abc}$  is a totally antisymmetric tensor specifying the structure constants of the Lie algebra. For the  $SU(2)$  definition given above,  $f^{abc} = \varepsilon^{abc}$ .

The third group of interest is  $SU(3)$ ; this group is also non-Abelian and contains 8 generators, which in this instance are  $3 \times 3$  matrices. A typical basis for the generators of  $SU(3)$  would give structure constant values

$$\begin{aligned} f^{123} &= 1, \\ f^{147} = f^{246} = f^{257} = f^{345} = -f^{367} = -f^{156} &= \frac{1}{2}, \\ f^{458} = f^{678} &= \frac{\sqrt{3}}{2}, \end{aligned}$$

with all other elements equal to zero [6].

### 1.2.2 Gauge transformations

A gauge, in theoretical particle physics, is an abstract frame of reference that often manifests as a mathematical simplification made by modifying fields or operators, known as a gauge transformation. These transformations lead to a deeper symmetry required in theories: if a gauge transformation is allowed within a theory then it must not affect the observables of the theory, the theory must be symmetric under these transformations. This gauge symmetry is a core concept of modern QFTs, and such gauge-symmetric QFTs are known as gauge theories.

A gauge transformation can local or global. A global gauge transformation is where the parameter controlling the transformation is constant across space-time. Local transformations are a more general case where the parameter is a function of spatial coordinates and can vary between locations.

The transformations between allowed gauges in a theory form a Lie group. For each generator in the Lie group a gauge field is introduced. Inclusion of these gauge fields in the Lagrangian ensure that the theory is invariant under gauge transformations. If a theory is local gauge invariant, these gauge fields can vary across space-time

and allow for interactions between particles in the theory; this is how forces are introduced in gauge theories. The quanta of a gauge field in a QFT is called a gauge boson.

For an example of constructing a QFT satisfying local gauge invariance see Reference [5, pp.242-3].

## 1.3 Gauge theories

### 1.3.1 Quantum electrodynamics

Quantum electrodynamics (QED) describes electromagnetic interactions between charged particles. As a gauge theory respecting local  $U(1)$  transformations it introduces a single massless gauge boson, the photon. When formulated as a QFT, quantum electrodynamics (QED) must therefore describe fermions, photons, and the interactions between them. The QED Lagrangian can be built from three terms:

$$\mathcal{L}_{\text{QED}} = \mathcal{L}_{\text{Dirac}} + \mathcal{L}_{\text{EM}} + \mathcal{L}_{\text{int}}.$$

The  $\mathcal{L}_{\text{Dirac}}$  term describes the dynamics of a fermion under Dirac theory. This is given by

$$\mathcal{L}_{\text{Dirac}} = \bar{\psi}(i\gamma^\mu\partial_\mu - m)\psi,$$

where  $\psi$  is a Dirac spinor, a four-component fermion field representing up-down and particle-antiparticle states for a fermion of mass  $m$ . The  $\gamma^\mu$  are a set of matrices accounting for fermion spin, these are commonly absorbed into the covariant derivative using the Feynman slash notation,  $\gamma^\mu\partial_\mu \rightarrow \not{\partial}$ .

Maxwell's equations provide the terms  $\mathcal{L}_{\text{EM}}$  and  $\mathcal{L}_{\text{int}}$ , describing the kinematics of

the photon and their interaction with charged fermions:

$$\begin{aligned}\mathcal{L}_{\text{EM}} &= -\frac{1}{4}F^{\mu\nu}F_{\mu\nu} = -\frac{1}{4}(F_{\mu\nu})^2, \\ \mathcal{L}_{\text{int}} &= -J^\mu A_\mu = -q\bar{\psi}\gamma^\mu\psi A_\mu.\end{aligned}$$

Here  $A_\mu$  is the electromagnetic vector potential;  $F_{\mu\nu}$  is the electromagnetic field tensor, given by

$$F_{\mu\nu} = \partial_\mu A_\nu - \partial_\nu A_\mu; \quad (1.2)$$

and  $J^\mu = q\bar{\psi}\gamma^\mu\psi$  is a conserved current, satisfying  $\partial_\mu J^\mu = 0$ , for a fermion of charge  $q$ .

Combining these, and simplifying by defining a gauge covariant derivative

$$D_\mu = \partial_\mu - iQA_\mu, \quad (1.3)$$

gives the full QED Lagrangian:

$$\mathcal{L}_{\text{QED}} = \bar{\psi}(iD^\dagger - m)\psi - \frac{1}{4}(F_{\mu\nu})^2.$$

This result could instead be obtained by starting from the Dirac Lagrangian and enforcing local gauge invariance through the covariant derivative transformation in Equation 1.3. The form of Equation 1.3.1 is recovered with the inclusion of the  $\mathcal{L}_{\text{EM}}$  term, which is the only locally gauge invariant formulation of a kinetic term for the field  $A_\mu$ . Its invariance can be demonstrated from the local gauge invariance of the commutator  $[D_\mu, D_\nu]$ , given

$$\begin{aligned}[D_\mu, D_\nu] &= iq(\partial_\mu A_\nu - \partial_\nu A_\mu) \\ &= iqF_{\mu\nu}.\end{aligned} \quad (1.4)$$

This technique for deriving field tensors from potentials will be relevant in discussion of other theories. For the complete derivation of  $\mathcal{L}_{\text{QED}}$  through the requirement of

gauge invariance, see [7, pp.482-6].

### 1.3.2 Yang-Mills theory

The QED theory corresponds to a  $U(1)$  gauge symmetry, and as such is Abelian. Constructing a non-Abelian gauge theory respecting  $SU(n)$  symmetries is more complex, but generically solved by the Yang-Mills theory [8].

For generators of the Lie algebra  $T^a$  and structure constant  $f^{abc}$ , a gauge covariant derivative can be defined by

$$D_\mu = \partial_\mu - igT^a A_\mu^a,$$

where a vector field  $A_\mu^a$  is required for each generator of the  $SU(n)$  group, and  $g$  is a coupling constant. Here the exponents  $a, b, c$  index the generators of the Lie algebra, whilst  $\mu, \nu$  index space-time dimensions, as per convention.

This gauge covariant derivative is a generalisation of the Abelian form, given in Equation 1.3, and acts on an  $n$ -plet,  $\psi$ , of spinors,  $\psi_i$ , rather than on a single spinor as in the QED case. The generators of  $SU(n)$  serve to transform  $\psi_i$  into one-another through abstract rotations.

In analogy to the Abelian case in Equation 1.4, the commutator is used to define a set of field strength tensors: the commutator

$$[D_\mu, D_\nu] = -igF_{\mu\nu}^a T^a$$

holds for a field strength satisfying

$$F_{\mu\nu}^a T^a = \partial_\mu A_\nu^a T^a - \partial_\nu A_\mu^a T^a - ig[A_\mu^a T^a, A_\nu^b T^b].$$

This shows explicitly that for an Abelian symmetry group, with  $[T^a, T^b] = 0$ , the form of Equation 1.2 is recovered. For non-Abelian gauge theories, however, the

additional term is introduced, with dependence on the potentials from other gauge fields. This is known as a ‘nonlinear’ term, and represents self-interaction of gauge fields.

Substituting in the general form for the commutator of  $SU(n)$  generators given in Equation , the general form of a field strength for such a non-Abelian gauge theory is given by

$$F_{\mu\nu}^a = \partial_\mu A_\nu^a - \partial_\nu A_\mu^a + g f^{abc} A_\mu^b A_\nu^c. \quad (1.5)$$

This leads to the Yang-Mills Lagrangian, the most general renormalisable Lagrangian for a theory respecting  $SU(n)$  symmetry expressed in terms of these field strengths,

$$\mathcal{L}_{\text{YM}} = \bar{\psi}(iD^\mu - m)\psi - \frac{1}{4}(F_{\mu\nu}^a)^2. \quad (1.6)$$

A more detailed derivation for the Yang-Mills theory can be found in Reference [7, pp.486-91].

### 1.3.3 Quantum chromodynamics

The strong force, or QCD, is modelled by a non-Abelian gauge theory. The fundamental particles that QCD acts on are quarks. A charge is attached to quarks that works as the electric charge in QED, but to describe the observed dynamics of the strong force this charge comes in three flavours. This charge is known as colour charge, and the three flavours are red, green, and blue.

Transformation of a quark from one quark to another acts as a gauge symmetry in the theory; if all red quarks became green, green became blue, and blue became red the predictions of the theory would remain unchanged. This rotation of colour charge is described perfectly by the  $SU(3)$  symmetry.

QCD can therefore be constructed as a Yang-Mills theory under  $SU(3)$ , with the Lagrangian following that of Equation 1.6. Given that the  $SU(3)$  group has 8

generators, the theory of QCD relies on 8 gauge bosons to mediate interactions. These bosons are called gluons, and the 8 varieties are represented as different colour combinations of the gluons.

It can be shown that the coupling constant (appearing 1.5) for QCD is actually not a constant, and is dependent on the energy scale of interactions [9]. For high energies (i.e. large distance scales) the coupling strength tends to zero, leading to ‘asymptotic freedom’. Quarks can only exist as free particles in the high energy limit, whereas at and below energies of  $\sim 1$  GeV the coupling strengths are sufficiently high that quarks are exclusively confined in colourless composite particles, hadrons.

### 1.3.4 The electroweak theory

The Electroweak (EW) theory describes the weak interaction, and also supersedes QED as it unifies the weak and EM forces. It combines the local  $U(1)$  invariance of QED with the symmetry of the weak interaction under local  $SU(2)$  transformations, and thus is described by  $SU(2) \times U(1)$  symmetry. The gauge covariant derivative for the theory is given by

$$D_\mu = \partial_\mu - igT^a W_\mu^a - \frac{1}{2}ig'B_\mu,$$

where  $a$  indexes the 3 generators of the  $SU(2)$  algebra,  $T^a$ , and their corresponding gauge fields,  $W_\mu^a$ . The field  $B_\mu$  is required for invariance under  $U(1)$  symmetry.

The corresponding field strengths are then

$$\begin{aligned} W_{\mu\nu}^a &= \partial_\mu W_\nu - \partial_\nu W_\mu + g\varepsilon^{abc}W_\mu^b W_\nu^c \\ B_{\mu\nu} &= \partial_\mu B_\nu - \partial_\nu B_\mu \end{aligned}$$

To treat this as a conventional Yang-Mills theory would result in four massless gauge bosons, three corresponding to the three  $W_\mu^a$  fields mediating the weak interaction, and one from the  $B_\mu$  field mediating EM interactions. The weak interaction being

mediated by massless bosons would result in asymptotic freedom of weakly interacting particles, as seen in QCD; this is not what is observed experimentally, so this Yang-Mills theory cannot form a complete description of the interaction.

The missing ingredient is spontaneous EW symmetry breaking through the Higgs mechanism. When the Higgs field takes a non-zero vacuum expectation value, a rotated set of the potentials,  $W_\mu^a$  and  $B_\mu$ , appears in the Lagrangian instead, resulting in gauge fields:

$$\begin{aligned} W_\mu^\pm &= \frac{1}{\sqrt{2}}(W_\mu^1 \mp iW_\mu^2), \\ Z_\mu &= \frac{1}{\sqrt{g^2 + g'^2}}(gW_\mu^3 - g'B_\mu), \\ A_\mu &= \frac{1}{\sqrt{g^2 + g'^2}}(g'W_\mu^3 + gB_\mu). \end{aligned}$$

The  $W_\mu^\pm$  and  $Z_\mu$  fields have mass terms in the Lagrangian, with masses parametrised by

$$m_W = \frac{gv}{2}, \quad m_Z = \frac{\sqrt{g^2 + g'^2}v}{2},$$

where  $v$  is the vacuum expectation value.

This converts the previous form of the theory with four massless bosons to a description with three massive bosons, the two charged W bosons and the neutral Z boson, and one massless boson, which is identified as the photon.

Due to the non-Abelian  $SU(2)$  symmetry group used to build this theory, we see self-interaction terms arising in the Lagrangian, as explained in Section 1.3.2. The resulting interactions are discussed in Section ??.

Another result of the Higgs mechanism is the introduction of a massive scalar boson, the Higgs boson. A detailed description of the Higgs mechanism is beyond the scope of this thesis, but Reference [7] explains the form of equations given here as well as giving much more detail on the topic.

## 1.4 The Standard Model of particle physics

The Standard Model (SM) of particle physics is a gauge QFT which combines all of the theories discussed in Section 1.3 into a single theoretical description. As a result, the SM respects a symmetry of  $SU(3) \times SU(2) \times U(1)$ , a combination of the QCD and EW theories.

The SM models the interactions of 12 fermions, mediated by 12 gauge bosons and an additional scalar boson, the Higgs. The 12 fundamental fermions are split into six leptons and six quarks, each can be paired up across three generations. The leptons come in charged lepton-neutrino pairs in electron, muon, and tau families. There are three generations of up-type and down-type quark pairs: up-down, charm-strange, and top-bottom. These fermions all have unique masses, although the values of the masses are not derivable from the theory.

The 12 gauge bosons are those introduced by the imposed symmetries: eight gluons from  $SU(3)$ , 3 weak bosons ( $W^+$ ,  $W^-$ ,  $Z$ ) from  $SU(2)$  and the photo ( $\gamma$ ) from  $U(1)$ . The gluons and photon are all required to be massless by the theory and the weak bosons have related masses, as discussed in Section 1.3.4. The additional boson, the Higgs boson, is also massive, although the theory does not explicitly constrain its mass. All 17 varieties of fundamental particle (grouping the eight gluons and 2 W bosons) are shown in Figure 1.1.

Of particular interest to analyses presented in this thesis are EW direct multiboson interactions. These are interactions introduced in the Lagrangian involving multiple EW bosons. As explained in Section 1.3, these arise from the non-Abelian construction of the electroweak sector. These interactions involve either three or four bosons at a single vertex, termed Trilinear Gauge Coupling s (TGCs) and Quadrilinear Gauge Coupling s (QGCs) respectively. In the SM, there are two TGC vertices,  $W^+W^-Z$  and  $W^+W^-\gamma$ , and four QGC vertices,  $W^+W^-W^+W^-$ ,  $W^+W^-ZZ$ ,  $W^+W^-\gamma\gamma$ , and  $W^+W^-Z\gamma$  [5, p.541][10]. Figure 1.2 shows examples of these as Feynman diagrams.

## Standard Model of Elementary Particles

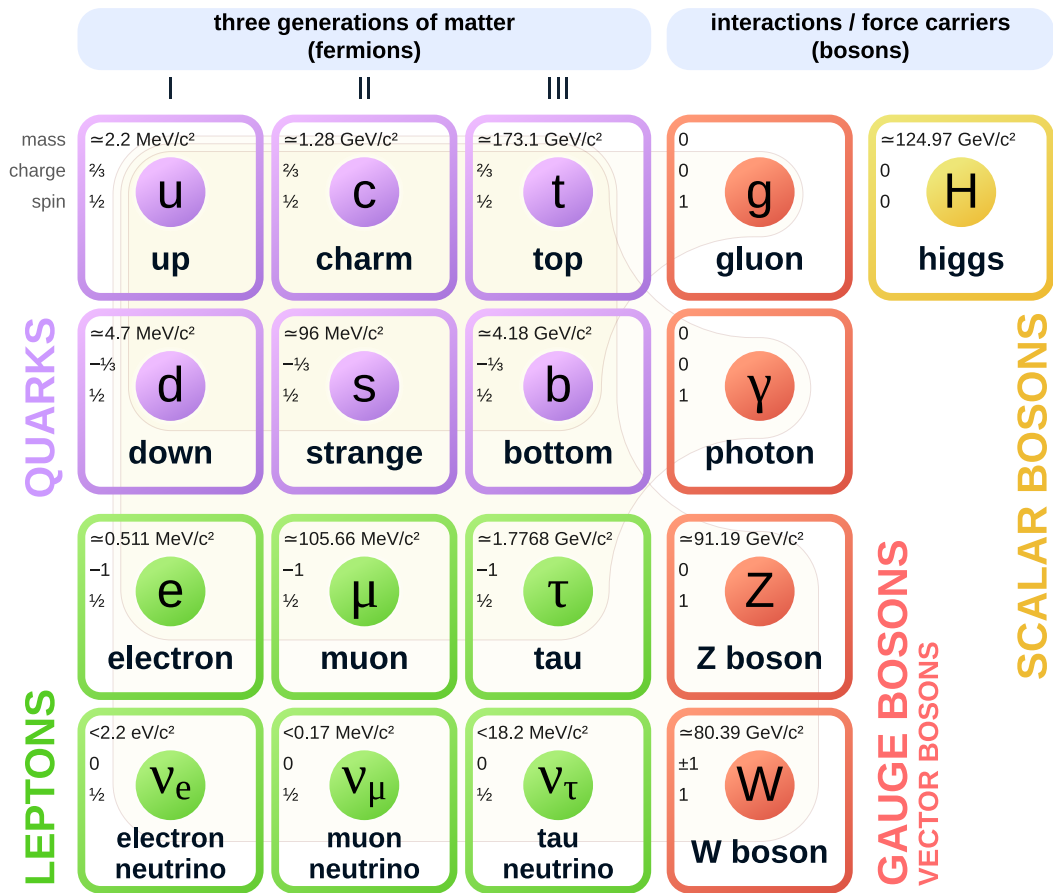


Figure 1.1: All fundamental particles described by the Standard Model shown with their masses, or limits on masses, measured from experiments. Particles are grouped into quarks, leptons, and bosons, with the grey outlines grouping each gauge boson with the fermions it acts on.

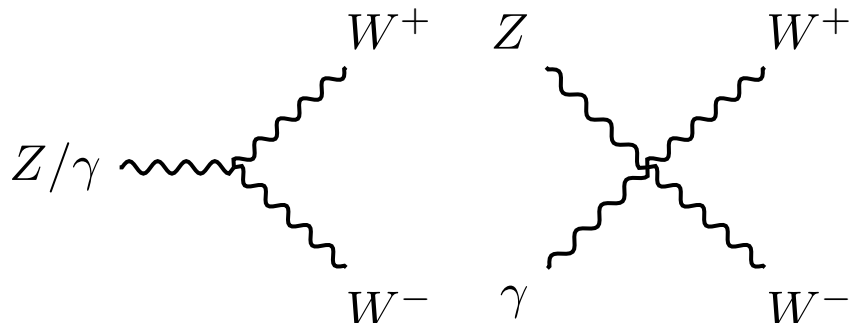


Figure 1.2: Example SM multiboson interactions: a three-boson vertex (left) and a four-boson vertex (right) are shown.

Whilst the SM has been very successful so far when its predictions are compared to experimental observations, it does not fully describe elementary particle physics. One missing piece is the fourth fundamental force, gravity. The current best theory of gravity, general relativity, is not quantisable and thus incompatible with the QFT structure of the SM. At sufficiently high energies, the SM description of physics will break down without accounting for the effects of gravity.

Other signs point to the SM being merely an effective theory, a low-energy approximation of some more complete theory. The SM has 25 parameters [5], such as the fermion masses, with values that have to be constrained by experiment rather than being dictated by the theory itself. This is not characteristic of a truly fundamental theory as it leaves many questions unanswered.

Contemporary experimental particle physics is dedicated to both testing predictions of the SM and searching for signatures of physics beyond it. Either by finding evidence of a more fundamental theory, or by identifying a breakdown in the SM description, the goal is to break the SM.

## 1.5 Proton-proton collisions

In collider physics, observable interactions between SM particles are induced by colliding particles in a controlled environment. In the case of the LHC (introduced in Section 2.1), these collisions are between two high-energy protons.

As protons are composite particles, interactions due to proton-proton collisions are initiated by constituent partons in the protons. Modelling these interactions requires knowledge of the fraction of the total proton energy carried by its partons. The distribution of these energies is given by Parton Density Functions (PDFs), which are determined experimentally from deep inelastic scattering measurements [11].

Interesting interactions are typically produced when two partons with high energy fractions collide, this is known as a hard scatter. In many collisions this will not

occur, and only soft low-energy interactions take place. Even when there is a hard scatter it will be surrounded by ‘spectator interactions’, soft collisions between other partons in the colliding protons. This complicates measurements made from proton-proton collisions.

A further complication is the introduction of pileup. In order to increase the rate of hard-scatter events, colliders are often configured to create multiple proton-proton collisions at once. This results in many, typically soft, interactions being produced around any hard scatter that is detected, termed ‘pileup interactions’.

These effects all complicate the procedure of measuring and understanding events from proton-proton collisions. The methods used to make practical measurements of SM processes under such conditions are discussed in the following section.

## 1.6 Monte Carlo predictions

The SM is tested by comparing its predicted cross-sections for a set of measurable physics processes with the rate observed in data. To isolate processes of interest, this is often done in complicated phase spaces and differentially across distributions, so calculating the predicted cross-sections is quite complex. Real measurements are also subject to the limitations and effects of the detector; for accurate comparisons to be made between data and predictions, these need to be accounted for.

The solution to this problem is to generate Monte Carlo (MC) events representing the SM prediction. For a given final state (i.e. the set of particles produced in the interaction) a sample of events is generated for each contributing process, containing particles with random kinematic properties generated in such a way that the overall distribution matches the expectation from the model. If all processes are accounted for, taking the sum of events from all of these samples in a certain final state and phase space, the yield of MC events should match the yield of data events.

Production of MC samples is a very complicated process and there are several imple-

mentations commonly used in the field, known as MC generators. Generators discussed in this thesis include MADGRAPH [12], SHERPA [13], PYTHIA [14], POWHEG [15], and HERWIG [16].

These generators are used to simulate the hard scatter, the interaction responsible for creating the desired final state. In order to match the simulation to the conditions under which the process is initiated, the generator must use a PDF set determined from data under the same conditions.

Simulating a single physics process does not give a complete picture of a real detector event, however. This is the core of the hard scatter, the primary high energy collision in the event, but several additional steps must be taken: parton showering, applied to any strongly interacting particles; hadronisation, converting these showers into composite hadrons; adding the ‘underlying event’, all of the activity expected in the collision from sources other than the hard scatter; and detector simulation, accounting for effects of particles being measured by the detector.

For each parton from the hard-scatter process, a shower of QCD activity is produced from repeated strong interactions. This continually creates more, lower energy, partons until the energies reach a regime where confinement effects become relevant. Confining the shower products into colourless hadrons is handled by a hadronisation model, such as string fragmentation [17]. Both parton showering and hadronisation are incorporated into MC event generators. Some generators, such as SHERPA, will simulate the hard-scatter process, parton showering, and hadronisation all in one. In other cases the hard-scatter process is created with one generator, e.g. MADGRAPH, and then another generator is used to add parton showering and hadronisation to it, e.g. PYTHIA or HERWIG.

Underlying event is a term used to describe everything happening around the hard scatter in collisions; this includes spectator and pileup interactions, as introduced in Section 1.5. Modelling the underlying event is very dependent on the specific conditions under which the collisions are happening. This is mitigated by tuning certain

parameters of the model to match data; different ‘tunes’ are available from data collected under different conditions. For MC samples, underlying event modelling is typically handled by the same generators as the parton showering and hadronisation.

Having simulated the hard scatter, parton showering, hadronisation, and the underlying event, the particles and their kinematics should be established. The remaining step is determining how this event would be detected in an experiment, if it were from a real collision. For the ATLAS detector (introduced in Section 2.2) this is done using GEANT4 [18, 19].

A distinction is made between information from MC samples before and after detector simulation. Simulated events before detector simulation is applied are known as ‘truth’ events, they contain only the physics processes and are not subject to any inefficiencies or misidentification of the simulated detector. Events completing the full simulation chain are known as reconstructed MC events. These are typically linked so that the truth properties (or ‘truth record’) of reconstructed MC events are accessible. Analysis is typically done using reconstructed MC events, but in certain cases making distinctions based on truth information is necessary.

Events simulated in the manner discussed here are used extensively for the two analyses presented in this thesis (as well as for studies presented in Chapter 3). The signal process and all backgrounds in the final state have dedicated MC simulation samples generated in order to model the kinematics of events. Generation of these specific samples is discussed in Section 4.2.

# CHAPTER 2

---

## The ATLAS detector at the Large Hadron Collider

---

### 2.1 The Large Hadron Collider

The Large Hadron Collider (LHC) is a circular<sup>1</sup> particle collider, measuring 27km in circumference, located at The European Laboratory for Particle Physics (CERN) in Geneva, Switzerland [20, 21, 22]. As a successor to the Large Electron-Positron Collider (LEP) [23], the LHC was designed to study higher energy systems than had previously been accessible in controlled, high-rate, collisions. One of the key goals of the LHC was discovering the Higgs boson, a goal which was achieved in 2012 [24, 25, 26]. However, the LHC research programme is much more broad than the search and study of the Higgs boson; many aspects of the SM are investigated to find signs of inconsistency between theory and experiment.

Controlled interactions are created by colliding accelerated beams of protons at

---

<sup>1</sup>Roughly circular, since the ring consists of alternating straight and curved sections.

## 19 CHAPTER 2. THE ATLAS DETECTOR AT THE LARGE HADRON COLLIDER

interaction points. Two beams of protons, travelling in opposite directions around the LHC ring, are accelerated to an energy of 6.5 TeV<sup>2</sup>. Creating collisions between these two beams at certain interaction points on the ring results in proton-proton interactions at a centre-of-mass energy of 13 TeV. Experiments are built around the interaction points to observe the results of these high-energy interactions.

Protons are obtained by ionising hydrogen gas with an electric field. A chain of many accelerators is then used to take the initial at-rest protons up to an energy of 450 GeV, when they are injected into the LHC. This injector chain is shown, amongst other CERN accelerators, in Figure 2.1. Once in the LHC, protons are further accelerated to the desired beam energy of 6.5 TeV. This acceleration, both in the injectors and the LHC machine itself, is performed using superconducting radio-frequency cavities; these are electromagnetic fields that alternate in such a way as to ‘pull’ protons towards them and then ‘push’ them away.

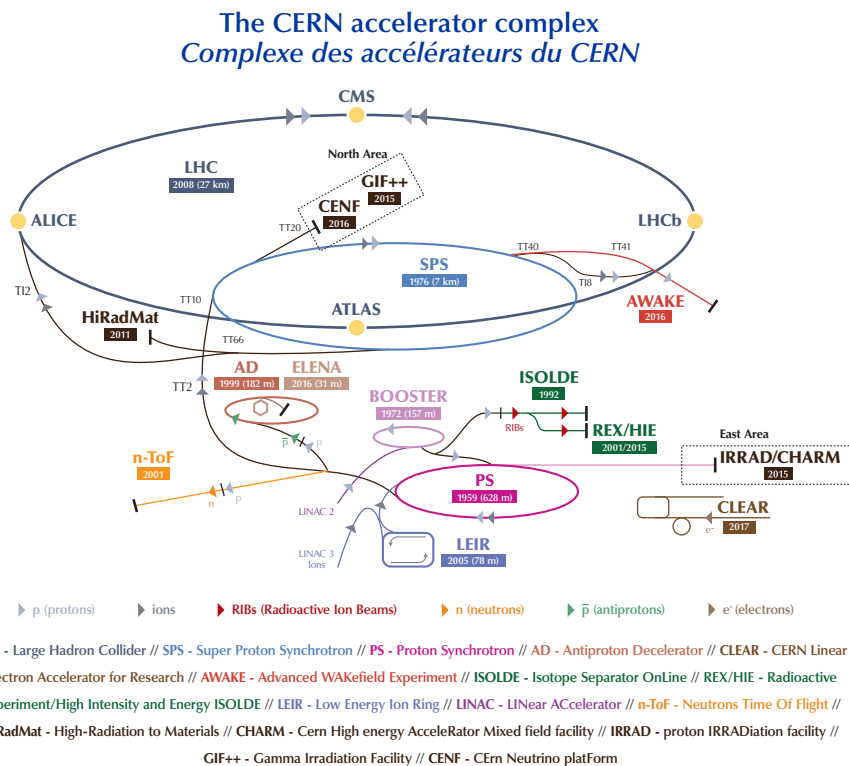


Figure 2.1: Schematic of the CERN accelerator complex. The chain of accelerators used to inject protons into the LHC is LINAC2→BOOSTER→PS→SPS [27].

<sup>2</sup>Numbers given here correspond to the Run-2 parameters of the machine.

Superconducting magnets are used to bend and focus the beam. A total of 1232 dipole magnets, with a field strength of 8.3 T, are used to bend the path of the beam, as required by the circular design of the collider. Additionally, 392 quadrupole magnets are placed around the LHC to focus the beam, squeezing the protons together to make the profile of the beam more compact [20].

Protons are injected into the LHC in bunches, with approximately  $10^{11}$  protons in a single bunch. Consecutive bunches are injected with a minimum separation of 25 ns; this is referred to as a bunch train when many bunches are used at this minimum separation.

To create collisions between the two proton beams, insertion magnets are used to cross the paths of the beams [28]. Each colliding pair of bunches, one from each beam, is called a ‘bunch crossing’. The magnets can be adjusted in order to change the crossing angle, affecting the number of proton-proton collisions induced for each bunch crossing.

The rate at which collisions occur in the LHC is known as instantaneous luminosity,  $\mathcal{L}$ , and is given by

$$\mathcal{L} = \frac{N_p^2 n_b f_{\text{rev}} \gamma}{4\pi \epsilon_n \beta^*} F,$$

where  $N_p$  is the number of particles per bunch,  $n_b$  is the number of bunches per beam,  $f_{\text{rev}}$  is the revolution frequency of the beam,  $\gamma$  is the relativistic Lorentz factor,  $\epsilon_n$  and  $\beta^*$  parametrise the optics of the beam, and  $F$  is a factor describing the crossing angle of the two beams. The design luminosity for the LHC is  $\mathcal{L} = 1 \times 10^{34} \text{ cm}^{-2}\text{s}^{-1}$ , and throughout Run 2 the machine operated between around 0.5 to 2 times this amount [29].

Integrated luminosity,  $L$ , is used to measure the amount of data in an entire dataset. This quantity is the integral of instantaneous luminosity over time,

$$L = \int dt \mathcal{L}.$$

The expected number of collisions for a particular process is given by the product of the integrated luminosity with the cross-section of the process,  $\sigma$ . Obtaining a large dataset is therefore vital to measure processes with very low cross sections. The LHC produced a dataset of  $160 \text{ fb}^{-1}$  over the entirety of Run 2 [29].

The LHC has periods of operations known as runs. Each run consists of multiple years of data-taking, with some short shutdown periods for maintenance and minor upgrades. Between each run is a ‘long shutdown’ period, in which more significant upgrades can take place. Analyses in this thesis use data taken during Run 2, between 2015 and 2018. Run 3 began in 2022, with an increase in centre of mass energy to 13.6 TeV, and is currently ongoing at the time of writing.

## 2.2 The ATLAS detector

ATLAS (A Toroidal LHC Apparatus) is one of the four detectors built around interaction points at the LHC. The ATLAS detector is the largest of the four, and designed as a general-purpose detector to measure as many different processes as possible. In order to do this, it surrounds the interaction point almost entirely; full angular acceptance would allow any event to be fully reconstructed from its detected decay products. The detector itself is built of several sub-detectors, each dedicated to measuring specific properties of particles. Each of these sub-detectors is discussed in detail below. Figure 2.2 gives an overview of the ATLAS detector and its components.

### 2.2.1 Coordinate system

A specific coordinate system is used to describe the ATLAS detector and interactions within it. The  $z$ -axis runs along the beamline, the  $x$ -axis points, in the positive direction, towards the centre of the LHC ring, and the  $y$ -axis points vertically upwards. The azimuthal angle,  $\phi$ , is measured around the beamline in the  $x$ - $y$

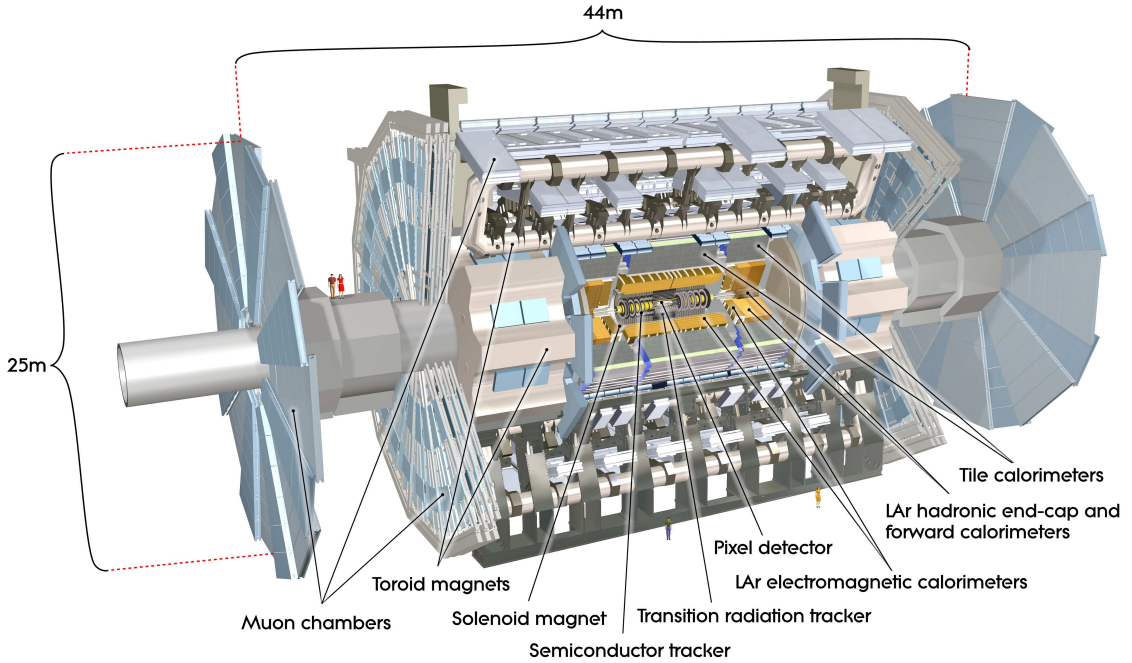


Figure 2.2: Cut-away view of the ATLAS detector. Dimensions and components of the detector are labelled. [30]

plane and the polar angle,  $\theta$ , is measured from the beam axis. A pseudorapidity coordinate,  $\eta$ , is defined as

$$\eta = -\ln \tan(\theta/2).$$

Transverse momentum,  $p_T$ , and transverse energy,  $E_T$ , are used to define the momentum or energy in the  $x$ - $y$  plane, transverse to the beamline.

The set of coordinates  $p_T$ ,  $\eta$ , and  $\phi$  are typically preferred to describe the kinematics of objects in the detector as they are invariant under Lorentz boosts along the beamline<sup>3</sup>. Without this Lorentz invariance, differences in kinematics between events could be introduced depending on the relative momenta of the colliding partons.

Angular differences between objects are typically expressed in terms of the quantity  $\Delta R = \sqrt{\Delta\eta^2 + \Delta\phi^2}$ .

<sup>3</sup>Pseudorapidity itself is not invariant, but transforms additively under Lorentz boosts; differences in pseudorapidity are therefore Lorentz invariant.

### 2.2.2 Inner detector

The innermost detector system, known as the Inner Detector (ID) or tracker, contains three sub-detectors designed to track the location of charged particles, to measure their momentum based on the curvature of their tracks. This is enabled by a solenoid magnet which surrounds the ID, generating a 2 T magnetic field in order to curve the tracks of charged particles travelling through.

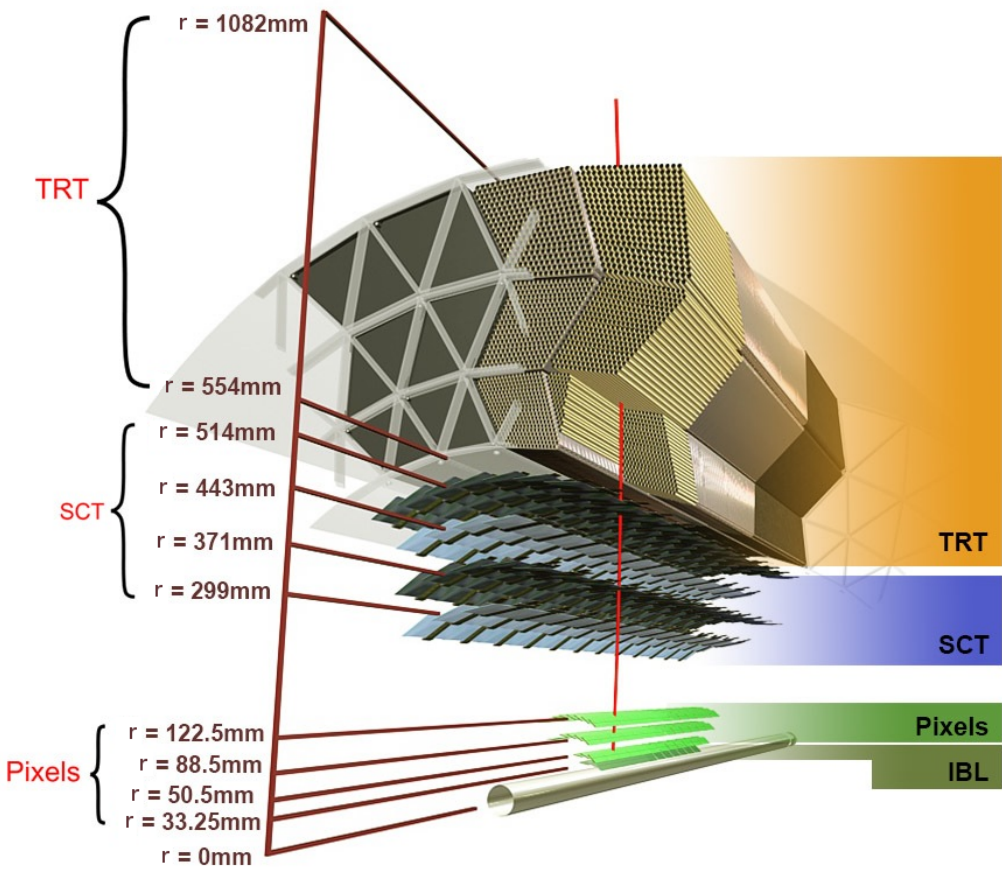


Figure 2.3: Diagram showing the components of the inner detector. The IBL label represents the insertable B-layer, the innermost part of the pixel detector which was added between Run 1 and Run 2. The  $r$  values label radial distances from the centre of the beam pipe. [31]

As particles travel through the components of the ID, ‘hits’ are registered for each location where the particle is detected. Hits across the tracker are fitted to reconstruct the track of the particle. The momentum of this particle is calculated from the radial arc of this track, and the sign of its charge is deduced from the direction of the curve. Extrapolating the track towards its origin allows it to be associated

with a specific collision vertex location on the beamline.

Figure 2.3 shows a cross-section of the ID and its sub-detectors. From the beamline outwards, these are: the pixel detector, the semiconductor tracker (SCT), and the Transition Radiation Tracker (TRT). Each of these are detailed below. The pixel and SCT both cover an acceptance of  $|\eta| < 2.5$  while the TRT has an acceptance of  $|\eta| < 2$ .

The closest component to the beamline is the pixel detector. The pixel detector is designed to measure particles as close to the beamline as possible, with very high granularity and precision. The detector is made up of 1968 silicon sensor modules, with a combined total of  $8.6 \times 10^7$  pixels across all sensors [32]. The nominal pixel size is  $50 \times 400 \mu\text{m}$  (in  $r\phi \times z$ ) and 250  $\mu\text{m}$  thick, with some variation in different regions [30]. As a charged particle passes through a pixel on the sensors it ionises the atoms in the silicon, creating electron-hole pairs; these charges are collected to generate a signal indicating a hit in that pixel.

The next component out, along the path of a particle, is the SCT. The SCT uses silicon strip sensors, which operate on the same principles as the pixels. These strips have typical dimensions of  $80\mu\text{m} \times 6.4\text{cm}$  with a thickness of 285  $\mu\text{m}$  [30]. The SCT consists of four layers, where each layer has two sets of strips back-to-back with a relative angle of 40 mrad between the strips. The rotation between strips within a layer improves resolution along the long axis of the strip. In the barrel strips are placed with their long axis parallel to the beamline (in the  $z$ -direction) and in the end-caps strips are placed in the  $r$ -direction.

The last ID component encountered by incident particles is the TRT. The TRT is composed of  $3.7 \times 10^5$  straw detectors, with a diameter of 4 mm and a length of 144 cm (barrel region) or 37 cm (end-cap region). In the barrel region straws are placed parallel to the beamline. In the end-cap region straws are arranged radially in wheels. The straw detectors contain a gold-plated tungsten wire surrounded by a xenon-carbon dioxide-oxygen gas mixture. The space between straws is filled with

a polymer fibre. Charged particles crossing the boundaries between materials emit transition radiation, dependent on their  $\gamma = E/m$ , which is ionises atoms in the gas mixture and gives a readout on the wire. This gives hits for tracking particles but also provides information on the  $E/m$  ratio of the incident particle; this is used for identification of electrons.

### 2.2.3 Calorimeters

The ATLAS detector has two distinct calorimeter systems: the Liquid Argon (LAr) calorimeter and the tile hadronic calorimeter. These are both sampling calorimeters, employing alternating absorbing and active layers to induce EM or hadronic showers and measure the energies of shower products, respectively. Figure 2.4 shows the location of the calorimeter components in the context of the detector.

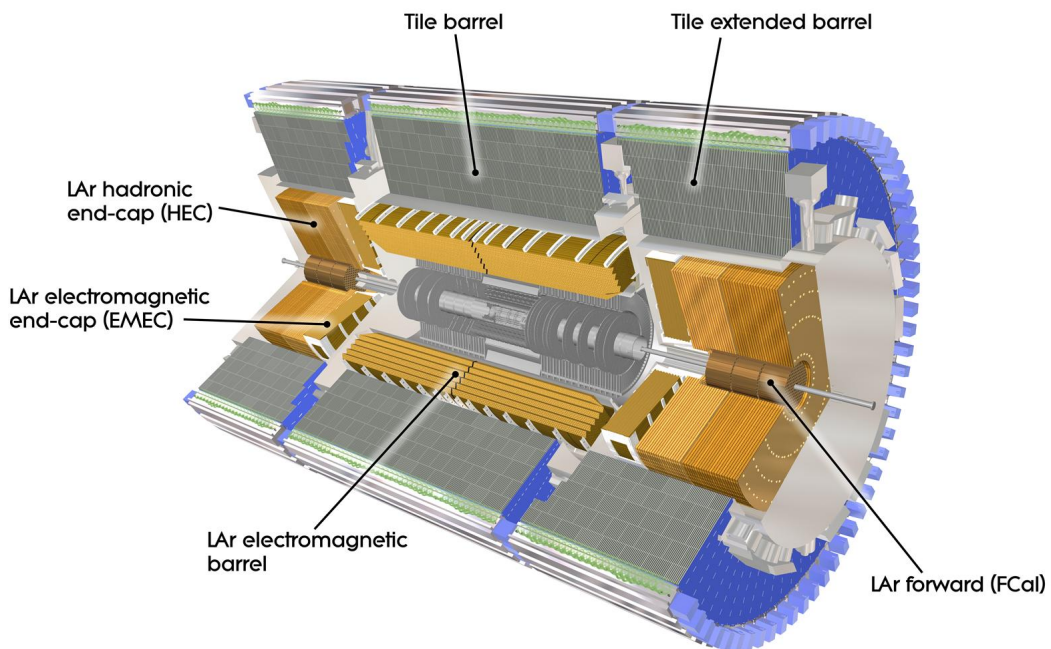


Figure 2.4: Cut-away view of the ATLAS calorimeters, with each component labelled. [38]

The LAr calorimeter has four components, the barrel, the EM end-cap (EMEC), the hadronic end-cap (HEC), and the forward calorimeter (FCal). All of these

components use liquid argon in the active layers, where low-energy shower particles will ionise argon atoms and produce a charge which is collected in order to measure the deposited energy. The barrel and EMEC use lead for the absorbing layers, the HEC uses copper absorbers, and the FCal has a combination of copper and tungsten.

The LAr barrel and EMEC each have three layers of calorimeter cells of differing sizes. These sizes vary by region, but Figure 2.5 shows the layout in the centre of the barrel. There is also an additional ‘presampler’ layer in front of these three layers. The full specification for calorimeter cell granularity is given in Reference [30, p.9].

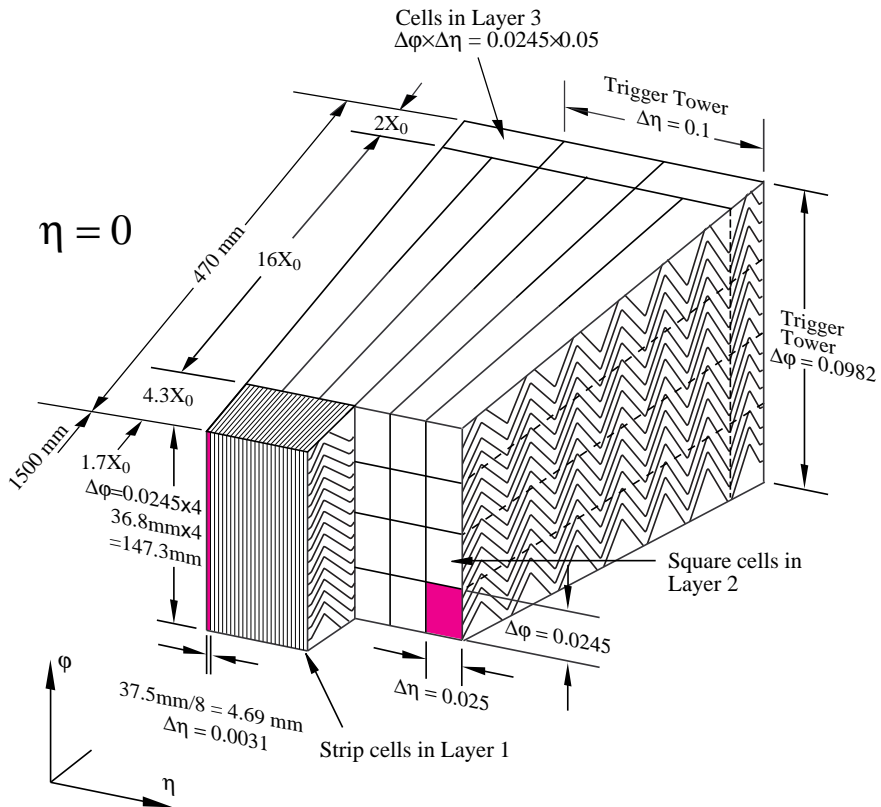


Figure 2.5: Diagram showing layout of calorimeter cells in the barrel of the LAr calorimeter. The  $X_0$  units measure EM radiation lengths. [30]

The first of these calorimeter layers in the barrel for  $|\eta| < 1.4$  consists of strips of cells with very high  $\eta$  granularity. This provides more precise determination of the shape of EM showers in the calorimeter.

The tile hadronic calorimeter uses scintillating plastic tiles for the active layers and

steel absorbing layers. The tile barrel and extended barrel combined give coverage of  $|\eta| < 1.7$ . The barrel and extended barrel are each divided into three layers longitudinally, and have a total thickness of 7.4 hadronic interaction lengths. Between the tile, HEC, and FCal, hadronic calorimetry acceptance is  $|\eta| < 4.9$ .

#### 2.2.4 Muon spectrometer

The outermost component of the ATLAS detector is the Muon Spectrometer (MS). Muons will likely pass through the calorimeters without significant energy loss and, due to their larger mass, relying on the ID alone is imprecise for measuring their momentum and identifying them. The muon spectrometer solves this problem, adding additional tracking for muons in an acceptance of  $|\eta| < 2.7$ .

A large toroidal magnet system is used to curve the tracks of muons passing through the MS, allowing tracking systems to measure their momentum. Tracking information is primarily provided by the monitored drift tube (MDT) and cathode strip chamber (CSC) systems. The resistive-plate chambers (RPC) and thin gap chamber (TGC) detectors add to this, but also provide triggering capabilities. These systems are shown in the context of the detector in Figure 2.6.

The MDTs provide tracking across the full acceptance of the MS, with multiple layers of MDTs in both the barrel and the end-caps. These function similarly to the straw detectors of the TRT, with a tungsten-rhenium wire surrounded by an argon-methane-nitrogen gas mixture.

In the most radiation-prone region, the inner section of the most central end-cap layers, CSCs are used in place of MDT. The CSCs cover pseudorapidities  $2 < |\eta| < 2.7$ . These are multiwire proportional counters with cathodes segmented into strips, and benefit from higher granularity than the MDTs.

The RPCs are placed in the barrel region and consists of two resistive plates separated by a 2 mm gas-filled gap. In the end-cap region, TGCs are used; these are

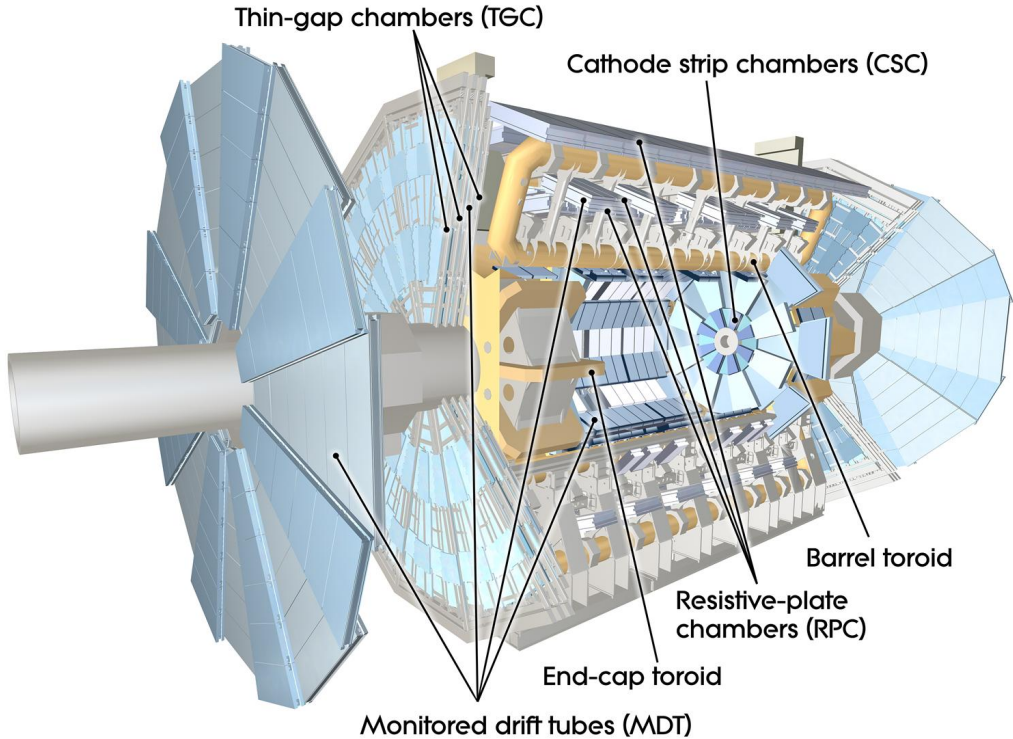


Figure 2.6: Cut-away view of the ATLAS detector with muon spectrometer components labelled. [34]

similar to CSCs but designed with a faster readout suitable for triggering. Both the RPC and TGC are used to give real-time readout of track information for the trigger. They also give a measurement of the ‘second coordinate’, the coordinate orthogonal to what the MDT or CSC are designed to measure in the same region.

### 2.2.5 Trigger and data acquisition

Running at maximum capacity, the ATLAS detector measures an event every 25 ns, i.e. a rate of 40 MHz, and in the majority of events no ‘interesting’ physics happens. There is no realistic way to read out the data from every single event at this rate, but even if this was possible it would create an inflated storage requirement for events that will probably never be used for physics studies.

The trigger is the solution to this problem; events are quickly processed to determine if they have any signatures that might indicate the presence of interesting physics

processes. This is done in two stages: a low-level hardware trigger (the Level-1 trigger) to make very fast but loose selection on events, reducing the input rate to around 100 kHz, and then a high-level trigger (HLT) which uses more information and more complex reconstruction to reduce the rate further down to 1 kHz.

To adjust how events are accepted and to manage the output rate, a trigger ‘menu’ is used; this gives the set of requirements for events to pass the trigger in a given run, for both Level 1 and the HLT.

The trigger works in tandem with the data acquisition system, responsible for reading out events passing trigger selections. This is done with front-end hardware read-out devices that collect the detector information and process it after receiving accept signals from the trigger systems. The entire trigger and data acquisition (TDAQ) system is summarised in Figure 2.7.

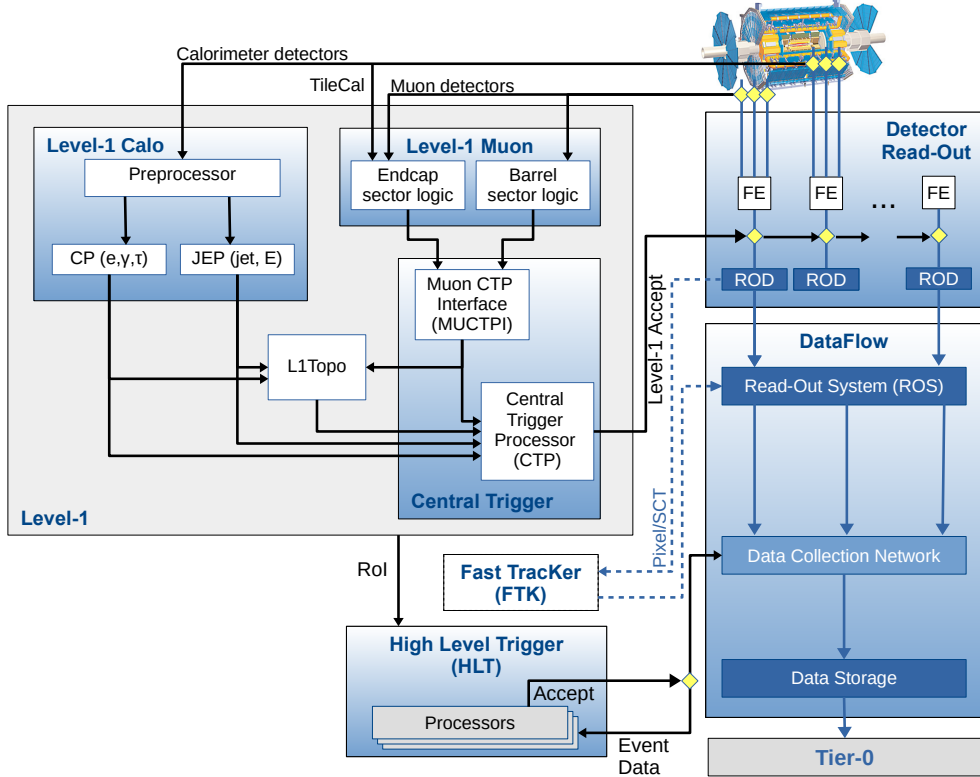


Figure 2.7: Diagram showing components and data-flow of the ATLAS Run-2 TDAQ system. [35]

### 2.2.5.1 Level-1 trigger

The Level-1 trigger system is built of three main components: L1Calo, L1Muon, and L1Topo. Each of these are built from bespoke hardware modules designed to perform the necessary algorithms as quickly as possible to keep up with the rate of input data.

L1Calo takes input from the calorimeters to give triggers for EM objects and jets. From both the LAr and tile calorimeters, the energies in each trigger tower (a  $0.1 \times 0.1$  area in  $\eta \times \phi$ ) are sent to a pre-processor module (PPM). The PPM sends these energies to two modules: the Cluster Processor (CP) and Jet/Energy Processor (JEP). The CP analyses a  $4 \times 4$  area of trigger towers to calculate energies and isolations for  $e/\gamma$  or  $\tau$  candidates. The JEP employs a similar process over larger areas and with lower granularity, in order to calculate energies of jet candidates and estimate missing transverse energy. For each event, L1Calo sends a set of ‘threshold bits’ to the central trigger processor (CTP) indicating multiplicities and energies of different objects with respect to trigger menu thresholds [36].

L1Muon uses tracking information from the RPC and TGC to make a rough estimate of transverse momentum of muons. Any set of two or more hits that are consistent with a track originating at the interaction point are considered as candidate muons. Comparing the calculated  $p_T$  of these muons to the menu thresholds gives a trigger decision for the event.

Taking input from both L1Calo and L1Muon, L1Topo calculates topological variables with a more holistic view of the event. These calculations include quantities such as invariant masses of or angular separation between multiple objects, and allow to trigger on more complex signatures.

For events passing the Level-1 trigger threshold, Region of Interests (RoIs) are passed to the HLT in order to seed more complex trigger calculations.

### 2.2.5.2 High-level trigger

The HLT runs algorithms in software on a dedicated server farm, afforded looser timing constraints due the reduced input rate from the Level-1 trigger. Algorithms are grouped into ‘chains’, with each chain seeded by a Level-1 RoI. Algorithms that require less processing time are typically run earlier in the chain to enable faster rejection of bad events.

Events are organised into ‘streams’ where each stream contains events that pass a set of trigger chains. These streams give events that will pass the trigger and be saved for offline processing. The main stream (`physics_Main`) will consist of events passing the trigger menu. A subset of accepted events are sent to an express stream which is sent for immediate offline reconstruction to test data quality.

## 2.2.6 Luminosity

The luminosity recorded by the ATLAS detector is measured to understand what fraction of the delivered LHC luminosity is recorded by the detector. The precision of this measurement also has an impact on the precision of physics measurements. There are multiple methods of luminosity measurement employed by ATLAS but the primary measurement is made with the LUCID detector [37].

The LUCID detector consists of two stations 17m along the beam pipe either side of the interaction point. Each station uses a set of Cherenkov tubes to detect protons displaced through inelastic scattering. The number of detected protons should be proportional to the number of interactions per bunch crossing, on average, and thus proportional to the integrated luminosity; this is calibrated using van der Meer scans. For the Run-2 integrated luminosity, the measurement from LUCID and other sources has an uncertainty of 1.7% [39].

The total integrated luminosity recorded by ATLAS throughout Run 2 is shown in Figure 2.8. This marks the total luminosity delivered by the LHC, the amount

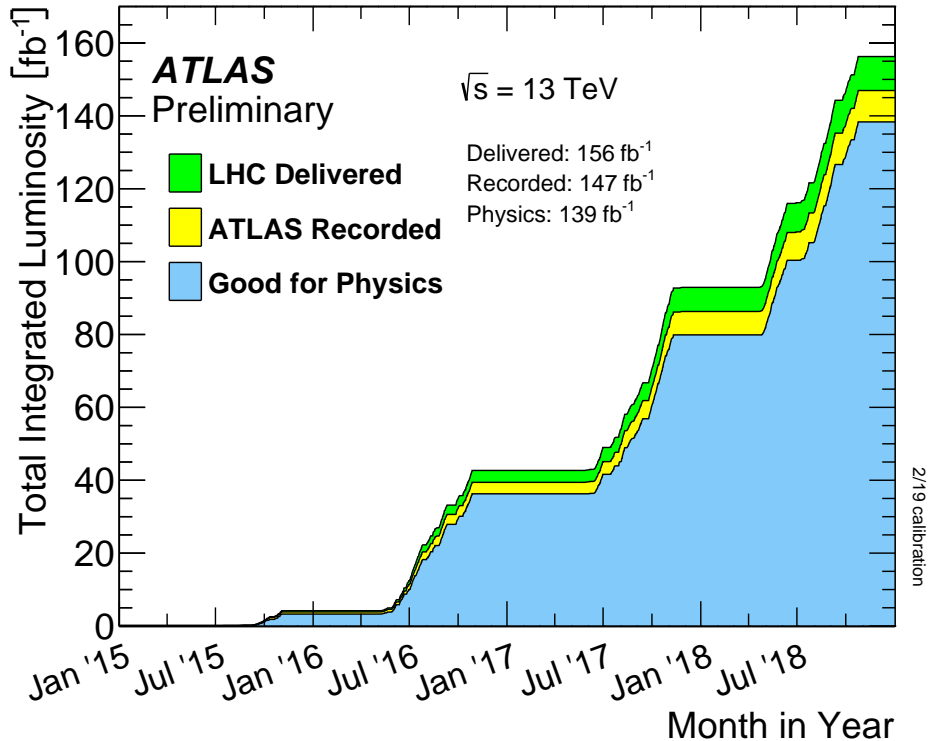


Figure 2.8: Integrated luminosity as a function of time for Run 2. Shown are the total luminosity delivered by the LHC, the luminosity recorded by ATLAS, and the amount satisfying requirements to be used for physics analyses. [38]

of that recorded by ATLAS, and the amount which is ‘good for physics’. The differences in these amounts are due to down-time in the detector or its subsystems. Events are only marked good for physics if all systems were functional, within accepted tolerances, during data-taking. The deficit in ATLAS recorded luminosity from the total delivered represents inefficiencies in data acquisition.

# CHAPTER 3

---

## Upgrading the ATLAS Level-1 Calorimeter Trigger

---

### 3.1 Evolution of the Level-1 Calorimeter Trigger

The Level-1 Calorimeter (L1Calo) system, as used for Run 2 of the LHC in the ATLAS detector, is described in Section X. This chapter focuses on work done towards upgrading this system for later LHC runs. In the long shutdown between Run 2 and Run 3, significant improvements were made to the system as part of the Phase-I upgrade. The long shutdown following Run 3 will facilitate further changes with the Phase-II upgrade, preparing L1Calo for the High-Luminosity LHC (HL-LHC) in Run 4.

Sections 3.2 and 3.3 discuss work on the Phase-I upgrade and Section 3.4 discusses work on the Phase-II upgrade, all with a focus on triggers for  $e/\gamma$  signatures. Details of the L1Calo system as implemented/planned for Phase I and Phase II, with the major changes in comparison to the Run-2 system and to each other, are given in

Sections 3.1.1 and 3.1.2 respectively.

### 3.1.1 Phase-I upgrade

The Phase-I upgrade has progressed alongside the work discussed in this chapter, to the point where the system is fully implemented and in use in Run 3 at the time of writing. The goal of the Phase-I upgrade to L1Calo is a redesign of the core components of the trigger in order to handle more data and make more refined decisions while rejecting events.

The main components introduced in the Phase-I upgrade are the Feature Extractor (FEX) systems, which replace the CP and JEP from the Run-2 system. The Electromagnetic Feature Extractor (eFEX) provides discrimination for  $e/\gamma$  and  $\tau$  objects, the Jet Feature Extractor (jFEX) focuses on jets whilst providing additional  $\tau$  identification, and the Global Feature Extractor (gFEX) triggers on large-radius jets and global quantities such as missing energy.

An overview of the Phase-I system architecture is shown in Figure 3.1. The key change to the  $e/\gamma$  signature trigger is that it now receives digital information from the LAr Calorimeter in the form of SuperCells, rather than the analogue tower energies that were available to the Run-2 system. This information is processed by the eFEX to generate Trigger Objects (TOBs), equivalent to the RoIs generated by the CP in Run 2.

The move to digital input comes with an increase in granularity, a trigger tower now being split in both  $\eta$  and calorimeter layer to give up to 10 SuperCells: typically one SuperCell each from Layers 0 (presampler) and 3 and four SuperCells each from Layers 1 and 2, segmented in  $\eta$ . Each SuperCell is formed by summing energies from between four and eight calorimeter cells. This division of a tower into SuperCells is shown in Figure 3.2. The granularity received from the Tile Calorimeter is the same as in Run 2, the energy in a tower (this is later referred to as Layer 4).

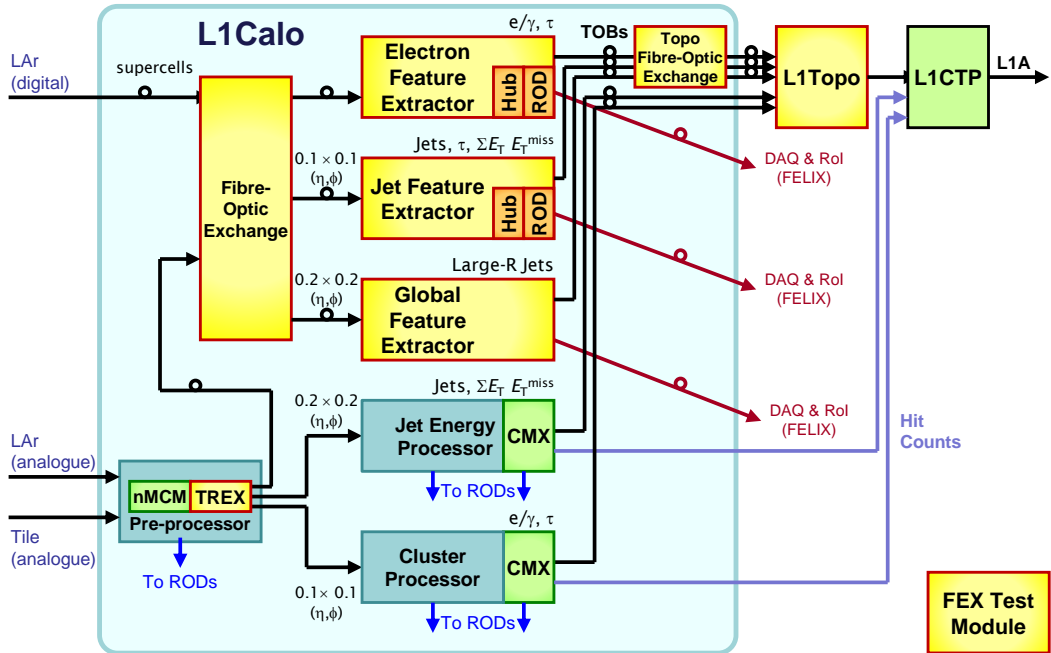


Figure 3.1: Diagram showing the L1Calo modules in use for Run 3 of the LHC. Gold rectangles represent modules introduced in the Phase-I upgrade. Blue and green rectangles represent existing components from the Run 2 system, included still as part of the trigger whilst transitioning to the new system. [40]

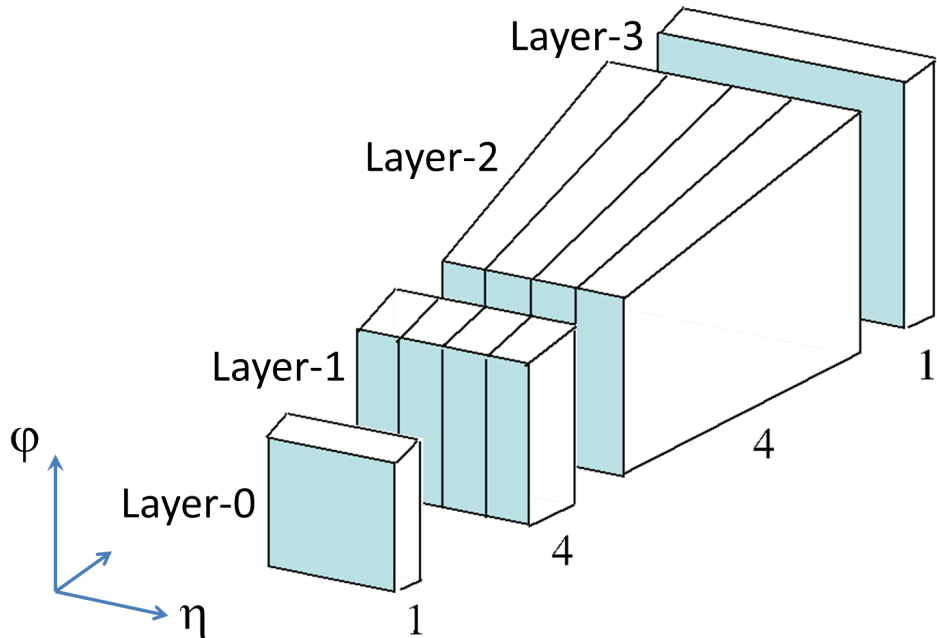


Figure 3.2: Diagram showing division of a single trigger tower into SuperCells. [41]

The eFEX introduces new algorithms to use the SuperCell information in order to trigger on  $e/\gamma$  objects. In comparison to the CP in Run 2 which calculates a cluster energy and a single isolation value, the eFEX calculates three separate variables used to identify and isolate a candidate object and can also more accurately calculate the energy from SuperCell information.

To calculate any of these variables a seed SuperCell is first identified, as the highest energy SuperCell in Layer 2 of the calorimeter compared to the surrounding region. The energy of the cluster is calculated by summing the energy of the seed with its highest energy neighbour in  $\phi$  and both neighbours in  $\eta$ , adding also the six corresponding SuperCells in Layer 1, and the two SuperCells from Layers 0 and 3 that are in the same tower as the seed. The three other discriminating variables are calculated as follows:

$$R_\eta = \frac{\text{energy in } 3 \times 2 \text{ area of cells}}{\text{energy in } 7 \times 3 \text{ area of cells}},$$

with each area (in  $\eta \times \phi$ ) centred on the seed and calculated in Layer 2;

$$R_{\text{had}} = \frac{\text{core energy}}{\text{environment energy}},$$

where the core energy is calculated in the same manner as for the cluster energy but including both neighbours in  $\phi$  (so a  $3 \times 3$  area of SuperCells in Layers 1 and 2 and a  $1 \times 3$  area in Layers 0 and 3) and the environment energy is the energy in a  $3 \times 3$  tower area in Layer 4 (i.e. the hadronic calorimeter); and

$$w_{s,tot}^2 = \frac{\sum_i i^2 \cdot E_i}{\sum_i E_i},$$

where  $i \in [-2, 2]$  is the  $\eta$  coordinate of the SuperCell relative to the seed, calculated for SuperCells in Layer 1 with both neighbours in  $\phi$  also summed for each  $E_i$ . Visual representations of the areas included for these algorithms are presented alongside the work done in Section 3.2.

Candidate  $\tau$  particles considered by the eFEX have a similar set of variables (cluster

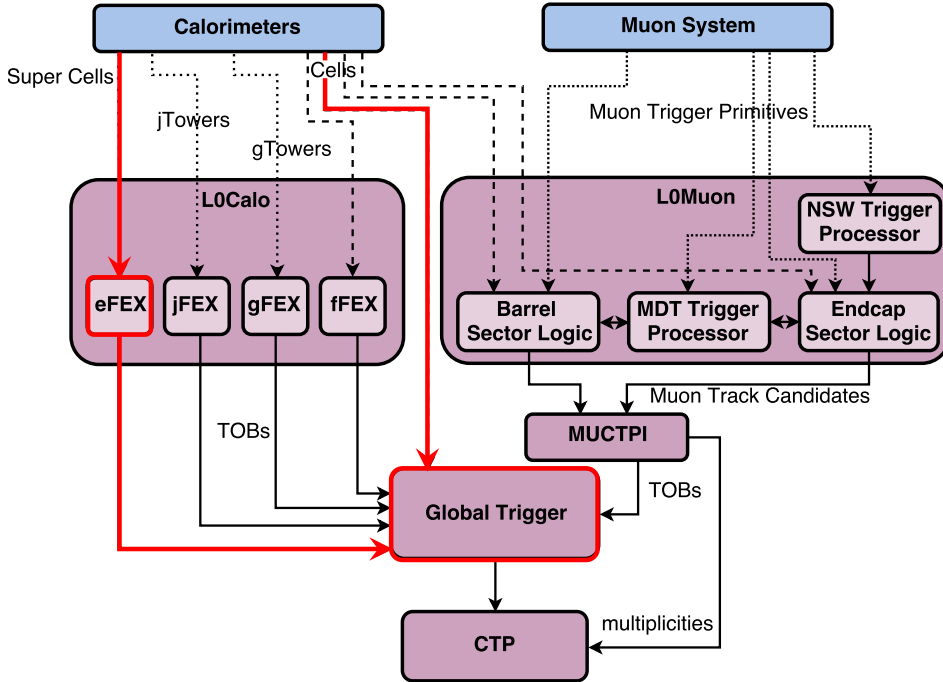


Figure 3.3: Schematic of the ATLAS hardware trigger as planned for the Phase-II upgrade in Run 4 of the LHC. The red lines highlight the main parts relevant to the  $e/\gamma$  trigger, with the addition of the Global Trigger being the main change with respect to the Phase-I system. [42]

energy,  $R_\eta$ , and  $R_{\text{had}}$ ) with small differences in the areas used in their calculation.

### 3.1.2 Phase-II upgrade

As luminosity and pileup is increased even further with the high-luminosity era of the LHC in Run 4, the trigger needs to be further improved to operate in increasingly difficult conditions. The Phase-II upgrade to the hardware trigger aims to do this primarily by adding a new component, the Global Event Processor (GEP) (or Global Trigger). The GEP will be downstream of the Phase-I FEX modules, which will continue to contribute to the trigger, and will refine decisions made by employing additional information: information from a larger area than typically available to a single FEX but also finer in granularity.

An outline of how the GEP fits in with the existing systems is shown in Figure 3.3. Information from the calorimeters will be sent directly to the GEP in finer granularity than is available to the eFEX, with energies in each individual cell without them being grouped into SuperCells. This gives a 4-8 times increase in granularity, depending on the region of the calorimeter.

The additional information available to the GEP means it can work together with the eFEX. The eFEX will create TOBs with associated variables (discussed in Section 3.1.1) which are sent to the GEP, which can then further probe the same region of the calorimeter to determine if the candidate object should be accepted. The algorithms used by the GEP to do this are the topic of the study in Section 3.4.

## 3.2 Visualisation of eFEX inputs and algorithms

In order to aid in debugging minor differences between different implementations of eFEX algorithms, an algorithm visualisation program was created. The program reads input data and performs aspects of eFEX algorithms whilst also providing a visual representation of what the algorithm is doing and where the result comes from.

The visualiser is written in JavaScript, using Node.js to interface with some server-side C++ scripts, needed to access energy decoders from online software, and Express.js to handle the web-based User Interface (UI).

### 3.2.1 Motivation

During development of algorithms for the hardware trigger, each algorithm is implemented multiple times. First, algorithms will be implemented in offline software to be tested and tuned against simulations or existing data. Then, in order to run on hardware, the algorithm needs to be ported to firmware. Often, to provide closer

cross-checks of the firmware algorithms, they are also simulated in online software. Inevitably, due to software and firmware bugs, subtle differences will exist between these algorithms; these differences need to be understood and corrected to have a complete bug-free implementation.

The need to find these subtle differences between algorithms motivates the visualisation software discussed here. Although at first it seems illogical to add an additional, independent, implementation of the algorithm (since the issue is in part due to having multiple different implementations), the added visualisation aspect makes it easier to understand where a particular algorithm implementation might have gone wrong in cases where there are discrepancies. This has been demonstrated through the use of the visualisation software in tests, discussed in Section 3.2.5.

### 3.2.2 Input Data

The visualisation software takes as input the calorimeter energies visible to a single eFEX Field-programmable Gate Array (FPGA). This covers a  $6 \times 10$  area in  $\eta \times \phi$  of trigger towers, with each tower being split into SuperCells across 5 calorimeter layers, as described in Section 3.1.1. For each event, the input data provides one energy value per SuperCell, encoded with either LAr or Tile energy encoding.

From this input data, a  $3 \times 3$  area of trigger towers, centred on an  $(\eta, \phi)$  coordinate provided by the user, is extracted and displayed on-screen. This area covers all energy values used for eFEX algorithms if the seed of the TOB is located in the central trigger tower.

### 3.2.3 User Interface

The eFEX Visualiser program provides a minimal UI to explore input data and results of the eFEX algorithms. The basic interface is shown in Figure 3.4. It prompts the user to specify an input file,  $(\eta, \phi)$  centre-tower coordinates, and an

event number, then on receipt of these inputs it reads the information and displays the requested energies in a grid.

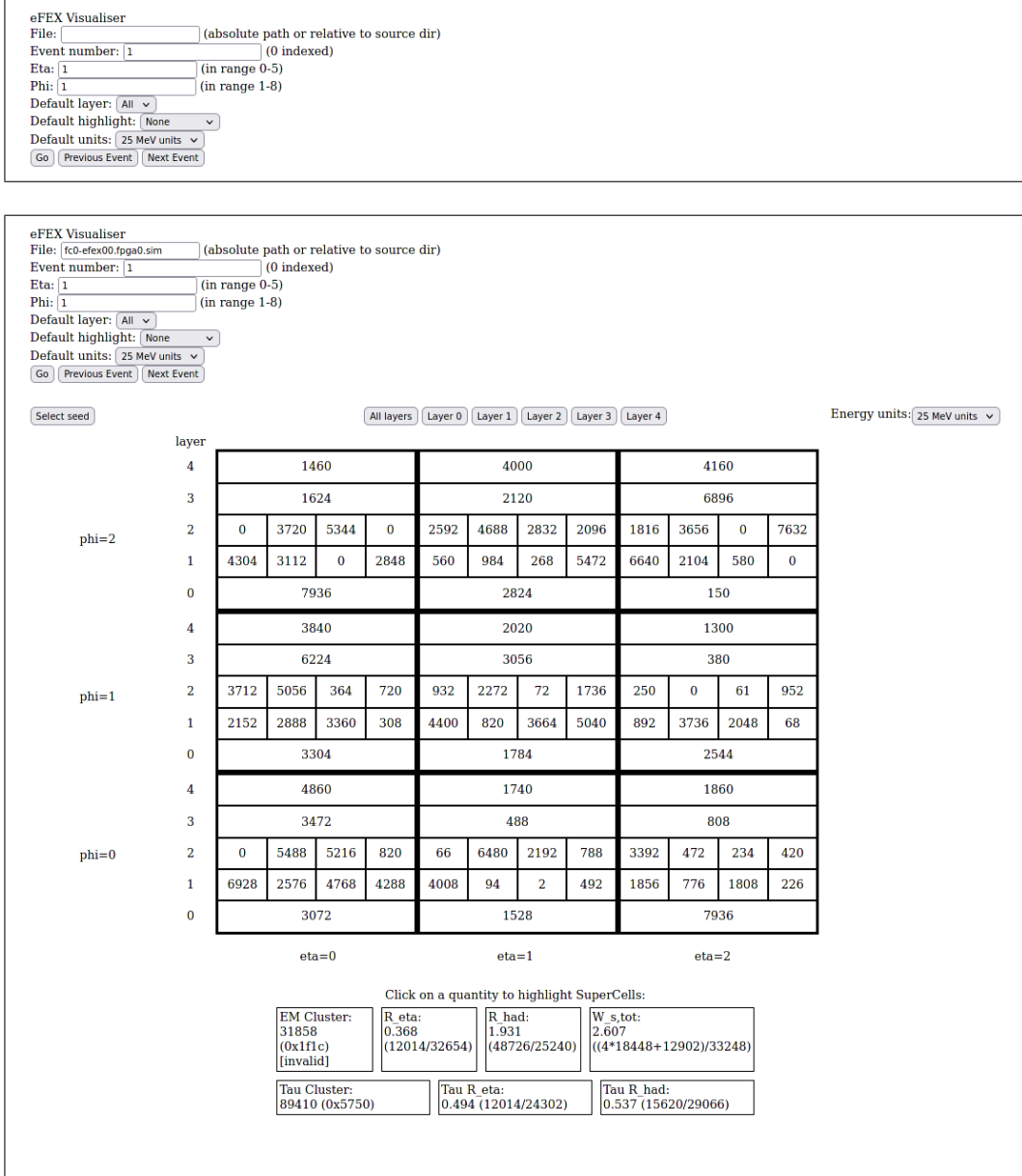


Figure 3.4: Initial interface on launching the eFEX Visualiser program (top) and the default view once data is read from a file (bottom).

The full interface becomes visible after the grid is displayed. The grid itself is a  $3 \times 3$  area divided by bold lines, with each square representing a trigger tower, and each trigger tower square divided further into SuperCells. The horizontal axis represents the  $\eta$  coordinate of the tower or SuperCell, and the vertical axis represents the  $\phi$  coordinate. These coordinates are labelled with the same indices the user gave as

initial input. In order to show all layers simultaneously, in the default view layers are stacked on top of each other, in the phi axis, within each tower. Controls are provided to instead view each layer individually if preferred.

Below the grid, a list of all the quantities calculated for the current TOB is displayed. Clicking on one of these quantities will highlight all of the SuperCells involved in the calculation. The details of how these values are calculated and how the algorithms are visualised are discussed in more detail in Section 3.2.4.

Above the grid, alongside the layer selection buttons, are options to manually set the seed SuperCell and to select the units used to display energies. The unit selection input is a drop-down box that allows the user to choose between 25 MeV (default units in firmware) or GeV units. Changing this option instantly updates all displayed energies. Pressing the “Select seed” button will toggle the layer view to display Layer 2, prompt the user to click on the SuperCell with the highest energy, and then on its  $\phi$ -neighbour with the highest energy. This aids the user in selecting the correct seed for TOB generation, but is not normally necessary as the program will apply these criteria to automatically set the seed as soon as the grid is loaded. The manual override is included in case the automatic selection is wrong, or if looking at algorithms with a different seed may help debugging.

### 3.2.4 Algorithms

For each TOB processed (i.e. each particular event, coordinate location, and seed), several algorithms are run to calculate the quantities displayed on-screen. These are the same algorithms used by the eFEX to calculate TOB energies and isolations. The following variables are calculated: EM cluster energy, EM  $R_\eta$ , EM  $R_{\text{had}}$ , EM  $w_{s,\text{tot}}$ , tau cluster energy, tau  $R_\eta$ , and tau  $R_{\text{had}}$ . All of these are either sums of SuperCell energies (EM and tau cluster energies), ratios of sums of SuperCell energies ( $R_\eta$  and  $R_{\text{had}}$ ), or a ratio with weighted sums ( $w_{s,\text{tot}}$ ).

The values of these variables are calculated immediately after the data for a given

TOB is collected, or once the seed is re-specified, and displayed on-screen below the grid. If the user clicks on a displayed quantity, the SuperCells involved in the sums for the corresponding algorithm are highlighted with colours corresponding to whether those cells are used in the numerator (lime green); the denominator (gold); or, in the case of  $w_{s,\text{tot}}$ , in the numerator with a larger weight (dark green). Figures 3.5 and 3.6 demonstrate the highlighting for all of the algorithms.

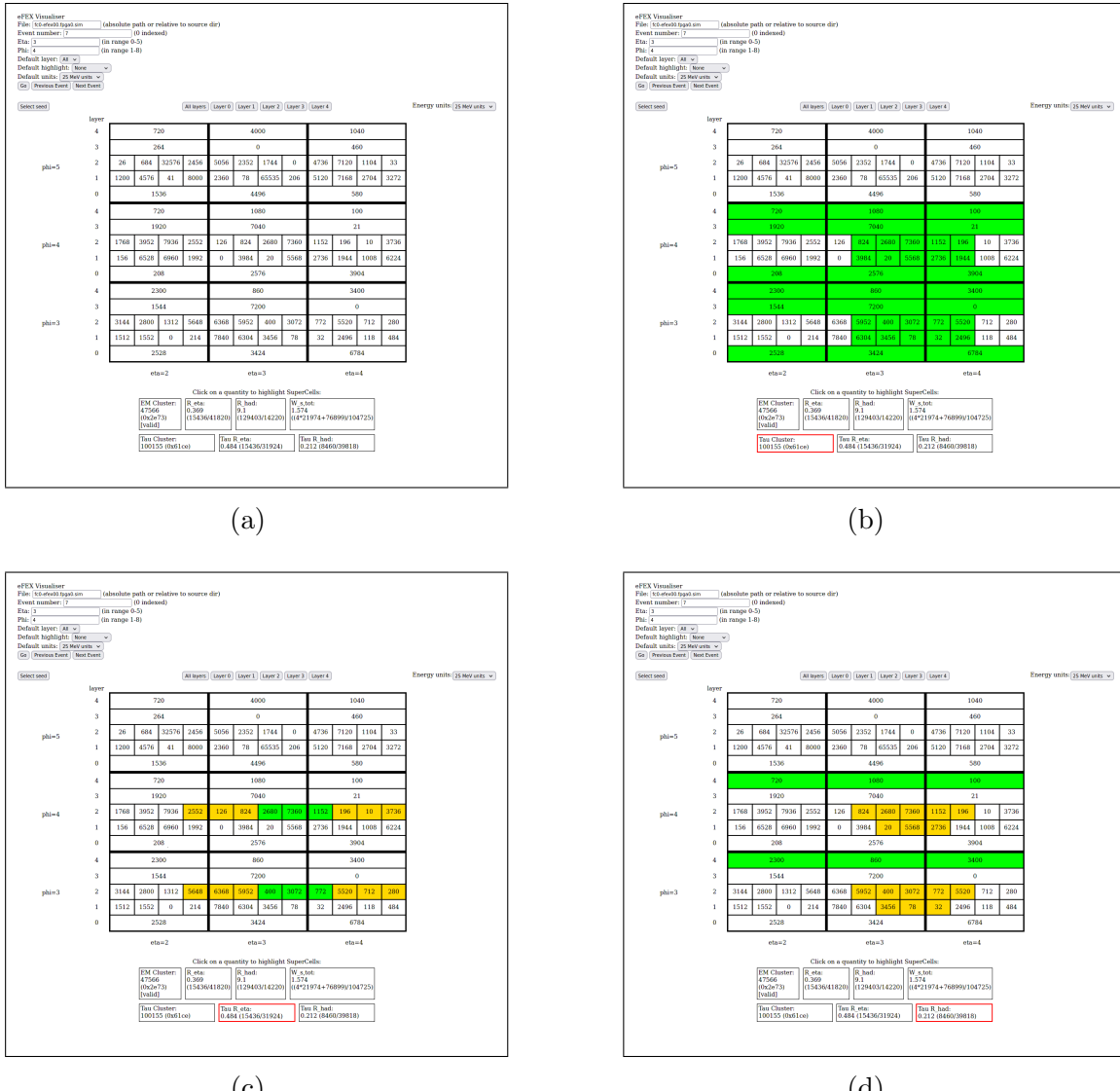


Figure 3.5: Demonstration of highlighting used to visualise algorithms, all shown for the same TOB. Showing (a) initial view without highlighting, (b) highlighting for tau cluster energy, (c) highlighting for tau  $R_\eta$ , and (d) highlighting for tau  $R_{\text{had}}$ .

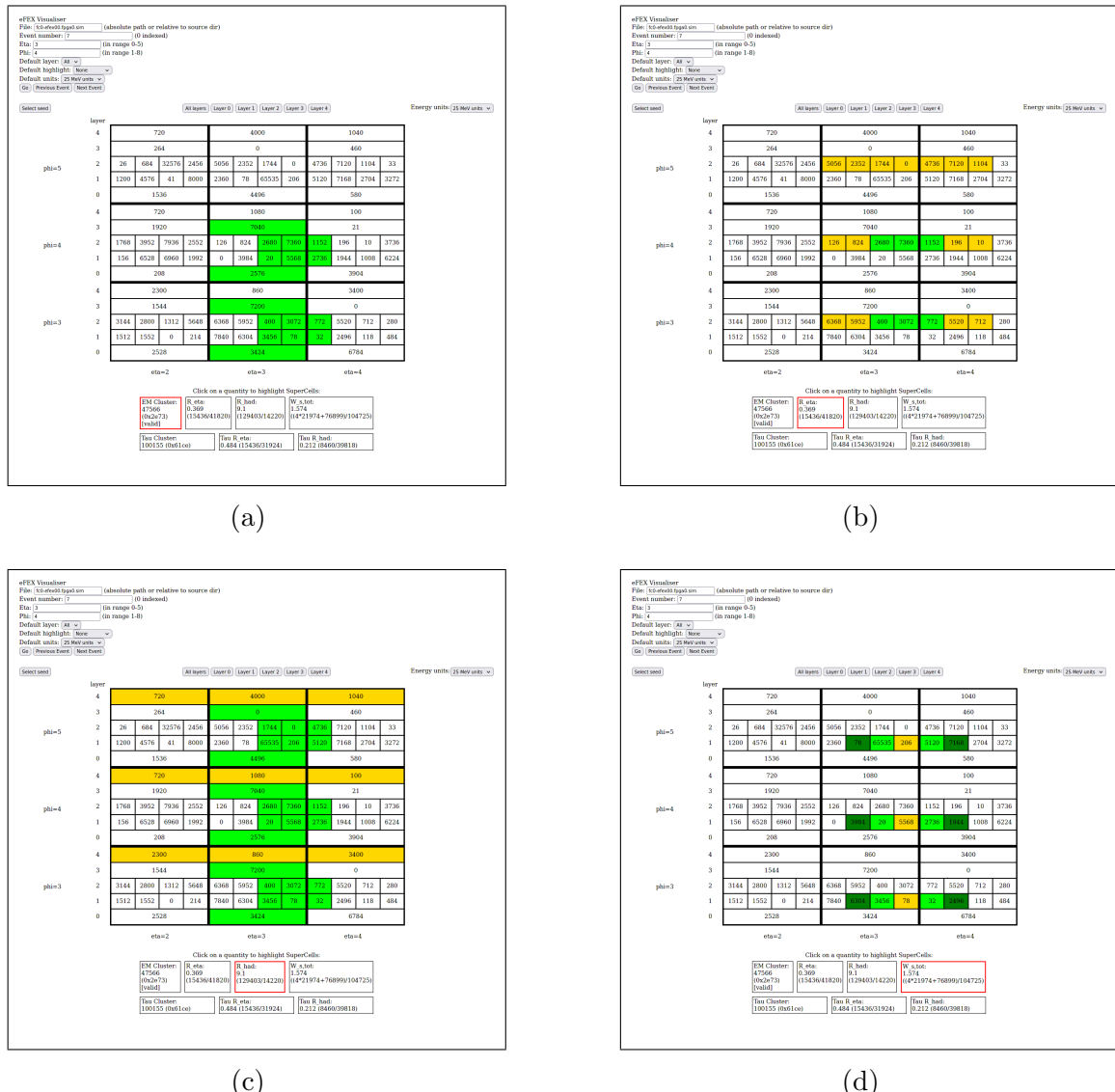


Figure 3.6: Demonstration of highlighting used to visualise algorithms, all shown for the same TOB. Showing (a) highlighting for EM cluster energy, (b) highlighting for EM  $R_\eta$ , (c) highlighting for EM  $R_{\text{had}}$ , and (d) highlighting for EM  $w_{s,\text{tot}}$ .

### 3.2.5 Usage

The visualisation tool was used at several stages during commissioning of the eFEX. Primarily it was used to compare firmware algorithms to their implementation in online software. Each time there was a difference found between the two, the event could be checked with the visualiser to help determine which of them was correct and to work out how the other might have gone wrong.

Once there was sufficient confidence in the similarity between online simulation and firmware implementations, the visualiser was again used to help in tests comparing online and offline simulations. The same technique was applied here to help ensure offline simulations were running with the same results as their online equivalent, and to help find errors in cases where they were not.

## 3.3 Analysis of early Run-3 data for commissioning

At the start of Run 3, the Phase-1 L1Calo trigger was being used for the first time, having just been installed in the ATLAS detector. In these early stages, the new Phase-1 system was running in parallel to the Run-2 system, but the Run-2 system was still being used in the trigger menu over the new system.

One of the key goals of this time period was validating the Phase-1 trigger system, comparing it to the Run-2 system to identify any differences which may have arisen from bugs or hardware issues. This section describes analysis of some early Run-3 data contributing to this goal.

### 3.3.1 Data

Two runs were used to provide the data for this analysis: Run 423433, taken on 31 May 2022, and Run 427885, from 10 July 2022. These runs were taken in quite

different conditions, the first with lower intensity beams and no stable beam conditions, and the second with high intensity stable beams. Notably, the second of these runs had bunch trains with 25 ns separation between bunches, whereas the first had only isolated bunches.

Events are taken from the `physics_Main` stream. This stream contains 1,636,636 events for Run 423433 and 107,016 events for Run 427885.

### 3.3.2 TOB and RoI selection

Phase-1 TOBs and Run-2 RoIs in events are compared to find instances in the same event that have the same, or very similar,  $\eta$ - $\phi$  coordinates. A pair is formed by selecting, for each TOB, the nearest RoI that has not already been matched to a TOB. A match is considered to be a pair of objects within  $\pm 1$  trigger tower in both  $\eta$  and  $\phi$ , i.e. a TOB matches an RoI if it falls within the  $3 \times 3$  area of trigger towers centred on the tower containing the RoI. Matched objects are considered to be the same physics object, identified independently by both systems. Instances where there is a TOB or RoI with no analogue in the opposing system are also tracked.

Only the barrel region was considered for this as a preliminary investigation, since it has a simpler geometry and as such it is easier to isolate bugs. Also, at the time of analysing, only half of the eFEX modules were installed so the Phase-1 system had coverage for half of the  $\phi$  range; only RoIs inside of this coverage are accepted.

### 3.3.3 Results

From the 1,636,636 events in Run 423433, 292,498 RoI/TOB pairs are selected. Of these, 271,854 matched in  $\eta - \phi$  coordinates, giving a total match rate of 93%. For Run 427885, 22,337 of 27,973 pairs were matched for a match rate of 80%. Figures 3.7 and 3.8 show the match rate for objects in Run 427885 as a function of energy, using Cluster-processor Module (CPM)-measured and eFEX-measured

energies respectively. This shows that the bulk of the mismatches come from low-energy objects, with a notably higher match rate at higher energies. At all energies the match rate is worse here than in the earlier run.

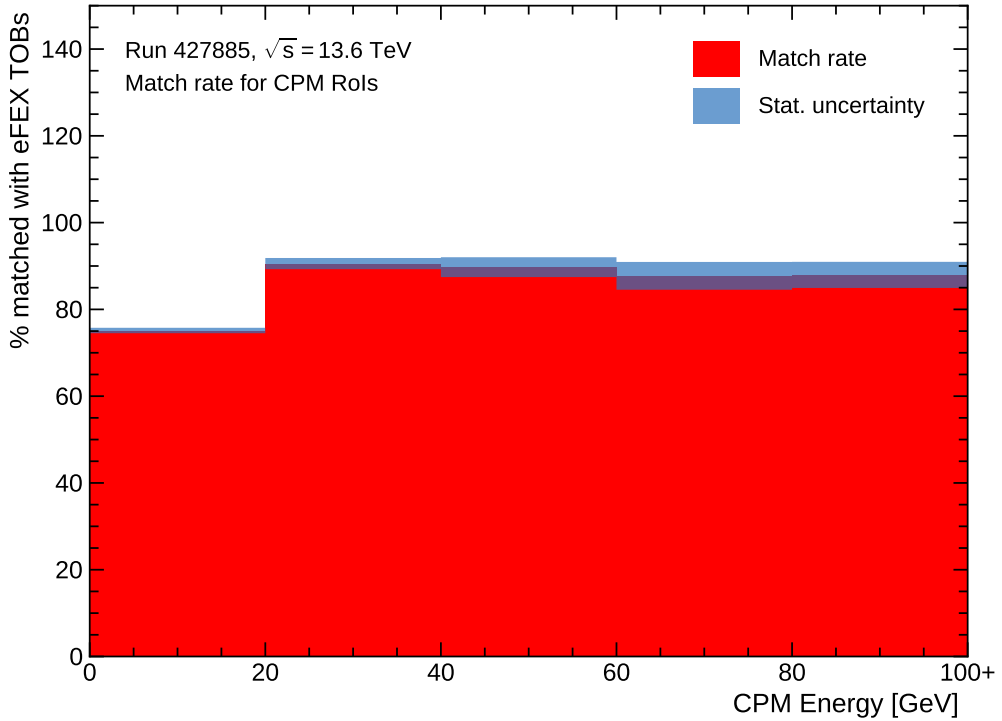


Figure 3.7: Match rate for TOBs/RoIs as a function of energy as measured by the CPM. Objects grouped in 20 GeV bins, with the last bin including all overflow.

Figures 3.9 and 3.10 compare the energies recorded by the Run-2 and the Phase-1 systems for matched objects in the two runs. In Run 423433 it is clear that the majority of matched objects have approximately the same energy, with an additional cluster where in a few cases the eFEX-measured energy is much lower than the CPM-measured.

In the later run, Run 427885, however, there is no longer such a strong correlation in energies. It seems that in general the eFEX energies are lower than the CPM energies – seen by the gradient of the area containing the majority of objects being less than the equal-energies line. Once again there is another cluster of objects with very low eFEX energies at high CPM energies.

The general trend is a high but imperfect match rate and decreased performance in

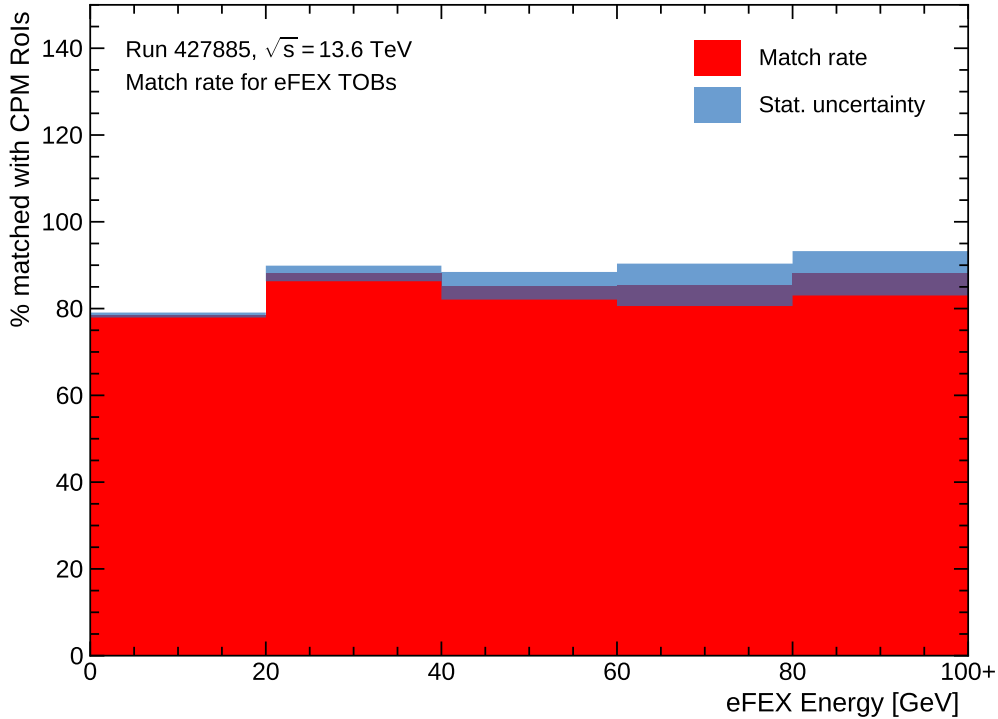


Figure 3.8: Match rate for TOBs/RoIs as a function of energy as measured by the eFEX. Objects grouped in 20 GeV bins, with the last bin including all overflow.

the later run compared to the earlier run, both in terms of match rate of objects and energy correlation between the two systems. From this information, issues in the system could be identified and solved. In the case of the degraded performance for Run 427885, the different beam conditions in this run (bunch trains, that were not present for Run 423433) were deemed to have caused issues with the Bunch Crossing ID (BCID) on the Liquid Argon Trigger Optical Mezzanine (LATOME) modules providing the eFEX with digitised energies from the calorimeter.

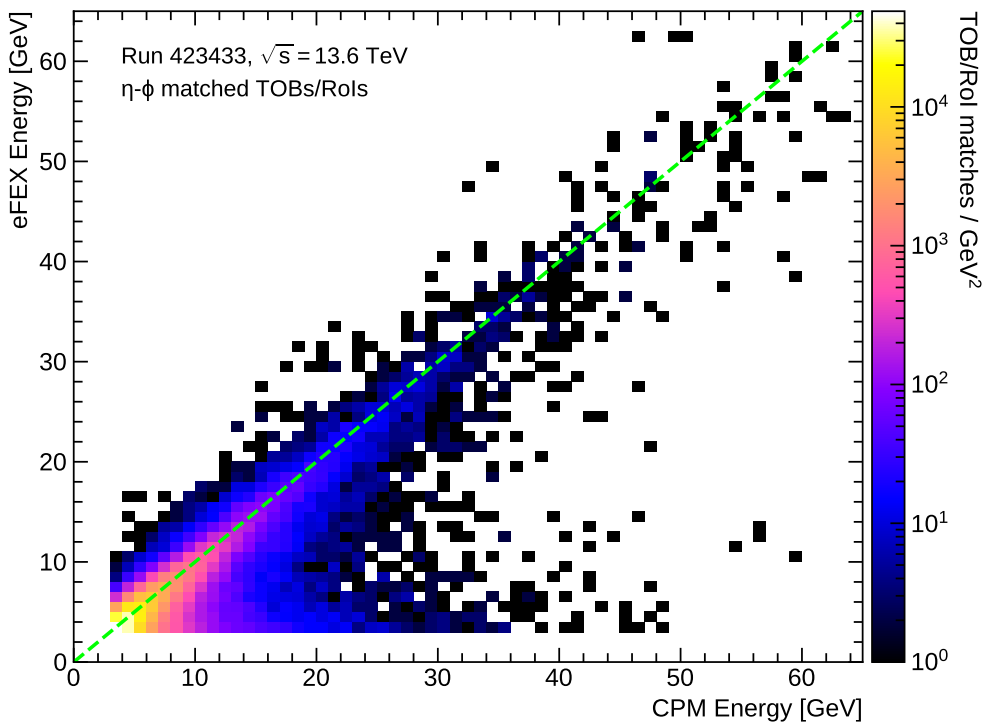


Figure 3.9: Comparison of energies for matched TOBs/RoIs with the energy as measured by the CPM given on the  $x$ -axis and as measured by the eFEX on the  $y$ -axis. Contains data for all matched objects in Run 423433. The dashed line marks the set of points where the CPM and eFEX energies are equal.

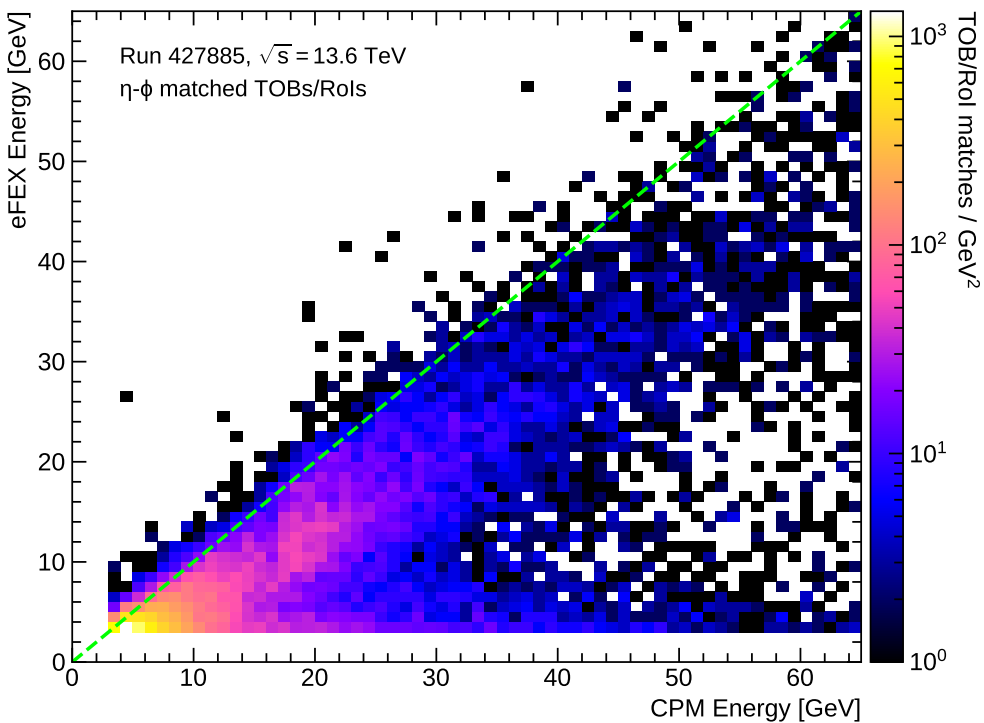


Figure 3.10: Comparison of energies for matched TOBs/RoIs with the energy as measured by the CPM given on the  $x$ -axis and as measured by the eFEX on the  $y$ -axis. Contains data for all matched objects in Run 427885. The dashed line marks the set of points where the CPM and eFEX energies are equal.

## 3.4 Performance studies of electron and photon algorithms for the Global Event Processor

### 3.4.1 Introduction

The GEP, when introduced in the Phase-II upgrade, will aim to improve discrimination in the hardware trigger for many signatures, but notably for  $e/\gamma$  objects. The GEP will be working alongside the eFEX system, introduced in Phase I, but will have access to more information, giving it potential to improve upon decisions made by the eFEX. To realise this improvement, new algorithms will need to be implemented in the GEP to take advantage of the finer granularity information available to it.

Designing algorithms to be used in future hardware systems is achieved through prospective performance studies. Performance studies use simulations of the expected response of a system to evaluate the performance of individual algorithms. These studies benefit from the ease of implementation of algorithms in high-level software but it is still important to consider the complexity of implementation in firmware when designing algorithms. Performance studies are typically the first step in designing a system as evaluating performance in simulations before a system is built can inform the design of the hardware.

This section explores the specific implementation and possible performance of the  $E_{\text{ratio}}$  algorithm in the GEP, expected to significantly improve discrimination for  $e/\gamma$  by making use of fine granularity input information [42, p. 126]. Section 3.4.2 details the samples used for evaluating algorithm performance, Section 3.4.3 discusses how the GEP itself is simulated, Section 3.4.4 gives metrics used to evaluate performance, then Section 3.4.5 goes through the process of designing an algorithm, the outcome of which is evaluated in Section 3.4.6.

### 3.4.2 Monte Carlo samples

Simulations used for the performance studies presented here are from two Monte Carlo samples: a  $Z \rightarrow ee$  sample providing signal EM objects that the trigger should be accepting, and a minimum bias QCD sample providing background objects, typically low-energy jets, that the trigger should be rejecting. The signal sample is generated by POWHEG [15] and PYTHIA [43], and the background sample is generated by PYTHIA.

After being processed by the typical ATLAS detector simulation (see Section X), additional simulations of the upgraded trigger are performed by the Phase-I offline software in order to simulate the eFEX response to each event.

### 3.4.3 Phase-II simulation

Producing prospective results for the Phase-II trigger requires simulation of the requisite algorithms. On top of the existing simulations of the Phase-I simulations, two things are needed to produce the results possible with Phase II: collection of the higher granularity calorimeter data that will be available to the GEP, and any algorithms that the GEP will run on its input data.

The first of these tasks is done by taking the location of  $e/\gamma$  candidate TOBs identified by the simulated eFEX, collecting calorimeter cell energies in a region around this location, and storing it in a cluster. This method was chosen over storing calorimeter cell output in the entire detector to reduce computing requirements. The size of stored clusters is  $0.3 \times 0.3$  in  $\eta \times \phi$ , centred on the seed TOB location, chosen conservatively to be sufficiently large that it will contain all information required by any algorithm.

Samples with these clusters of high-granularity calorimeter data included are then used for developing prospective algorithms for the GEP, explored in detail in Section 3.4.5.

### 3.4.4 Performance benchmarks

These studies focus on performance of the  $e/\gamma$  trigger at hardware level. As such, the goal is to maintain a signal efficiency, fraction of signal events selected by the trigger, as high as possible. At the same time the amount of background being rejected should be as high as possible; this responds to maximising the background rejection, where

$$\text{background rejection} = \frac{1}{\text{fraction of background events selected}}.$$

Both signal efficiency and background rejection will be dependent on the selections made by different algorithms. To compare algorithms, or different variants of an algorithm, both of these quantities must be considered. The typical benchmark used in these studies will be the background rejection at 95% signal efficiency.

### 3.4.5 $E_{\text{ratio}}$ algorithm design

The focus for this study is on the impact of a single variable in  $e/\gamma$  discrimination,  $E_{\text{ratio}}$ .  $E_{\text{ratio}}$  is a shower-shape variable, already used in the HLT. The definition used here is

$$E_{\text{ratio}} = \frac{E_2}{E_1} \tag{3.1}$$

where  $E_1$  and  $E_2$  are the first and second most energetic cells in Layer 1 of the EM calorimeter in an area around the centre of the shower.<sup>1</sup>

The  $E_{\text{ratio}}$  variable is designed to discriminate against substructure in a shower. A shower with multiple distinct branches (e.g.  $\pi^0 \rightarrow \gamma\gamma$ ) might produce two peaks of similar energy and give an  $E_{\text{ratio}}$  value close to one, whereas a shower with a single peak (as expected from  $e/\gamma$  clusters) would give an  $E_{\text{ratio}}$  value close to zero.

---

<sup>1</sup>This is different to the definition used in the HLT, which instead is  $E_{\text{ratio}} = (E_1 - E_2)/(E_1 + E_2)$ . The simpler definition is preferred here in the spirit of reducing calculation in firmware, though the two forms are a transformation of one another.

Calculating this variable in high-level software is straightforward and requires no optimisation. However, identifying the two required maxima involves a large number of comparisons between cell energies. An algorithm developed to run on hardware should be as simple as possible, therefore designing an alternate implementation is beneficial to minimise the impact of this algorithm on the latency of the GEP system.

A simple approach to finding the two highest energy cells in a cluster is to form a sorted list of all energies from Layer 1 cells, or at least sufficiently sorted to be confident in the highest two energies. Sorting algorithms are a very well-understood problem and heavily optimised but this approach is very rigid, not allowing for any tuning of the algorithm. For example, a cluster may have no substructure but fall on the boundary between two cells, depositing a similar amount in each. This would result in a high, background-like,  $E_{\text{ratio}}$  value. To avoid this the algorithm could include a minimum distance between cells considered to be the two maxima, or try to identify minima between the two, this would greatly complicate a list-sorting approach.

The most complete, but resource-heavy, method might consist of fitting some functional form to the energies as a function of  $\eta$  and  $\phi$  to extract the peak energies. This might work in software but is very computationally expensive, even if possible to implement in firmware it is likely not worth the latency it would require.

The desired solution is an algorithm for calculating an  $E_{\text{ratio}}$ -type variable that comes somewhere between these two options, more adaptable than the list-sorting approach and less resource-heavy than the peak fitting. The following sections explore such an algorithm: a baseline algorithm for finding secondary maxima in clusters in the GEP is established in Section 3.4.5.1; parameters of the algorithm are tuned using simulations in Sections 3.4.5.2, 3.4.5.3, and 3.4.5.4; and a summary of the results and recommended parameters, as well as additional adjustments that could be made with further studies, is given in Section 3.4.6.

### 3.4.5.1 Initial algorithm

Identifying the two highest energy cells is done in three stages: locating the seed, identifying candidate secondary maxima, and comparing results.

The GEP will receive a seed location from the eFEX identifying which SuperCell has the highest energy. The cells within this SuperCell are compared with one another to find which has the highest energy, this becomes the seed cell for the  $E_{\text{ratio}}$  algorithm.

The algorithm will then perform a stepwise search from the seed outwards to identify peaks in energy. On each step the energy gradient is calculated as  $\Delta E = E_{\text{next}}^{\text{cell}} - E_{\text{prev}}^{\text{cell}}$ , where  $E_{\text{next}}^{\text{cell}}$  is the energy of the cell being stepped to, and  $E_{\text{prev}}^{\text{cell}}$  is the energy of the cell being stepped from. From the first step  $\Delta E$  should be negative, as the seed will have a higher energy than the surrounding cells, but on subsequent steps  $\Delta E$  may become positive, marking that a minimum-energy point has been passed. If, after this,  $\Delta E$  becomes negative again it indicates that the previous cell was a local maximum; in this case that cell is added to a list of candidate secondary maxima, and the search stops along this route. If the edge of the available range of cells is reached before  $\Delta E$  turns positive then no candidate is saved. If the edge is reached after  $\Delta E$  turns positive, but before it turns negative again, then the last cell in the range is taken to be the candidate.

This stepwise search is done in 6 different routes from the seed: one route where each step from the seed is in positive  $\eta$ , one in negative  $\eta$ , two where the first step is in positive  $\phi$  before proceeding in positive or negative  $\eta$ , and two following the same pattern with the first step in negative  $\phi$ . Figure 3.11 cells, alongside a schematic depicting the peak location strategy.

Once the stepwise search is complete, up to 6 candidate secondary maxima will have been identified. The candidate with the largest energy is taken as the secondary maximum and, with the seed as the maximum,  $E_{\text{ratio}}$  can be calculated using Equation 3.1.

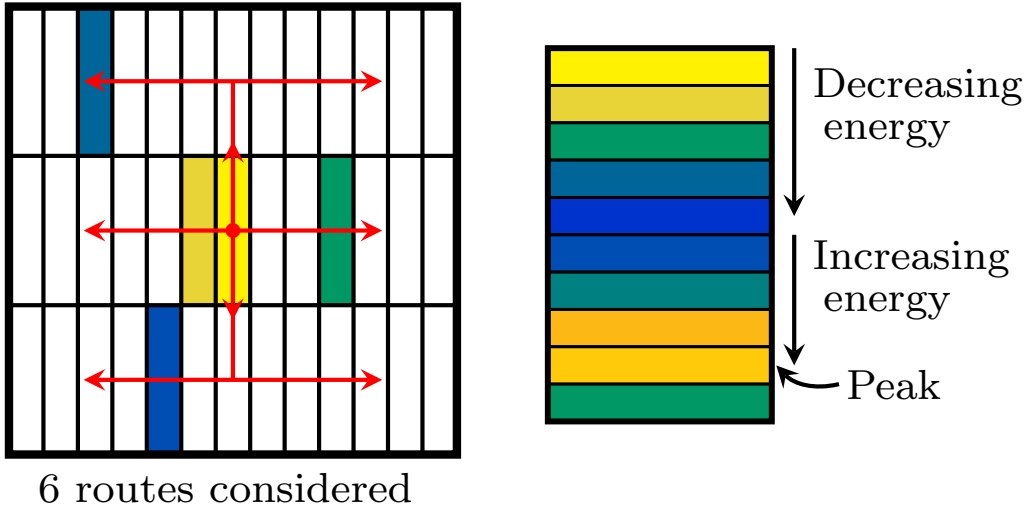


Figure 3.11: Diagram showing the 6 different routes in which the  $E_{\text{ratio}}$  algorithm searches for secondary maxima (left) and how the algorithm identifies secondary maxima by tracking energy gradients along each step (right).

The performance of this baseline algorithm was investigated using simulations. Figure 3.12 shows the results, comparing the response in signal and background as a function of the calculated  $E_{\text{ratio}}$  value and the fraction of each that would pass a given  $E_{\text{ratio}}$  threshold. The background rejection as a function of signal efficiency is also shown, the baseline algorithm achieves a background rejection of 2.3 at 95% signal efficiency.

### 3.4.5.2 Peak size

The first parameter to investigate is the size of the area used to calculate energies. In the algorithm as described in Section 3.4.5.1, the energies used in comparisons and in the final  $E_{\text{ratio}}$  calculation are always the energies of a single cell. This could be modified by instead summing the energy of a cell with that of its neighbours in  $\eta$  to reduce sensitivity to small fluctuations. The number of cells summed is labelled the ‘peak size’, where the default algorithm would have a peak size of one. With a peak size greater than one the algorithm uses a ‘sliding window’ approach, so the step size is still a single cell despite the energy value coming from a larger area. For

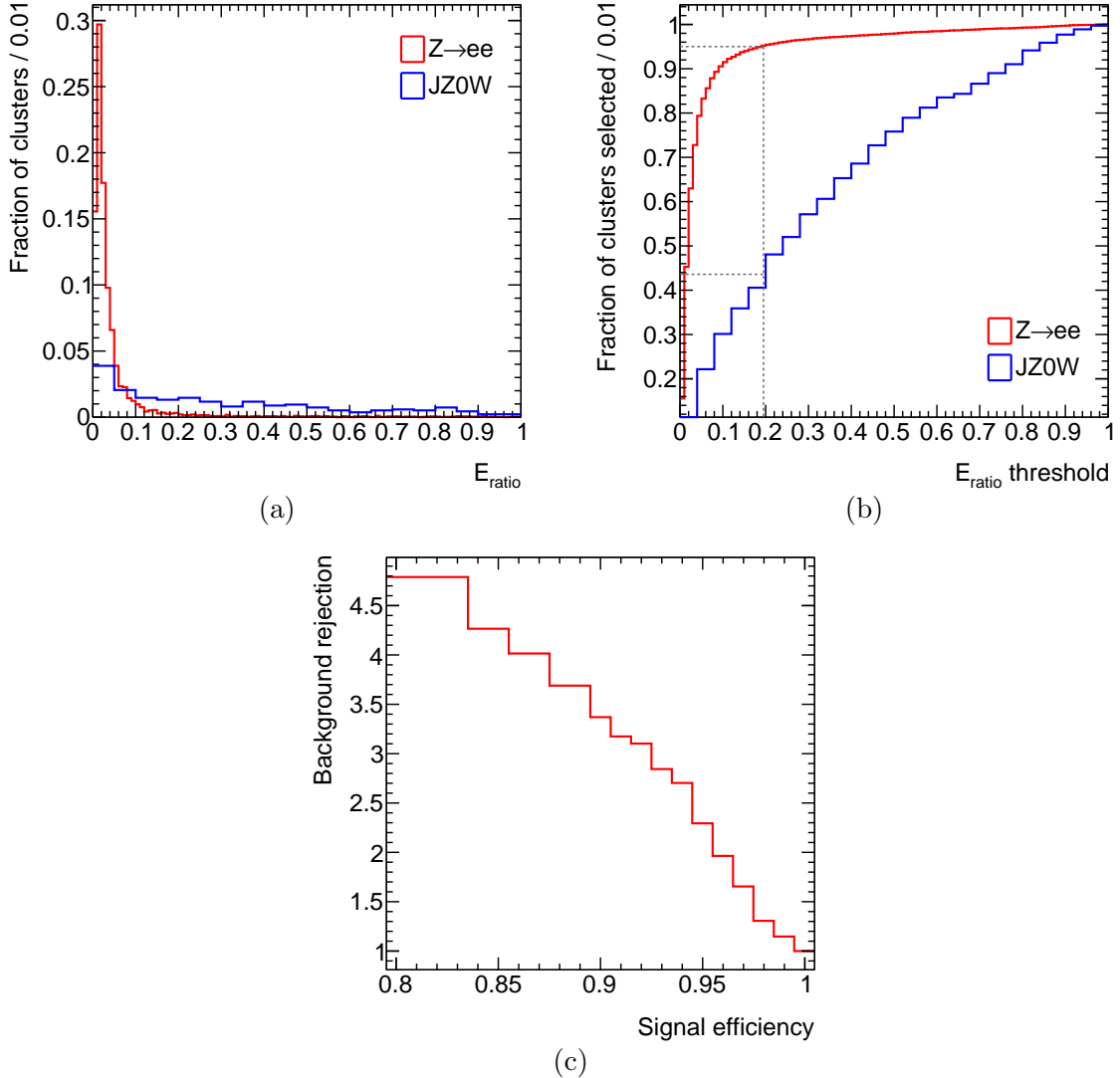


Figure 3.12: Performance of baseline  $E_{\text{ratio}}$  algorithm on signal ( $Z \rightarrow ee$ ) and background ( $JZ0W$ ) clusters. Plots show (a) a histogram of calculated  $E_{\text{ratio}}$  values for each cluster, (b) the integral of (a) with a grey dashed line indicating the values at 95% signal efficiency, and (c) the background rejection of an  $E_{\text{ratio}}$  threshold corresponding to a given signal efficiency.

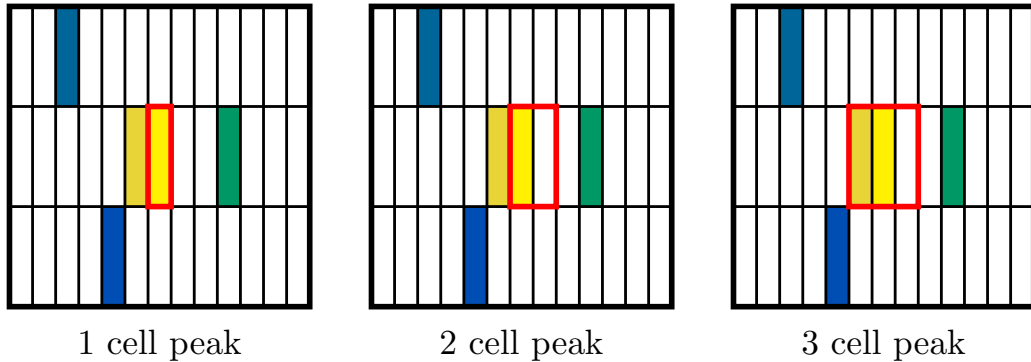


Figure 3.13: Diagram showing which cells contribute to the energy sum for the seed cell (bright yellow) for different peak sizes. The horizontal axis represents  $\eta$  and the vertical axis  $\phi$ . In each case, the calculated energy would be the sum of the energies of the cells contained within the red box.

an odd numbered peak size the energy of a cell is added to that of its neighbours on each side. For an even numbered peak size, neighbours in positive  $\eta$  are preferred. Figure 3.13 shows how cells are included in the calculated energy.

Performance for the  $E_{\text{ratio}}$  algorithm was tested with peak size values from one to five. The results are shown in Figure 3.14. Comparing the benchmark value of background rejection at 95% signal efficiency, it is clear that a peak size of one (i.e. the same as the baseline algorithm) gives the best results, with performance degrading as more cells are added to the energy sum. This appears to be generally true for background rejection at all signal efficiencies. This suggests that the benefit of the fine granularity of each energy measurement outweighs the negative impact of any potential fluctuations that the increased peak size would smear out.

### 3.4.5.3 Exclusion region

Another alteration tested on the  $E_{\text{ratio}}$  algorithm is an ‘exclusion region’ around the seed, i.e. a number of cells close to the seed in which secondary maxima will not be searched for. An  $n$ -cell exclusion region means making the first step along any route  $n$  cells away from the seed in  $\eta$ . Since secondary maxima can be found as

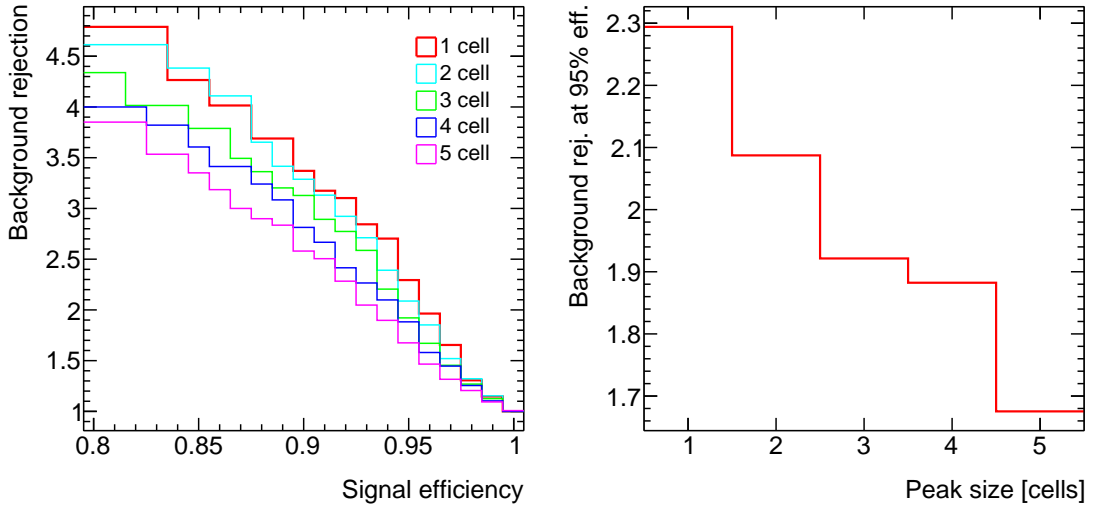


Figure 3.14: Results for calculating  $E_{\text{ratio}}$  with different peak size options. Plots show background rejection as a function of signal efficiency for each peak size tested (left) and background rejection at 95% signal efficiency as a function of peak size (right).

soon as two steps have been taken from the seed cell (they cannot be found on the first step as it will always be a step down from the seed), this excludes all cells in an  $\eta$  range from  $-n$  to  $n$  (in relative coordinates) from being considered secondary maxima. Comparatively, the baseline algorithm with no exclusion region can find secondary maxima anywhere but the four cells directly adjacent to the seed. Figure 3.15 highlights the effect of the exclusion region.

Performance for the  $E_{\text{ratio}}$  algorithm was tested with exclusion regions from between one and five cells, shown in Figure 3.16 alongside the baseline algorithm with no exclusion region. This time a clear increase in performance is visible compared to the initial form of the algorithm, with a one-cell exclusion region attaining a background rejection of 3.1 at 95% signal efficiency. For most signal efficiencies the one-cell exclusion still seems to perform best, though perhaps competing with a two-cell exclusion region for very high signal efficiencies. Since the only difference between no exclusion region and the one-cell case is that cells diagonally adjacent to the seed are excluded, these results suggest signal clusters frequently create secondary peaks on these diagonal; this could stem from incident particles falling close to the corner of a cell.

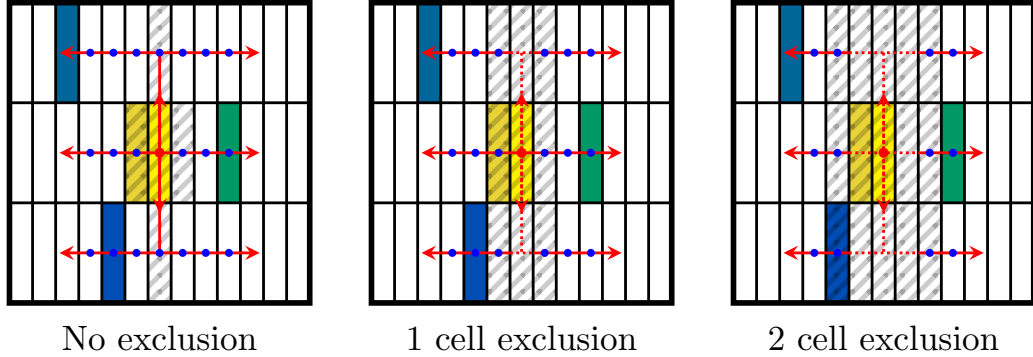


Figure 3.15: Diagram showing how the introduction of an exclusion region to the  $E_{\text{ratio}}$  algorithm prevents secondary maxima close to the seed from being selected. Red arrows mark each of the six paths traversed by the stepwise algorithm. Blue dots mark each step where the energy gradient is calculated. The shaded grey area shows cells that cannot be selected as a candidate secondary maximum, due to either being skipped over or being the first step from the seed.

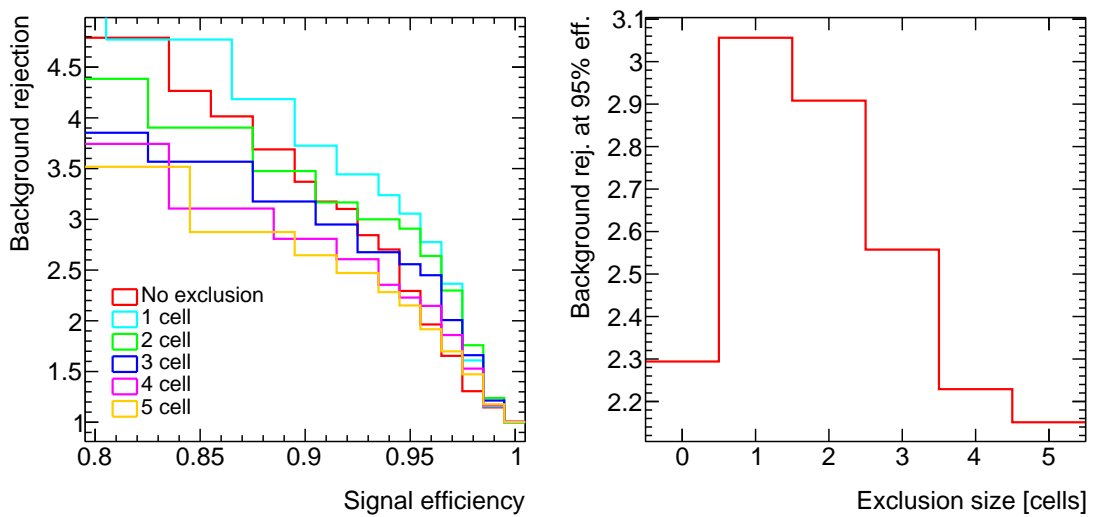


Figure 3.16: Results for calculating  $E_{\text{ratio}}$  with different or no exclusion region definitions. Plots show background rejection as a function of signal efficiency for each tested exclusion region (left) and background rejection at 95% signal efficiency as a function of exclusion region size (right).

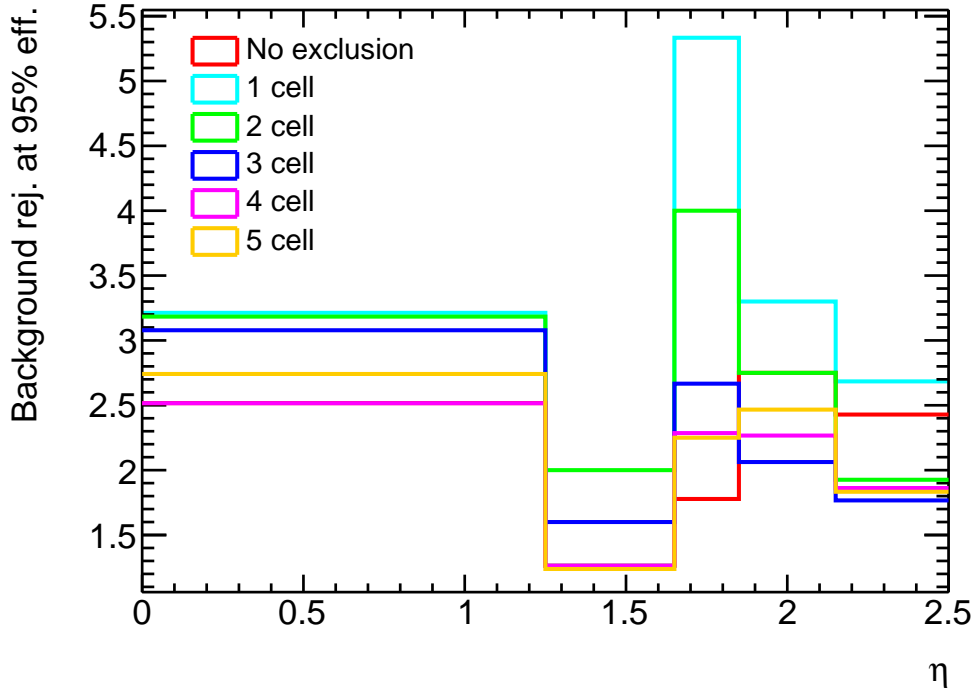


Figure 3.17: Plot of background rejection at 95% signal efficiency as a function of pseudorapidity,  $\eta$ , for  $E_{\text{ratio}}$  algorithms with different exclusion regions.

Given that cell widths vary significantly in different regions of the calorimeter, the performance for the  $E_{\text{ratio}}$  algorithm with different exclusion widths was also tested as a function of  $\eta$ . Figure 3.17 compares background rejection at 95% signal efficiency in several  $\eta$  regions. It is evident that the one-cell exclusion region performs best regardless of calorimeter geometry. The difference between one-cell and two-cell is much more drastic in the high- $\eta$  endcap regions, here the strips are less granular so likely the larger exclusion regions are starting to miss real secondary peaks in background clusters.

#### 3.4.5.4 Search limit

In the baseline  $E_{\text{ratio}}$  algorithm, the stepwise search for secondary maxima extends as far as the available data allows, in this case to the edge of the, conservatively large, stored cluster size. To minimise the amount of processing required by the algorithm, and potentially improve performance by reducing overlap with other clusters, a limit

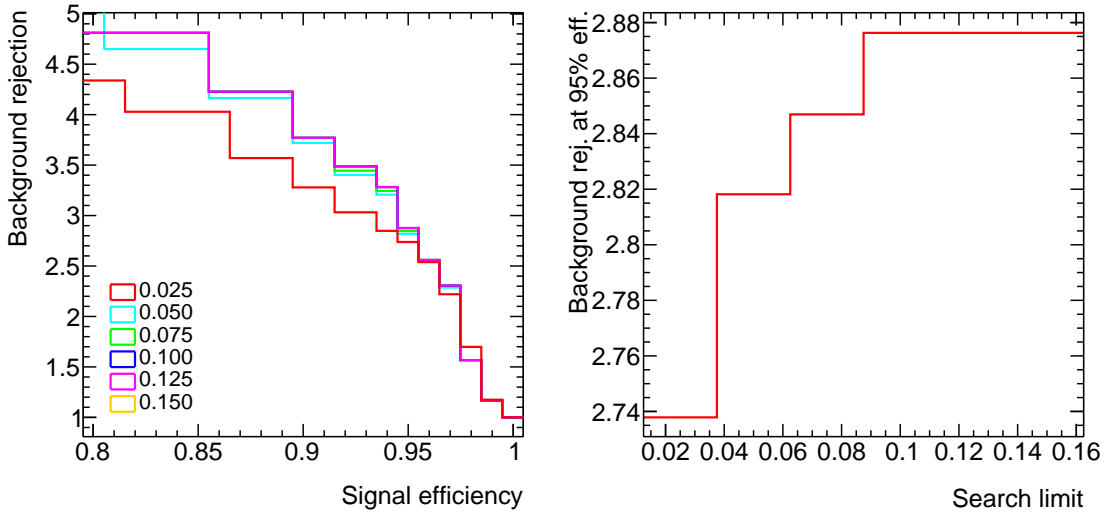


Figure 3.18: Results for calculating  $E_{\text{ratio}}$  after varying the search limit parameter, given as a distance in  $\eta$  from the seed cell. Plots show background rejection as a function of signal efficiency for each tested search limit (left) and background rejection at 95% signal efficiency as a function of the search limit (right).

can be placed on the distance this search will traverse. Since the  $\phi$  range of the search is already limited to one cell either side of the peak, this search limit is implemented as a maximum distance traversed in  $\eta$ . This distance is calculated in pseudorapidity units rather than number of cells to give a consistent response across calorimeter regions.

Performance for the  $E_{\text{ratio}}$  algorithm with different search limit values was tested on simulations, with the results presented in Figure 3.18. Distances in  $\Delta\eta$  from 0.025 up to 0.15 were tested, with 0.15 being the width of the clusters and thus the limit in place in the baseline algorithm. While no performance gains are seen by reducing the search limit, there is a plateau in performance from  $\Delta\eta > 0.1$ . This means the required cluster size, and thus the amount of computation required, can be reduced without degrading performance of the algorithm.

### 3.4.6 Algorithm summary

Given the results presented in Sections 3.4.5.2-3.4.5.4, the most performant and resource-efficient algorithm for calculating  $E_{\text{ratio}}$  in the GEP is the baseline algorithm established in Section 3.4.5.1 with an exclusion region of one cell and a search limit of  $\Delta\eta = 0.1$ . No further improvement was found by varying the peak size. This algorithm achieves a background rejection of 3.1 for 95% signal efficiency.

The  $E_{\text{ratio}}$  algorithm presented here is functionally complete and serves as an option for e/ $\gamma$  discrimination in the GEP, but further improvements could be made with additional study. More parameters could be varied and tested for performance against simulations. One example is a threshold in the energy gradient between steps to allow a change in gradient to be identified, which might improve the response of the algorithm to noise or statistical fluctuations.

# CHAPTER 4

---

## Analysis Methods

---

This chapter presents methods required to perform the analyses presented in the following chapters. Two analyses are discussed, both making use of the  $Z\gamma jj$  final state: VBS of a Z boson and a photon, and semileptonic triboson production of a Z boson, photon, and an additional massive vector boson ( $VZ\gamma$ ). The majority of the methods discussed here are relevant to both analyses, which have many common features.

The primary difference between the analyses is the jet phase space: very high energy forward jets in the Vector-boson Scattering (VBS)  $Z\gamma$  case, and more central jets with a dijet mass peaking around the W/Z boson masses in the  $VZ\gamma$  case. How these differences are addressed as the analyses diverge is discussed in Chapters 5 and 6.

First the data and simulated samples used for the two analyses are discussed in Sections 4.1 and 4.2. The specifics of how detector signatures are reconstructed

Table 4.1: Transverse momentum thresholds for triggers used data in presented analyses. Where two numbers are given, for the dilepton triggers, the first gives the threshold for the leading lepton and the second for the sub-leading.

Signature	Threshold $p_T$ [GeV]	
	2015	2016-18
Single electron	24	26
Single muon	20	26
Dielectron	12, 12	24, 24
Dimuon	18, 8	22, 8

into physics objects are detailed in Section 4.3, and the shared preliminary selection for the analyses is detailed in Section 4.4. Section 4.5 gives some background on machine learning methods used for the  $VZ\gamma$  analysis. Each of the backgrounds, which are common to both analyses, is introduced in Section 4.6. Finally, Section 4.7 covers systematic uncertainties which affect the two measurements, and Section 4.8 discusses the statistical tools used to make inferences from the data.

## 4.1 Data and blinding strategy

The presented analyses use data collected by the ATLAS experiment during Run 2 of the LHC, between 2015 and 2018. Including all data recorded in stable beam conditions with all relevant systems operational, the integrated luminosity for this sample is  $139 \text{ fb}^{-1}$  [38].

The unprescaled single lepton and dilepton triggers [44, 45] were used to select data events, due to the requirement of a leptonically decaying  $Z$  boson in events. Table 4.1 gives the  $p_T$  thresholds required by these triggers for isolated leptons, depending on the lepton flavour and run period. Additional single lepton triggers with higher  $p_T$  thresholds and looser isolation requirements are also included to improve efficiency.

This set of triggers was found to accept 99% of events which would pass the VBS  $Z\gamma$  selection described in Section 5.2. This efficiency is expected to be comparable

for the semileptonic  $VZ\gamma$  selection.

Analyses are performed ‘blind’, meaning that data yields in certain regions are not looked at until the analysis strategy is decided. This is done to avoid data bias, i.e. adapting the analysis procedure based on effects in the data (which could be statistical fluctuations).

In each analysis certain control regions are used, both for estimating backgrounds and validating data-MC agreement. These regions were ‘unblinded’ first in order to validate the methods for which they are used. The signal regions in the two analyses remained blinded until the fits had been finalised, at which point unblinding and running the fit represents the final measurement being taken.

## 4.2 Simulated event samples

The signal and background processes for both analyses are the same, the same simulated event samples can therefore be used for each.

EW  $Z\gamma jj$  production, the signal sample, is generated with `MADGRAPH5_AMC@NLO 2.6.5` [12]. This sample is at Leading Order (LO) accuracy (order  $\alpha_{\text{EW}}^4$ ) with the NNPDF3.1 LO PDF set [11]. Parton showering, hadronisation, and underlying event activity are added through `PYTHIA 8.240` [14]. An alternate version of this sample is produced using `HERWIG++ 2.7.1` [16, 46] in place of `PYTHIA` to evaluate uncertainties due to the choice of parton showering and underlying event model.

The dominant background process is QCD production of  $Z\gamma jj$ . The nominal sample used for this process is produced with `MADGRAPH5_AMC@NLO 2.3.3` [12] using the NNPDF3.0 Next-to-leading Order (NLO) PDF set [47]. Diagrams up to order  $\alpha_s^2 \alpha_{\text{EW}}^2$  are included.

Additional samples for QCD  $Z\gamma jj$  are generated to evaluate uncertainties. A sample made with `SHERPA 2.2.4` [13] at LO accuracy, with up to three additional parton

emissions, is used to assess generator differences. The NNPDF3.0 Next-to-next-to-leading Order (NNLO) PDF set is used for this sample, in conjunction with a dedicated parton shower tuning developed by the SHERPA authors. Five more samples are used for evaluation of theoretical uncertainty. These are generated at particle level using SHERPA 2.2.10 [13] with the NNPDF3.0 NNLO PDF set. One of the five samples has a nominal value for the merging and resummation scales and the other four have an up or down variation for either.

Interference between EW and QCD  $Z\gamma$  production is estimated at LO using MADGRAPH5\_AMC@NLO. 2.3.3 with the NNPDF3.0 LO PDF set, including contributions order  $\alpha_s \alpha_{EW}^3$  to the amplitude.

The  $Z+jets$  background, in which a jet is misidentified as a photon, is estimated with a data-driven method. A MC sample for this process is necessary to evaluate correlation between the regions used in this method, as discussed in Section 5.4. POWHEGBOX v1 [48, 15, 49] is used to generate this sample at NLO accuracy with the CT10 NLO PDF set [50]. PYTHIA 8.210 [14] is used for parton showering in this sample, with the AZNLO [51] set of tuned parameters.

A  $t\bar{t}\gamma$  sample is generated at LO accuracy with MADGRAPH5\_AMC@NLO and the NNPDF2.3 LO PDF set [52]. The  $WZ$  background has both a QCD and EW component produced with SHERPA 2.2.2 [13] at NLO, with NNPDF3.0 NNLO PDF set, and MADGRAPH5\_AMC@NLO 2.6.2 [12] at LO, with NNPDF3.0 LO PDF set, respectively.

Pileup (additional proton-proton interactions) is overlaid on simulated samples, generated with PYTHIA 8.186 using the A3 tune [53] and the NNPDF2.3 LO PDF set. Data is used to reweight these MC events to respect the mean number of interactions per bunch crossing from the corresponding data-taking period.

Once physics events and pileup are combined, samples are passed through a simulation of the ATLAS detector with GEANT4 [19, 18] and then processed with offline reconstruction in the same manner as data events. Additional scale factors and

smearing are applied to more closely match data events.

## 4.3 Object reconstruction

A reconstruction procedure is applied in order to match signals in the detector to the corresponding physics object that created them, and to calculate the kinematic properties of the incident particles. The procedure used is different for any class of physics object. This section discusses the details of the reconstruction for each of the objects used in the two presented analyses: photons, electrons, muons, and jets.

### 4.3.1 Photons

Photon reconstruction covers two scenarios: unconverted photons where the photon passes through the tracker and deposits its energy in the calorimeter, or converted photons where the photon converts into an  $e^+e^-$  pair inside the tracker. The signature for an unconverted photon is an EM cluster with  $E_T > 1.5$  GeV and no associated track (due to the photon being electrically neutral). The signature for a converted photon is two opposite-sign electron candidates with tracks from the same vertex, within the tracking system, consistent with a massless particle. These signatures are considered as photon candidates.

Transverse energies are calculated by combining candidate photon EM clusters with any further clusters within a  $0.075 \times 0.125$  ( $\eta \times \phi$ ) area centred on the candidate cluster. Energy measurements are corrected for scale and resolution effects due to variation in detector response across  $\eta\text{-}\phi$  and data-MC differences [54]. Systematic uncertainties are included in the results to account for uncertainties from these corrections.

Jets can often produce similar signatures to photons, and so additional requirements are placed on the calorimeter shower shape to discriminate against these ‘fake pho-

tons’. The desired prompt photons typically result in more collimated clusters contained within the EM calorimeter, whereas fake photons produce broader showers and leakage into the hadronic calorimeter. An identification selection, consisting of a set of cuts on shower-shape variables, is derived to minimise photon fakes.

Additionally, photons must be considered isolated. Non-prompt photons will typically appear nearby other activity in the detector. Prompt photons can be selected by ensuring that photon candidates are isolated in a region with little activity around them. Two variables are used to define the isolation:  $p_T^{\text{cone},20}$  and  $E_T^{\text{cone},20}$ .  $p_T^{\text{cone},20}$  is the sum of transverse momenta of all  $p_T > 1$  GeV tracks originating from the Primary Vertex (PV), within a cone of  $\Delta R < 0.2$  around the direction of the photon.  $E_T^{\text{cone},20}$  is the sum of EM cluster transverse energies within the same cone, minus the energy of the photon. Cuts are defined on these variables as a function of the photon  $p_T$ :  $p_T^{\text{cone},20} < 0.05 \cdot p_T^\gamma$  (track isolation) and  $E_T^{\text{cone},20} < 0.065 \cdot p_T^\gamma$  (calorimeter isolation).

Systematics uncertainties are included in the measurements to account of the efficiencies of photon identification and isolation [55].

### 4.3.2 Electrons

The basic signature to seed an electron is an EM cluster with  $E_T > 1$  GeV with an associated track that has hits in at least four silicon layers. As with photons, the energy for an electron candidate is calculated by summing the energy of the seed cluster with any additional clusters in a  $0.075 \times 0.125$  ( $\eta \times \phi$ ) area, as well as any clusters matched to the same track as the seed. Energy scale and resolution effects are accounted for in the same manner as for photons, and included in systematic uncertainties.

Electron candidates are also subject to identification and isolation requirements, to minimise the impact of fakes. Identification is based on both EM shower shape in the calorimeter and transition radiation in the TRT. Similarly to the photon,

isolation is determined in both the tracker and calorimeter by requiring the energy or momenta within a cone around the seed is below a threshold. The details of both identification and isolation of electrons are discussed in Reference [56].

### 4.3.3 Muon

Muon candidates are seeded from tracks in either the MS or ID. A seed track in the MS must be matched to a track in the ID, and a seed track in the ID must be matched to at least three hits in the MS. Muon candidates are only considered here within the acceptance of the ID ( $|\eta| < 2.5$ ). Candidates must produce three hits in at least two MS stations, or in only one station for muons with  $|\eta| < 0.1$ . The transverse momentum of the muon is calculated from a combined track fit of the tracks/hits in the ID and MS and the corresponding energy loss in the calorimeters.

Muons must also be isolated to select prompt muons from, e.g., boson decays rather than those from hadronic sources. Muon isolation is given by the total  $p_T$  in a cone around the muon divided by the muon  $p_T$ . As with electrons and photons, this is calculated in both the ID and the calorimeter.

Data-MC comparisons are used to measure the efficiency and resolution of muon reconstruction, accounted for in systematic uncertainties [57].

### 4.3.4 Jets

A jet is a physics object representing a localised grouping of hadrons, rather than a single particle. These hadronic showers can be initiated by quarks or gluons radiated from the hard scatter in the collision, since these free partons will hadronise before interacting with any elements of the detector. Jets are thus used as a reconstruction-level analogue of a quark or gluon produced in a physics process.

Reconstructing a jet requires use of a jet clustering algorithm in order to combine

clusters and tracks in the detector to collect all the particles likely to have been produced by the incident hadron. Jet reconstruction in ATLAS uses the anti- $k_t$  jet clustering algorithm [58], with a distance parameter of  $R = 0.4$ .

A jet can be reproduced differently depending on the information given as input to the clustering algorithm. A ‘jet collection’ is the name used for jets produced from a certain set of inputs. The baseline jet collection used in the two presented analyses is ‘particle-flow’ jets, in the VBS analysis ‘topo-cluster’ jets are also considered.

Topo-cluster jets are formed using only calorimeter information, passing topo clusters as input to the clustering algorithm. Topo clusters, or topological clusters, are a pileup-resistant formulation of a calorimeter cluster: with cells added to a cluster based on whether the measured energy exceeds a threshold determined by the expected noise in that cell. Since only calorimeter information is used to create the jets, topo-cluster jets rely heavily on the resolution of the calorimeter [59].

Particle-flow jets are an alternative jet collection created by using ‘particle-flow objects’ as input to the clustering algorithm. A particle-flow object is a combination of calorimeter topo clusters and ID tracks, with calorimeter deposits produced by charged particles removed to avoid energy/momentum double-counting, designed to represent a single particle. Combining calorimeter and tracker information allows for improved resolution at lower energies compared to topo-cluster jets [60].

Systematic uncertainties are included to account for effects on the energy and resolution of jets from detector calibration, properties of the jet such as quark/gluon flavour composition, and data-MC differences [61].

## 4.4 Event selection

Events from data and simulation undergo a selection process to focus on a phase space that matches the desired final state. Data events are required to pass a trigger in order to be recorded, and therefore the same requirement is placed on simulated

Z $\gamma$ selection	
Photon	$N_\gamma \geq 1$ $ \eta_\gamma  < 2.37$ (excludes $1.37 <  \eta_\gamma  < 1.52$ ) $p_T^\gamma > 25$ GeV
Lepton	$N_l = 2$ (OSSF) $ \eta_e  < 2.47$ (excludes $1.37 <  \eta_e  < 1.52$ ) $ \eta_\mu  < 2.5$ $p_T^{l,1} > 30$ GeV $p_T^{l,2} > 20$ GeV
Boson	$m_{ll} > 40$ GeV $m_{ll} + m_{ll\gamma} > 182$ GeV

Table 4.2: Cuts implemented for both analyses to select Z $\gamma$  events. Here  $p_T^{l,1}$  denotes the  $p_T$  of the leading (i.e. highest  $p_T$ ) lepton, and  $p_T^{l,2}$  denotes that of the sub-leading (second highest  $p_T$ ) lepton. OSSF indicates that two opposite-sign same-flavour leptons are required.

events for parity. For both analyses, any events passing either the single lepton or dilepton trigger thresholds are considered.

For an event to be selected, first the basic objects in the desired final state need to be present. There must be at least one photon passing isolation and identification requirements. There must be precisely two electrons or muons present, of the same flavour to each other but opposite charge, with both passing isolation and identification. At least two jets must have been reconstructed in the event, as per Section 4.3.4.

Further selection is applied to the lepton-photon system in order to identify events with a real Z boson and a photon not produced from Final-state Radiation (FSR). This Z $\gamma$  selection is detailed in Table 4.2, and acts as a pre-selection for both analyses before additional jet selection is applied.

The cut on the sum of the dilepton mass and the dilepton-photon mass,  $m_{ll} + m_{ll\gamma}$

is imposed to reject events with photons from FSR. In an FSR event, the photon is radiated from one of the final state leptons. This means the two leptons and the photon all originate from the same Z boson, and their invariant mass should be close to the mass of the Z boson. The invariant mass of the dilepton system in this case would be less, and so the sum of these masses should be less than twice the Z mass. In a non-FSR event, the photon is radiated before or simultaneous to the Z boson production, giving a dilepton mass close to the Z mass and a larger dilepton-photon invariant mass. The sum of the masses in this instance is typically greater than twice the Z mass. Figure 4.1 shows a two-dimensional distribution of these two invariant masses and how this cut rejects the population of events with FSR photons.

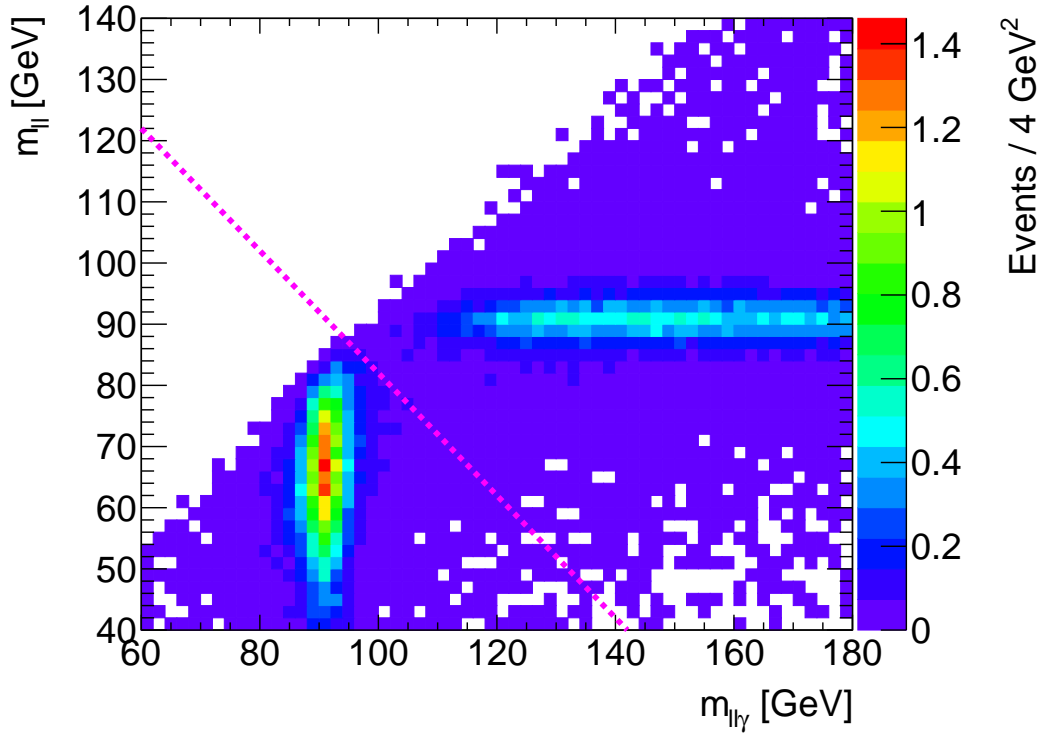


Figure 4.1: Distribution of events as a function of  $m_{ll}$  and  $m_{ll\gamma}$ , for events in the signal sample passing the lepton and photon cuts given in Table 4.2. The dashed line shows the threshold for the FSR-rejection cut, events below the dashed line are discarded.

FSR events are rejected as the photon emission from a final state lepton excludes the possibility of the photon having been produced in a multiboson interaction, which

are the focus of these analyses.

## 4.5 Boosted decision trees

## 4.6 Background estimation

The two presented analyses share a common set of background processes. Due to the differing phase space, estimation of the QCD  $Z\gamma$  background is different for each analysis. The remaining backgrounds however follow the same estimation procedure for both analyses. This section discusses the procedure for the common backgrounds:  $Z+jets$ ,  $t\bar{t}\gamma$ , and  $WZjj$ .

### 4.6.1 Fake photon estimation

Background from  $Z+jets$  events overlaps the analysis final state when a jet is misidentified as a photon. Fake photons such as these are not well modelled in MC, and so the shape and normalisation of this background must be calculated with a data-driven method.

#### 4.6.1.1 Normalisation

The ABCD method is used to estimate the normalisation for this process. This is done by establishing three orthogonal control regions adjacent to the region of interest (e.g. the SR). Cuts in two different variables, here the photon identification and isolation, are used to define these regions, as demonstrated by Figure 4.2. The region of interest is labelled as region A, inverting the photon calorimeter isolation gives region B, inverting identification gives region C, and inverting both criteria gives region D. Track isolation is still required for the photon in all regions.

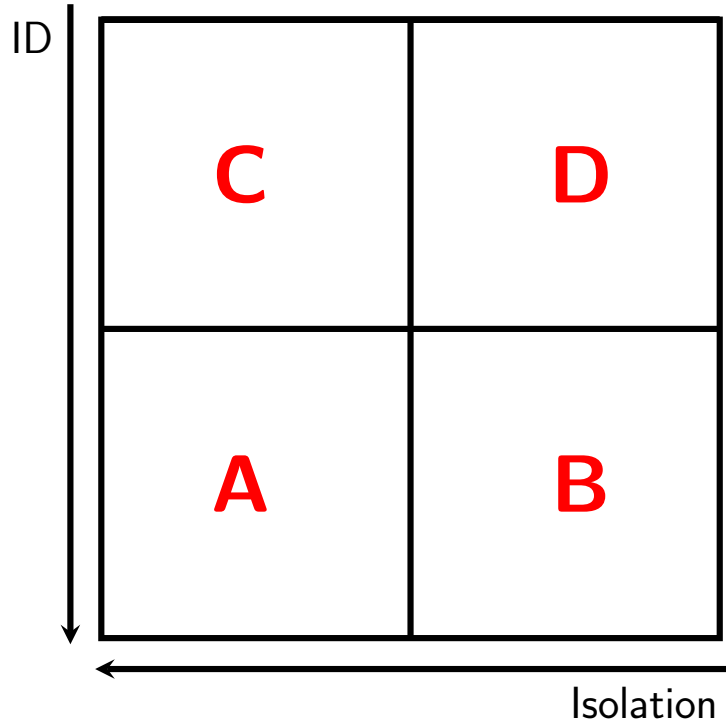


Figure 4.2: Schematic of the four regions used for fake photon background estimation. Region A represents the signal region; B, C, and D represent control regions obtained by relaxing isolation and/or identification requirements.

These three control regions are used to infer the amount of Z+jets background in the region of interest with the relationship

$$N_A^{\text{Z+jets}} = R \frac{N_{B,\text{data}}^{\text{Z+jets}} \times N_{C,\text{data}}^{\text{Z+jets}}}{N_{D,\text{data}}^{\text{Z+jets}}}$$

where  $N_{X,\text{data}}^{\text{Z+jets}}$  is the number of Z+jets events in the given region calculated by subtracting background and signal leakage from the data yield i.e.

$$N_{X,\text{data}}^{\text{Z+jets}} = N_X^{\text{data}} - N_X^{\text{bg}} - c_X N_{A,\text{data}}^{\text{sig}}, \quad \text{for } X = B, C, D.$$

The correlation factor,  $R$ , is given by

$$R = \frac{N_{A,\text{MC}}^{\text{Z+jets}} \times N_{D,\text{MC}}^{\text{Z+jets}}}{N_{B,\text{MC}}^{\text{Z+jets}} \times N_{C,\text{MC}}^{\text{Z+jets}}}$$

where in this case each  $N_{X,\text{MC}}^{\text{Z+jets}}$  is the event yield observed in Z+jets MC in this region. Also defined are signal leakage parameters,  $c_X$ , as

$$c_X = \frac{N_{X,\text{MC}}^{\text{sig}}}{N_{A,\text{MC}}^{\text{sig}}}, \quad \text{for } X = B, C, D,$$

calculated from QCD and EW Z $\gamma$  MC. Signal leakage represents any prompt photon events entering the CRs, hence both EW and QCD Z $\gamma$  production are considered as signal in this instance.

#### 4.6.1.2 Shape

The shape of the Z+jets background is taken directly from a data control region. The control region should be very pure in Z+jets events, but also sufficiently high statistics. The chosen region is the anti-tight region, with no requirement on track or calorimeter isolation. This is equivalent to regions C and D combined but without the track isolation requirement.

#### 4.6.1.3 Uncertainties

Several components of the normalisation for this background estimate have associated uncertainties. These are propagated to the final normalisation and included as a systematic uncertainty on results.

The MC background subtraction is subject to the uncertainty on the subtracted backgrounds. As this is predominantly from t $\bar{t}\gamma$ , a 15% uncertainty is used on the total subtracted background.

The signal leakage fractions,  $c_X$ , are split into two components, EW and QCD, representing the leakage from each source of prompt photons. To get uncertainty on the QCD leakage fraction it is first calculated with both the nominal and alternate sample. The difference between the calculated leakage fractions is combined with the

MC statistical uncertainty on the nominal sample to get the total QCD uncertainty. The EW leakage fraction is a minor contribution to the total leakage fraction, and so the uncertainty is taken as 50%, combined with the MC statistical uncertainty.

The correlation factor,  $R$ , has an uncertainty calculated from data-MC comparisons in complementary regions where the photon fails track isolation requirements. The correlation factor is re-calculated for both data and MC with the track isolation requirement inverted. The difference between these two  $R$  values is combined with the MC statistical uncertainty on the nominal  $R$  value to give its uncertainty.

#### 4.6.2 Monte Carlo backgrounds

The background from  $t\bar{t}\gamma$  events is estimated from MC and cross-checked in an  $e\mu\gamma$  CR, which validates the use of a  $k$ -factor of 1.44 to scale the MC normalisation.  $WZjj$  events make a minor contribution to the background, this is estimated solely from MC.

### 4.7 Systematic uncertainties

Many sources of uncertainty are considered for processes estimated in the presented analyses. The subsections below cover uncertainties from theoretical and experimental sources which are considered for EW and QCD  $Z\gamma jj$  production processes. Smaller backgrounds from MC estimates use a simple overall uncertainty on the normalisation: 15% for  $t\bar{t}\gamma$  and 20% for  $WZjj$ . The  $Z+jets$  background has a normalisation uncertainty calculated per-analysis considering the contributions detailed in Section 4.6.1.3. Limited statistics in MC samples also contributes uncertainties to all processes.

All systematic uncertainties are included as nuisance parameters in the fit used for each analysis, and the final impact of each uncertainty is adjusted according to the

data.

### 4.7.1 Theoretical uncertainties

Theoretical uncertainties are calculated for EW and QCD  $Z\gamma$  production mechanisms. These come from a variety of sources: choice of PDF set, renormalisation and factorisation scales, QCD modelling, choice of parton showering and underlying event model, and EW-QCD interference.

Evaluating uncertainty in PDF set choice is done by reweighting events using a number of replica PDF sets. Taking the standard deviation of yields under each of these weights gives the PDF uncertainty on the event yield.

Uncertainty due to scale choice is calculated by varying the default values of renormalisation and factorisation scales in the nominal QCD  $Z\gamma$  MC sample. Dedicated samples (as discussed in Section 4.2) are used to evaluate the effect of varying these two values. The per-bin envelope of all deviations is taken as the scale uncertainty.

QCD modelling uncertainty can be calculated conservatively by comparing predictions from different generators or, more precisely, by evaluating the effect of merging and resummation scales. Generator differences are calculated by taking the difference in event yields predicted by the nominal and alternate QCD  $Z\gamma$  samples. This difference is considered as the QCD modelling uncertainty on the nominal yield. Alternately, uncertainty from choice of merging (CKKW) and resummation (QSF) scale is calculated using the dedicated samples described in Section 4.2. The latter method is used for the VBS analysis whilst the former is used for the triboson analysis.

For the EW signal, parton showering and underlying event uncertainties are calculated by comparing the default PYTHIA hadronisation to alternatives with HERWIG or with a varied PYTHIA tune.

The interference between EW and QCD  $Z\gamma$  production is not included in either

the signal or background, but instead taken as an additional uncertainty, calculated using the dedicated interference sample.

### 4.7.2 Experimental uncertainties

Experimental systematic uncertainties cover uncertainties in energy scale and resolution of jets, photons, and electrons; momentum scale and resolution of muons; scale factors used to reproduce trigger, reconstruction, identification, and isolation efficiencies from data; suppression of pile-up jets; and flavour tagging. These uncertainties have a varying level of effect on the presented results, some of the most impactful uncertainties are discussed here.

#### 4.7.2.1 Pileup reweighting

MC samples are typically generated before data-taking is complete. The pileup distribution, i.e. the distribution of instantaneous luminosities, is therefore only estimated and does not exactly match that in data. Events are reweighted to align the pileup distributions between MC and data. The scale factors used to achieve this reweighting are calculated with a corresponding uncertainty. This uncertainty is propagated to physics results as a systematic uncertainty.

#### 4.7.2.2 Jet flavour composition and response

Jets initiated by quarks and gluons exhibit differences in fragmentation and showering properties. These properties will impact the jet energy scale calibration and so the distribution of quark- and gluon-initiated jets and its uncertainty affects the overall jet energy scale uncertainty. Whether a jet is quark- or gluon-initiated is referred to as the flavour of the jet.

The response of the calorimeter to different flavours of jet is not well modelled in MC,

and so is corrected using comparisons with data. Uncertainties on this correction are propagated as a ‘jet flavour response’ systematic uncertainty.

The jet response is itself dependent on the flavour composition of jets in the MC sample. This composition is dependent on the selection, so any jet selection differing from those in the jet calibration schemes will not have a well defined flavour composition. Uncertainties on the jet flavour composition within the phase space are taken as a systematic uncertainty on analyses [62].

Both jet flavour response and jet flavour composition uncertainties can be reduced by studying the fraction of quark and gluon jets in the phase space. This additional step is taken in the VBS analysis to manage these uncertainties.

## 4.8 Statistical inference

# CHAPTER 5

---

## Search for vector-boson scattering production of a Z boson and a photon

---

### 5.1 Introduction

Vector-boson scattering provides a unique experimental signature, producing decay channels with excellent potential to probe rare SM processes; the high selection efficiency achievable by exploiting kinematics of the VBS tag jets allows measurements to be conducted at lower cross-sections than would otherwise be accessible in the current dataset. VBS  $Z\gamma$  serves as a production mechanism for the  $Z\gamma jj$  final state, with the Z boson and photon resulting from a direct multiboson interaction and the jets created as a feature of the VBS production. This provides a robust framework for studying these rare SM interactions, motivated previously in Chapter X. Feynman diagrams for VBS  $Z\gamma$  production are represented in Figure 5.1, showing that QGC or TGC vertices are the only SM contributions at tree-level.

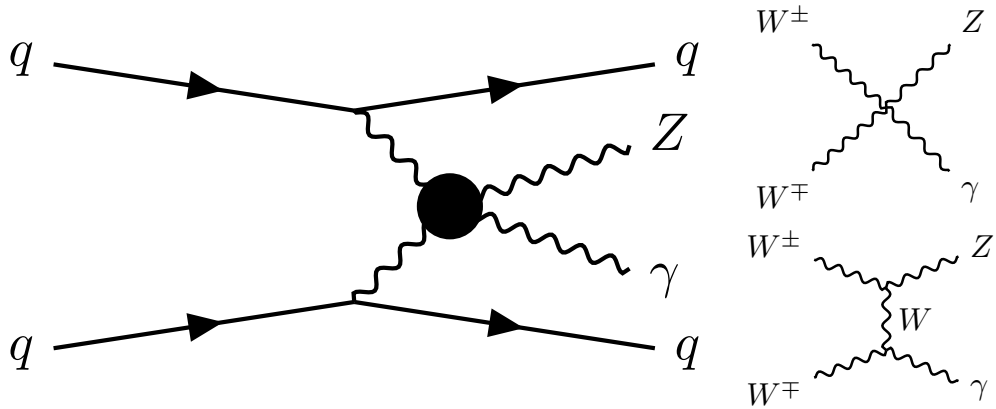


Figure 5.1: Feynman diagram for a  $Z\gamma$  vector-boson scattering event (left). The black circle contains the multiboson interaction, which for a tree-level SM interaction will be one of the two shown (right).

In the archetypal VBS event, a quark from each of the two colliding protons radiates a boson. The two bosons interact to produce the EW component of the final state and the quarks, deflected from their original trajectories after boson emission, appear as jets in the detector. Since the initial quarks are usually very energetic, the angle through which the quarks are deflected in the interaction is typically small. The final-state jets, known as tag jets, would therefore be in the very forward regions of the detector, at opposite ends to one another, and also still carrying large amounts of energy. These kinematics are typically characterised by a large invariant mass of the dijet system ( $m_{jj}$ ) and a large difference between the rapidities of the jets ( $\Delta y(j, j)$ ).

VBS  $Z\gamma$  production is one component of the more general EW production of  $Z\gamma jj$ . The VBS production modes are not gauge-invariantly separable from others, so a direct measurement of VBS  $Z\gamma$  is not strictly possible. Instead, EW  $Z\gamma jj$  production is measured with a selection designed to enhance the VBS component, matching the kinematics of the jets with the expected VBS signature. Figure 5.2 gives Feynman diagrams for some non-VBS production modes that contribute to the EW production mechanism.

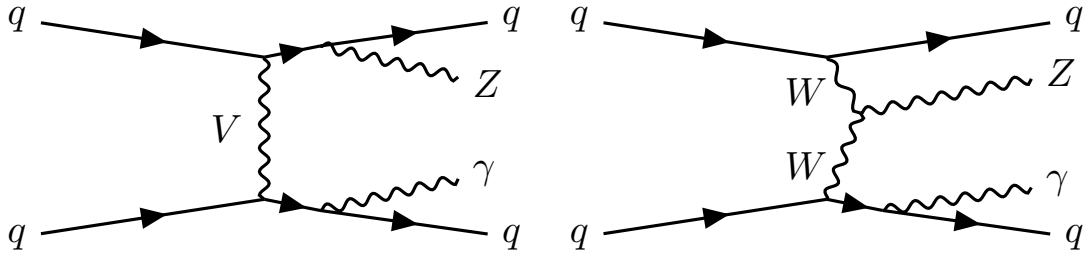


Figure 5.2: Example Feynman diagrams for non-VBS EW production of  $Z\gamma jj$ . In these instances one or none of the two final-state bosons are produced through multiboson interactions.

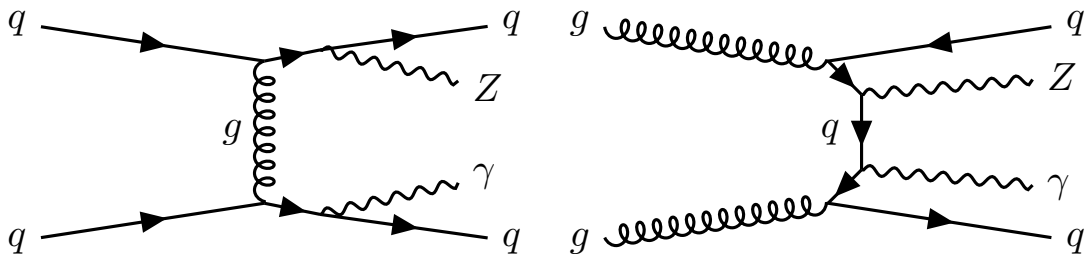


Figure 5.3: Example Feynman diagrams for QCD production of  $Z\gamma jj$ .

To measure this EW  $Z\gamma jj$  production, background processes with the same final state must be understood. The dominant background for this analysis comes from QCD  $Z\gamma jj$  production. Figure 5.3 gives example Feynman diagrams for this QCD production, which differs from the EW mode as the strong force either provides the interaction between the two quarks or otherwise generates the final-state jets, resulting in colour-connected jets. Additional interactions between the colour-connected jets are very probable and will affect the observed jet kinematics, allowing these events to be distinguished from VBS events.

The goal of this analysis is to measure the fiducial cross-section of EW  $Z\gamma jj$  production in a region sensitive to VBS  $Z\gamma$  production. Ideally, if enough precision is obtained, this will constitute the first observation of this process by the ATLAS experiment. The measurement relies on a cut-based selection, exploiting the VBS event kinematics. Signal and background processes are estimated, through a combination of MC simulation and data-driven estimates, and used to make a template fit to the dijet mass distribution. This chapter presents the analysis as a whole,

with additional focus given to sections on jet collection investigations, controlling jet flavour systematics, and pruning of systematic uncertainties.

## 5.2 Event selection

Selection is applied to simulation, using the samples detailed in Section 4.2, and data to reach the desired VBS-enhanced phase space. Cuts are first made to the  $Z\gamma$  system following the prescription given in Section 4.4.

Imposing VBS-like kinematics on the jets further reduces the phase space. Jets are required to have a transverse momenta of at least 50 GeV, and a rapidity of less than 4.4 in magnitude. There must be at least two jets, and no b-tagged jets in the event. The dijet system, formed from the two highest momentum jets, should have a mass  $m_{jj} > 150$  GeV and an inter-jet separation of  $|\Delta y_{jj}| > 1.0$ . A veto on ‘gap jets’, jets (reconstructed with  $p_T > 25$  GeV) found in the rapidity region between the two VBS tag jets, is applied to exploit the difference between VBS jets and colour-connected QCD jets. A loose cut is placed on the centrality of the  $ll\gamma$  system relative to the jets,  $\zeta(ll\gamma) < 5$ , where centrality is given by

$$\zeta(ll\gamma) = \left| \frac{y_{ll\gamma} - (y_{j_1} + y_{j_2})/2}{y_{j_1} - y_{j_2}} \right|, \quad (5.1)$$

where  $y_{ll\gamma}$  is the rapidity of the  $ll\gamma$  system and  $y_{j_i}$  is the rapidity of the  $i^{\text{th}}$  highest energy jet.

These cuts define the analysis region, and are summarised in Table 5.1. This is further split into the SR and the QCD CR with tighter requirements on the  $ll\gamma$  centrality:  $\zeta(ll\gamma) < 0.4$  defines the SR and  $\zeta(ll\gamma) > 0.4$  gives the CR used for the QCD  $Z\gamma$  background estimate.

Table 5.1: Summary of event selection criteria defining the VBS analysis region. This region is further subdivided by additional criteria on  $\zeta(ll\gamma)$ .

VBS $Z\gamma$ selection	
$Z\gamma$ system	$Z\gamma$ selection (Table 4.2)
Jet	$N_j \geq 2$ $ y_j  < 4.4$ $p_T^j > 50$ GeV $N_j^{\text{b-tag}} = 0$ $N_j^{\text{gap}} = 0$
Dijet system	$m_{jj} > 150$ GeV $ \Delta y_{jj}  > 1$
Event	$\zeta(ll\gamma) < 5$

### 5.3 Particle-flow jet validation

The choice of jet collection for this analysis is non-trivial. Particle-flow jets have recently become the standard recommendation within ATLAS in place of topocluster jets, but rather than applying that recommendation unilaterally, the specific case for this analysis is considered. For a discussion of jet collections, see Section 4.3.4.

The benefits of particle-flow include improved resolution for low-energy jets, although this only works within the acceptance of the ID. Typical VBS jets are energetic and very forward, perhaps pushing into regions beyond ID acceptance. Although a great deal of VBS jets will still be in range to benefit from particle-flow, the phase space is very different from one which would make particle-flow jets an obvious choice. This section presents a comparison between particle-flow and topocluster jets in the analysis phase space to justify the move to using particle-flow jets.

The procedure for comparing performance between these two jet collections is to investigate the difference in event yield from applying jet-based selection criteria with values calculated from either jet collection. The  $Z\gamma$  selection, as in Table 4.2,

Table 5.2: Yields and efficiencies after each jet cut, compared for both topo-cluster and particle-flow jets. Starting from all EW  $Z(\rightarrow ee)\gamma jj$  events that pass the  $Z\gamma$  selection. Efficiencies given are for the individual cut, relative to the yield from the previous cut. The difference is given as percentage increase from the topo-cluster to the particle-flow yields. The third cut is overlap removal between jets and leptons or photons.

Cut	Topo-cluster		Particle-flow		Difference
	Yield	Eff.	Yield	Eff.	
$N_j \geq 2$	51084	79.7%	51468	80.3%	+0.7%
$p_T^j > 50 \text{ GeV},  \eta_j  < 4.5$	31362	61.4%	31604	61.4%	+0.8%
$\Delta R(l, j), \Delta R(\gamma, j) > 0.4$	31359	99.99%	31552	99.84%	+0.6%
$ \Delta\eta_{jj}  > 1.0$	27127	86.5%	27293	86.5%	+0.6%
$ m_{jj}  > 150 \text{ GeV}$	26752	98.6%	26885	98.5%	+0.5%

is applied first then jet-based cuts are applied and the resulting yields compared. For simplicity, this was investigated in the signal MC sample for only  $Z \rightarrow ee$  events.

Looking at the overall yield of events after each cut shows that the two jet collections give very similar results, always within 1% of one another. Table 5.2 shows these yields.

Differences can be further scrutinised by looking at each individual event; most events should result in the same decision, pass or fail, regardless of the jet collection chosen. This checks that the similar yields aren't merely a coincidence, when in fact many events pass only one selection. Figure 5.4 shows these per-event differences in decisions.

For the vast majority of events, the two jet collections make the same selection, with less than 5% of events showing differences. These differences are tested by investigating the distributions in the cut variables for cases where the two jet collections give a different result. For example, if an event passes  $m_{jj} > 150 \text{ GeV}$  with topo-cluster jets but not with particle-flow jets then the particle-flow  $m_{jj}$  value should be close to the cut boundary of 150 GeV.

Investigating the case where events are selected using particle-flow jets but not

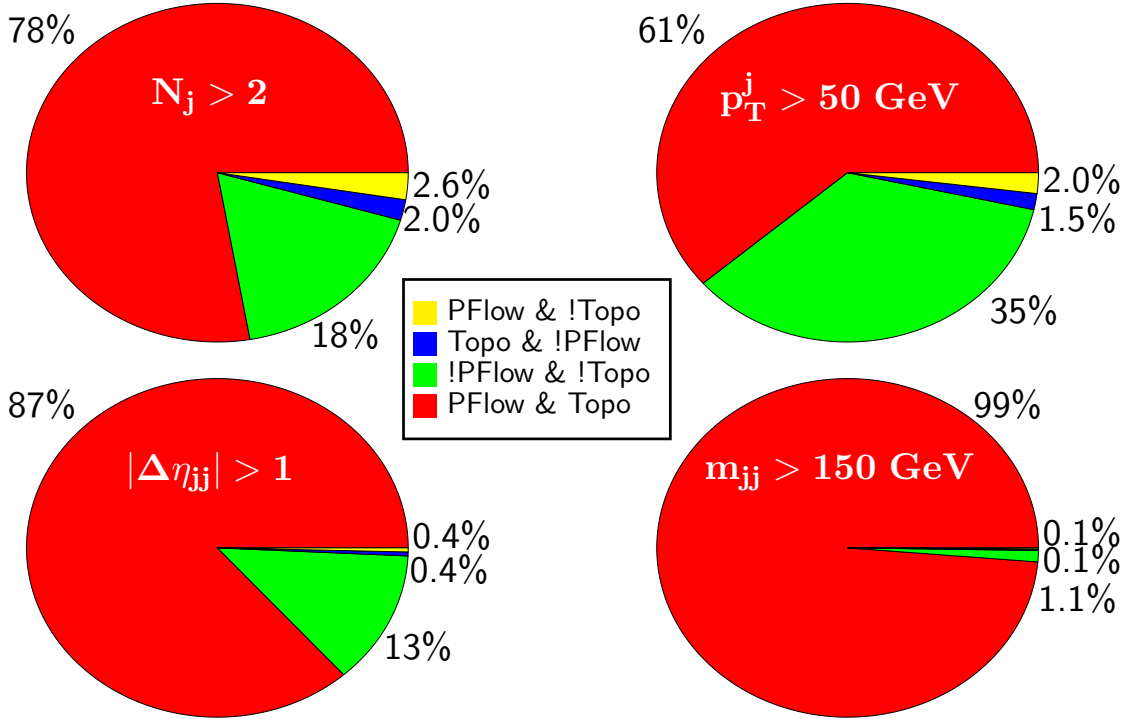


Figure 5.4: Impact of four of the key jet cuts on the analysis yield when applied individually with particle-flow and topo-cluster jets. Events are divided into four categories based on whether or not they pass the particle-flow cut and whether or not they pass the topo-cluster cut. Cuts are applied in the same order as presented in Table 5.2. Only events that pass the previous cut for both particle-flow and topo-cluster jets are included in the results, to decorrelate the effects of each individual cut. The label ‘PFlow’ is used for particle-flow cuts and ‘Topo’ for topo-cluster cuts.

topo-cluster jets, results for the four key cut variables are shown in Figure 5.5. The distributions are, largely, as expected given that values peak on the cut boundary and tail off for more extreme differences. However, it is notable that for the dijet variables,  $m_{jj}$  and  $|\Delta\eta_{jj}|$ , there are some strong outliers.

Events falling very far from the cut boundary for particle-flow jets when the topo-cluster jet variable fails the cut seem to indicate a significant disagreement in kinematics between the two jet collections. It is possible that these outliers happen when the  $p_T$  ordering of jets varies between collections. Dijet variables are calculated using the two highest energy jets, so a small shift in  $p_T$  between the second and third jets could cause dijet variables to be calculated with a different jet pair and therefore give very different results.

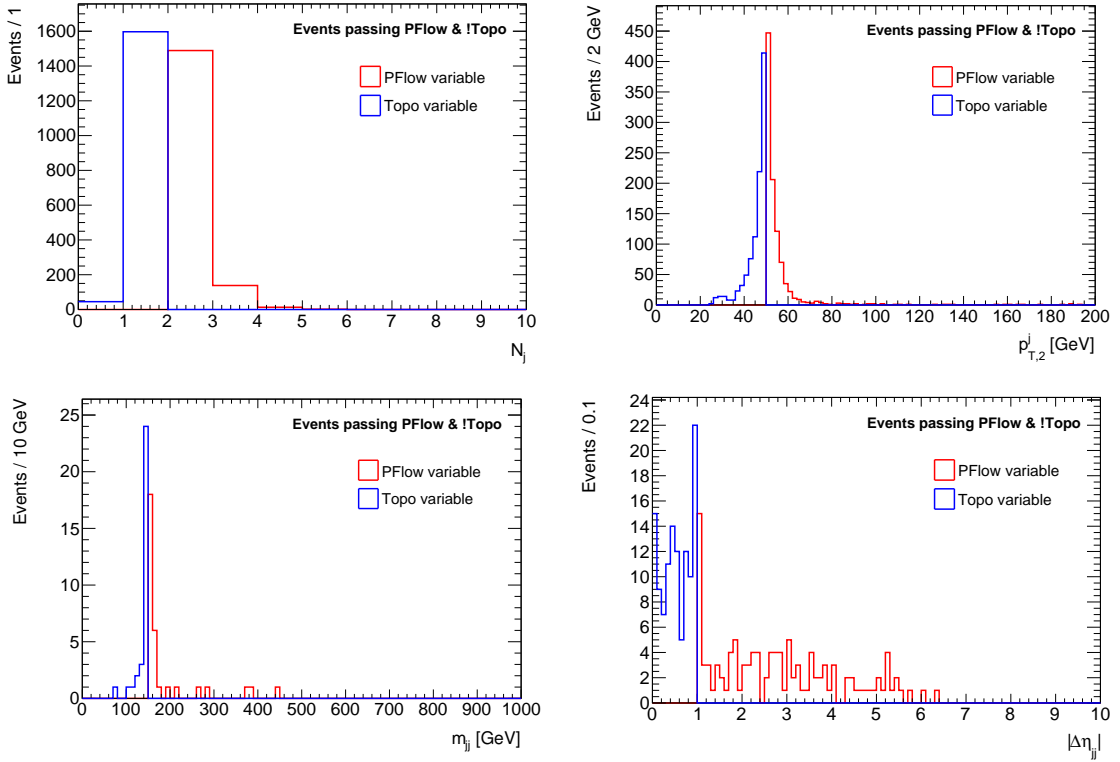


Figure 5.5: Distribution of events passing jet requirements for the particle-flow collection but not the topo-cluster collection. In each case the cut is in the same distribution as the histogram plotted. Four cuts are shown:  $N_j > 2$  (top left),  $p_T^{j,2}$  ( $p_T$  of second most energetic jet)  $> 50$  GeV (top right),  $m_{jj} > 150$  GeV (bottom left),  $|\Delta\eta_{jj}| > 1$  (bottom right). Only events passing all prior cuts for both particle-flow and topo-cluster jets are included. The label ‘PFlow’ is used for variables calculated with particle-flow jets and ‘Topo’ for topo-cluster jets.

This hypothesis can be tested by looking at the separation between jets used in each event for the two collections. The variable used to measure this is

$$\min \Sigma(\Delta R) = \min_{k_i \in \{(1,2),(2,1)\}} \sum_{i=1}^2 \Delta R(j_i^{\text{topo-cluster}}, j_{k_i}^{\text{particle-flow}}), \quad (5.2)$$

i.e. the sum of the two  $\Delta R$  values between topo-cluster and particle-flow jets, for whichever pairing of the jets gives the lowest value of the sum.  $\Delta R$  is the sum in quadrature of  $\Delta\eta$  and  $\Delta\phi$ . Figure 5.6 shows the distribution of this variable for events passing  $m_{jj}$  for only particle-flow jets. There are two clear populations, separated at  $\min \Sigma(\Delta R) \sim 0.5$ . The lower  $\min \Sigma(\Delta R)$  population should contain events where the particle-flow and topo-cluster jets are representing the same phys-

ical objects. Requiring  $\min\Sigma(\Delta R) < 0.5$  on top of the existing selection gives the  $m_{jj}$  distribution shown in Figure 5.6, where now all remaining events are tightly distributed around the cut boundary.

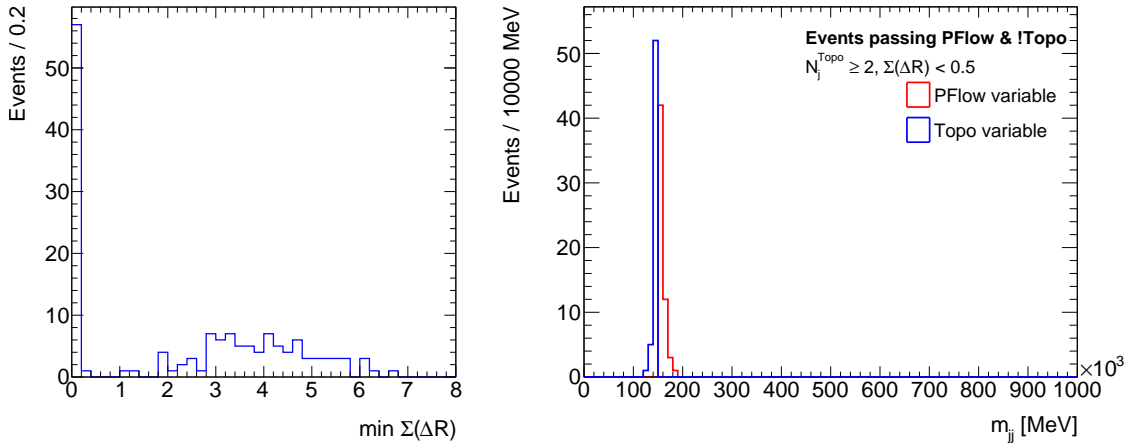


Figure 5.6: Distribution of the  $\min \Sigma(\Delta R)$  variable, defined in Equation 5.2, for events passing  $m_{jj} > 150$  GeV for particle-flow but not topo-cluster jets (left); and the  $m_{jj}$  distribution for these events after requiring  $\min \Sigma(\Delta R) < 0.5$  (right). The label ‘PFlow’ is used for variables calculated with particle-flow jets and ‘Topo’ for topo-cluster jets.

This study, although limited in scope, serves to demonstrate that the key jet variables used in this analysis perform very similarly when calculated with particle-flow and topo-cluster jets. Any differences seen are sufficiently small that no meaningful effect on the analysis result is expected. This is considered as motivation to use particle-flow jets for this analysis in keeping with the updated ATLAS recommendation. To really understand if the improvements in resolution with particle-flow jets are seen in the analysis phase space, further studies could be conducted on how systematic uncertainties differ between collections, to determine which would give the most precise result. This would have been a possible extension given more time.

## 5.4 Background estimation

The dominant background for this analysis, QCD  $Z\gamma jj$  production, suffers from known mismodelling for high dijet masses, which is precisely corresponds to the

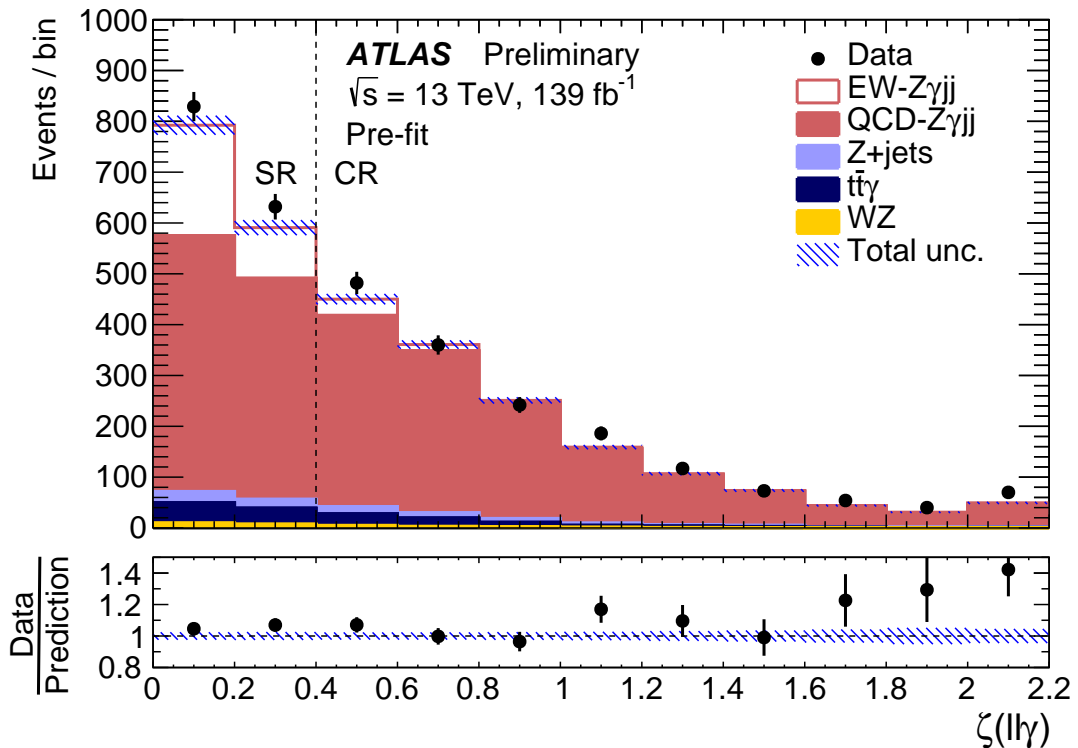


Figure 5.7: Centrality distribution for data, signal, and background estimates pre-fit (before any data corrections to QCD  $Z\gamma jj$ ). The dashed line marks the separation between the SR and QCD CR. The uncertainty band is the combination of uncertainties from background estimation, MC statistics, and experimental systematics. Overflow events are included in the last bin. [63]

region of interest in this analysis. Rather than using the MC template directly for estimating this background, the normalisation is corrected by comparing with data in a CR enriched in this background. The centrality variable is used to separate the SR ( $\zeta(ll\gamma) < 0.4$ ) from this QCD CR ( $\zeta(ll\gamma) > 0.4$ ). The CR is rich in the QCD background and has a very small fraction of signal events, as the EW production mechanism peaks at low values of centrality. Figure 5.7 shows the centrality distribution for signal and background events.

The normalisation correction is calculated by fitting a normalisation factor for the QCD background in the SR and CR simultaneously, allowing the overall normalisation to be adjusted according to data. The shape of the background is taken from MC, but data in the CR is used to validate this shape and constrain correlated

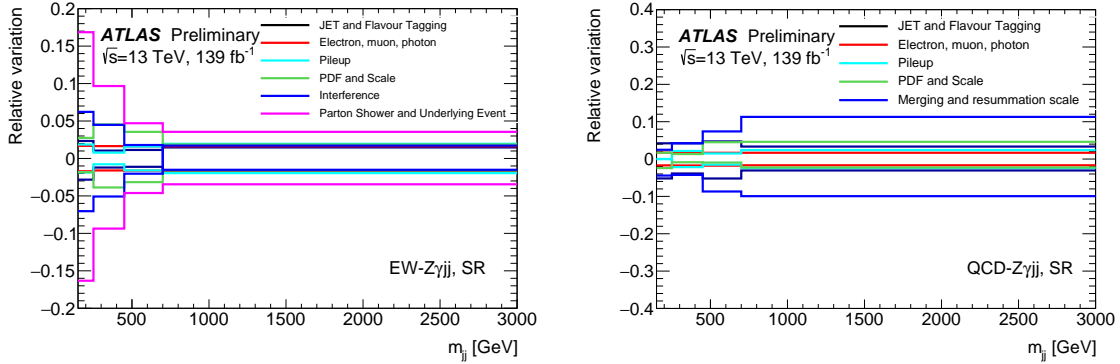


Figure 5.8: Plots of relative variation of yields as a function of dijet mass,  $m_{jj}$ , for EW (left) and QCD (right) production of  $Z\gamma jj$ . The variations shown are the largest groups of systematics in the SR. [63]

uncertainties.

Estimation for the remaining backgrounds;  $Z+jets$ ,  $t\bar{t}\gamma$ , and  $WZjj$ ; is detailed in Section 4.6.

## 5.5 Systematic uncertainties

The systematic uncertainties used in this analysis are discussed in Section 4.7. Figure 5.8 illustrates the relative effect of the largest groups of systematics is shown on both EW and QCD  $Z\gamma jj$  production, as a function of  $m_{jj}$ . The uncertainty on the normalisation of the  $Z+jets$  fake photon background is calculated following the prescription in Section 4.6.1.3 and determined to be 35% [63].

## 5.6 Jet flavour uncertainties

The uncertainties associated with the flavour composition and response of the jets in this analysis make a significant contribution to the result. This section presents measures taken to reduce these uncertainties and in turn improve the precision of the final measurement.

These jet flavour uncertainties, as discussed in Section 4.7.2.2, can be reduced by specifying the expected fraction of jets initiated by quarks and gluons in the analysis phase space.

The gluon fraction is defined as

$$f^{\text{gluon}} = \frac{N_j^{\text{gluon}}}{N_j^{\text{gluon}} + N_j^{\text{udsc}}},$$

where  $N_j^{\text{gluon}}$  and  $N_j^{\text{udsc}}$  are the number of jets initiated by gluons and by up/down/strange/charm quarks respectively. A given jet in a MC event is determined to be quark- or gluon-initiated from the truth record. Measuring both  $f^{\text{gluon}}$  and its associated uncertainty as a function of jet pseudorapidity and transverse momentum, for events passing the analysis selection, provides the information needed to reduce the jet flavour uncertainty.

This calculation is performed on events in the QCD  $Z\gamma$  MC sample, in the inclusive analysis region (defined by Table 5.1) and its subregions, the SR and the QCD CR. This study is not necessary for other samples as the uncertainties have a lesser impact on the final measurement.

Uncertainty on  $f^{\text{gluon}}$  arises from three sources: a modelling uncertainty calculated by comparing the  $f^{\text{gluon}}$  values obtained from two independent MC generators, statistical uncertainty resulting from the size of the MC sample used, and an additional uncertainty to cover any variations in the value of  $f^{\text{gluon}}$  between regions. The third uncertainty component is necessary due to technical limitations, which allowed only one  $f^{\text{gluon}}$  value to be provided for samples used to calculate yields in both the SR and the CR.

Calculation of  $f^{\text{gluon}}$  is performed for the QCD  $Z\gamma$  sample only, as this is where the jet flavour uncertainty is largest.

Figure 5.9 shows the gluon fractions measured in the nominal and alternate MC samples for QCD  $Z\gamma$ , as well as calculations of each of the uncertainty components.

The statistical uncertainty was found to be an order of magnitude smaller than the other components and so is neglected. The uncertainty to cover differences between regions is calculated by finding the largest difference, in each bin, between  $f_{\text{gluon}}$  in the inclusive region (SR+CR) and either of the two sub-regions. The overall uncertainty used is then the per-bin quadrature sum of the generator differences and this inter-region difference.

## 5.7 Template fit

The signal strength,  $\mu_{\text{EW}}$ , is used to parametrise the fiducial cross-section for the signal process,  $\sigma^{\text{EW}}$ , where

$$\mu_{\text{EW}} = \sigma_{\text{meas}}^{\text{EW}} / \sigma_{\text{SM}}^{\text{EW}}, \quad (5.3)$$

i.e. the ratio of the measured cross-section to the SM expectation. This signal strength is extracted from the data with a maximum likelihood fit, performed on  $m_{jj}$  distributions in the SR and CR simultaneously. MC distributions for backgrounds and signal are used as templates, with normalisations for the signal and QCD  $Z\gamma$  background allowed to float in the fit.

Electron and muon channels are treated together, using the sum of events from both for all aspects of the fit. Likelihood functions are built for each bin of the  $m_{jj}$  distribution in both the SR and CR using a Poisson distribution, and these are all combined to form a single extended likelihood

Systematic uncertainties are included in the fit as Gaussian nuisance parameters. The effect of each uncertainty on the normalisation and shape of the  $m_{jj}$  distribution is considered individually and a pruning system, described in Section 5.8, is used to reduce the number of nuisance parameters needed.

The fit extracts the value of the signal strength for the signal process,  $\mu_{\text{EW}}$ . From this a significance of the measurement, under the null hypothesis of  $\mu_{\text{EW}} = 0$ , can be extracted using the likelihood-ratio test. If the significance is greater than five standard

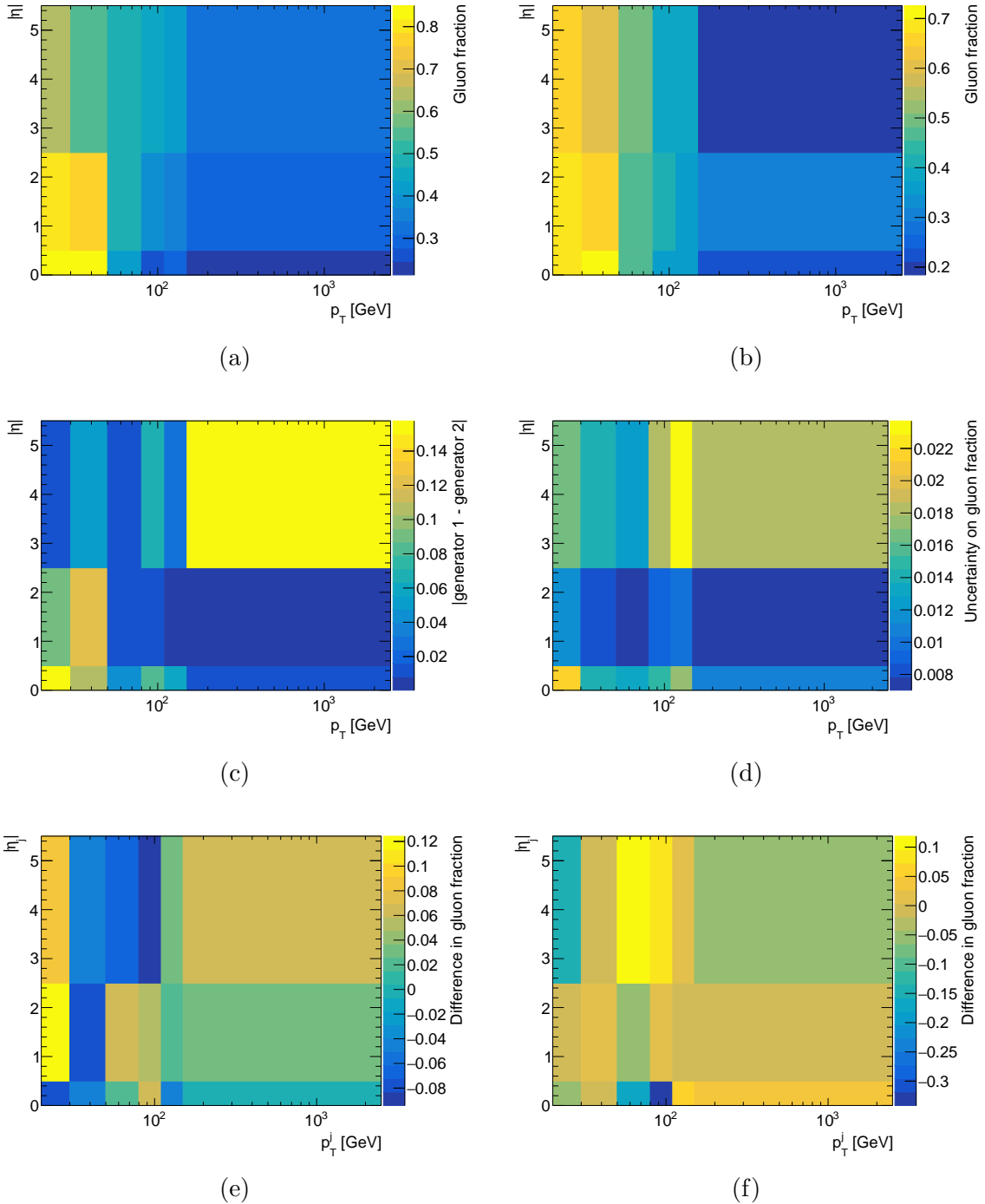


Figure 5.9: Gluon fractions and uncertainties as a function of jet pseudorapidity and transverse momentum. Plotted are gluon fraction in the nominal (a) and alternate (b) QCD  $Z\gamma$  sample MC samples, the difference between gluon fractions in these two samples (c), the statistical uncertainty on gluon fractions in the alternate sample (d) (this was the larger of the statistical uncertainties), and the difference between gluon fraction in the SR+CR region and in the SR (e) and CR (f) regions.

deviations, EW Z $\gamma$  production is considered to be observed. The value of the signal strength can also be used to give a measurement of the fiducial cross-section of the process, given the of the SM expectation of this cross-section, calculated from the nominal MC:

$$\sigma_{\text{SM}}^{\text{EW}} = 4.73 \pm 0.01 \text{ (stat.)} \pm 0.15 \text{ (PDF)}^{+0.23}_{-0.22} \text{ (scale) fb.}$$

## 5.8 Pruning systematic uncertainties

There are 74 experimental systematic uncertainties considered for this analysis. With each systematic requiring an up and down variations, 148 nuisance parameters would be needed in the fit. To limit the number of nuisance parameters, and stabilise the fit, a system is developed to rank the impact of different systematics on both the shape and normalisation of the  $m_{jj}$  distribution. Only systematic uncertainties deemed to be significant are fully accounted for in the fit, and those with less impact are pruned.

The first test for a systematic uncertainty is how uniform its effect is across the dijet mass spectrum – this will indicate whether it will impact the shape of the  $m_{jj}$  distribution. If a systematic is determined to have a significant impact on shape, by criteria discussed below, then it is included in the fit with one nuisance parameter for each bin in  $m_{jj}$ , allowing it to modify the shape in the fitting process.

Any uncertainty not found to impact the shape should be assessed for how significant an impact it has on the overall normalisation of events. Systematic uncertainties with a large enough effect on the event yield will contribute one nuisance parameter to the fit, and have the ability to scale the overall normalisation. Any uncertainties with a smaller effect will be pruned, i.e. all pruned systematics will be added in quadrature as a single extra nuisance parameter to scale the overall normalisation in the fit.

### 5.8.1 Calculating statistical uncertainties

In order to determine whether the effect of any systematic uncertainty, on shape or overall yield, is significant, the statistical uncertainty on the value of the systematic uncertainty must be ascertained. This statistical uncertainty arises from the finite size of MC samples used to evaluate systematic uncertainties.

The value of a systematic uncertainty on an event yield is given by

$$\sigma_{\text{Norm}} = \frac{N_{\text{varied}} - N_{\text{nominal}}}{N_{\text{nominal}}}, \quad (5.4)$$

where  $N_{\text{nominal}}$  is the number of events accepted for a nominal MC sample and  $N_{\text{varied}}$  is the number of events after the systematic variation has been applied. Each of  $N_{\text{varied}}$  and  $N_{\text{nominal}}$  has a statistical uncertainty. However, due to the fact that these variables are measuring the same set of events under different conditions, the two yields are highly correlated. The correlation is not known a priori, and so the uncertainty on  $\sigma_{\text{Norm}}$  cannot be calculated through error propagation.

The bootstrap method[64, 65] is instead used in order to determine statistical uncertainties while preserving correlations. This method relies on resampling the event set to create replica sets of events of the same size, with some events duplicated and some omitted. Calculating  $\sigma_{\text{Norm}}$  in each replica set gives a distribution of results for which the standard deviation represents the statistical uncertainty on  $\sigma_{\text{Norm}}$ .

### 5.8.2 Determining shape impact

For a systematic uncertainty that has no impact on  $m_{jj}$  shape, it would be expected that the resulting variation would be uniform across the  $m_{jj}$  distribution. This is tested by calculating the fractional difference in yield,  $\sigma_{\text{Norm}}$ , and its associated statistical uncertainty in bins of  $m_{jj}$ . A chi-squared test from fitting a zeroth order polynomial to these values provides a test statistic which should be distributed as  $\chi^2(3)$  (4 bins minus 1 parameter for 3 degrees of freedom) under the null hypothesis of

no shape impact. A significant shape uncertainty is therefore anything that deviates from this null hypothesis above a certain threshold. An example  $m_{jj}$  distribution and fit is shown in Figure 5.10, for a systematic uncertainty with an obvious impact on the shape.

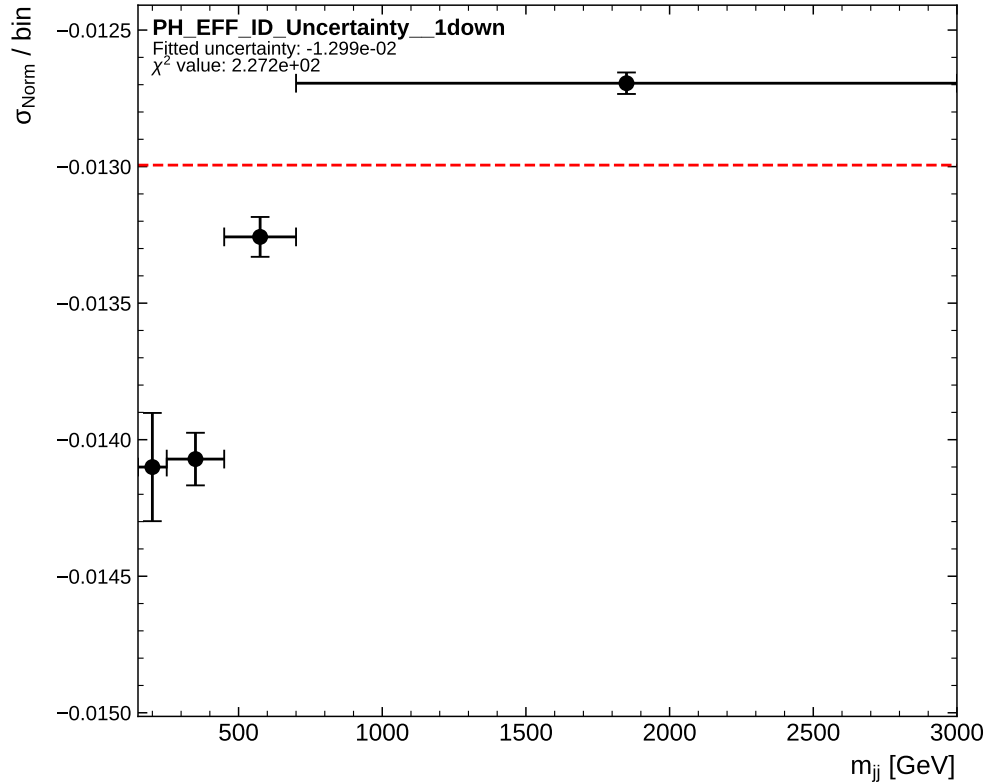


Figure 5.10: Binned  $m_{jj}$  distribution of measured systematic uncertainty,  $\sigma_{\text{Norm}}$ , for one systematic variation as labelled on the plot. The dashed line shows the zeroth-order polynomial fit attempted, with the indicated  $\chi^2$  value demonstrating this is clearly a poor assumption and this systematic does contribute an uncertainty on the  $m_{jj}$  shape.

The threshold chosen is a  $p$ -value of 0.05, i.e. chi-squared values sufficiently high that there is at most a 5% chance that the deviation arose from statistical fluctuation. Uncertainties with a  $p$ -value below this threshold have the full shape treatment in the fit, with per-bin nuisance parameters. Figure 5.11 shows the results of the chi-squared test for the largest experimental systematics in the SR. For the signal sample, 30 of the 74 experimental systematic uncertainties are significant, while for QCD  $Z\gamma$  there are 18 significant uncertainties.

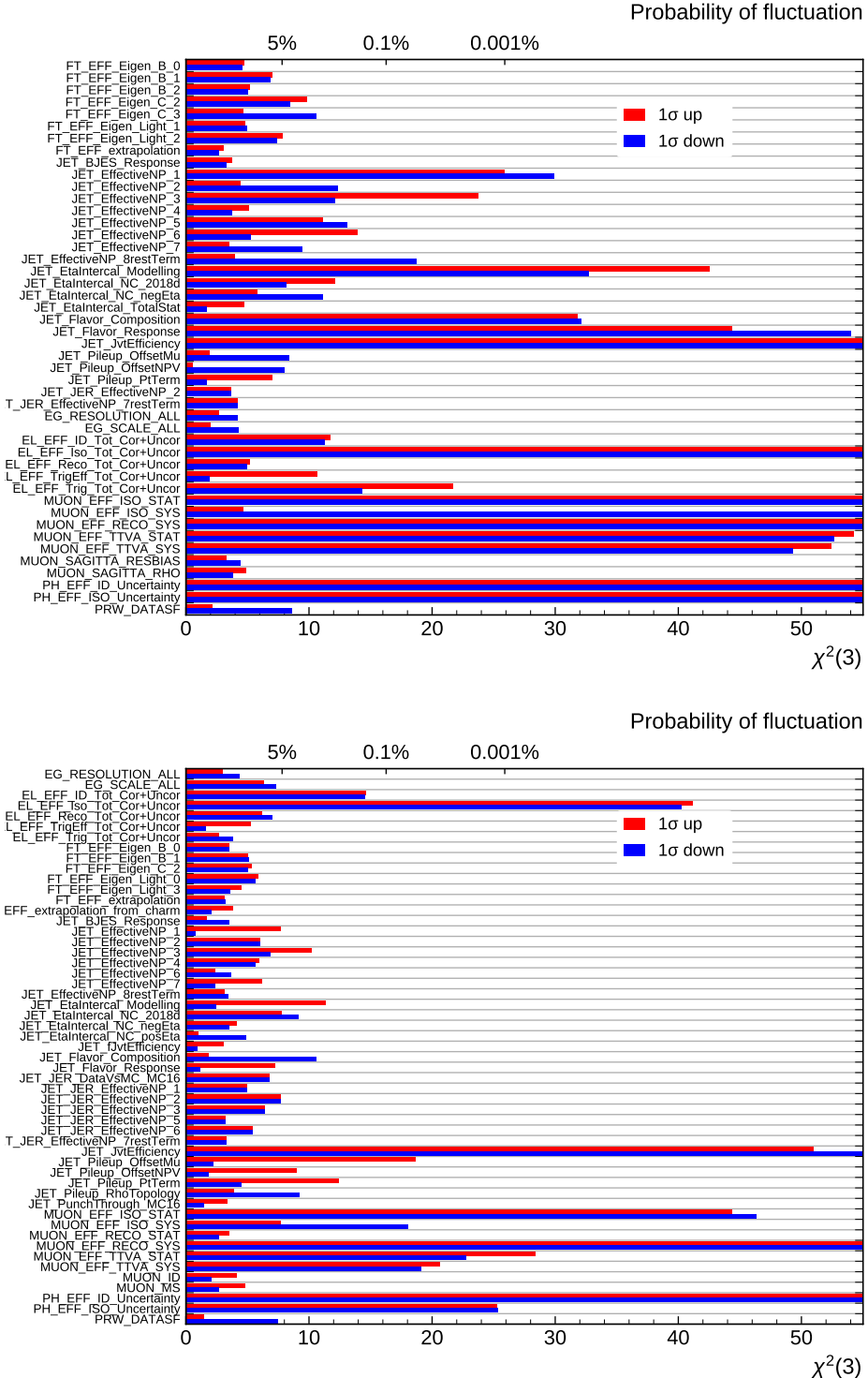


Figure 5.11:  $\chi^2$  values, representing the impact each systematic has on shape, for all experimental systematic variations in the EW (top) and QCD (bottom) samples in the SR. Only sources with  $\chi^2$  above 7 for either the up or down variation are shown. The top axis gives the probabilities of uncertainties arising fluctuations under the null hypothesis. The largest uncertainties extend beyond the range of the  $x$ -axis.

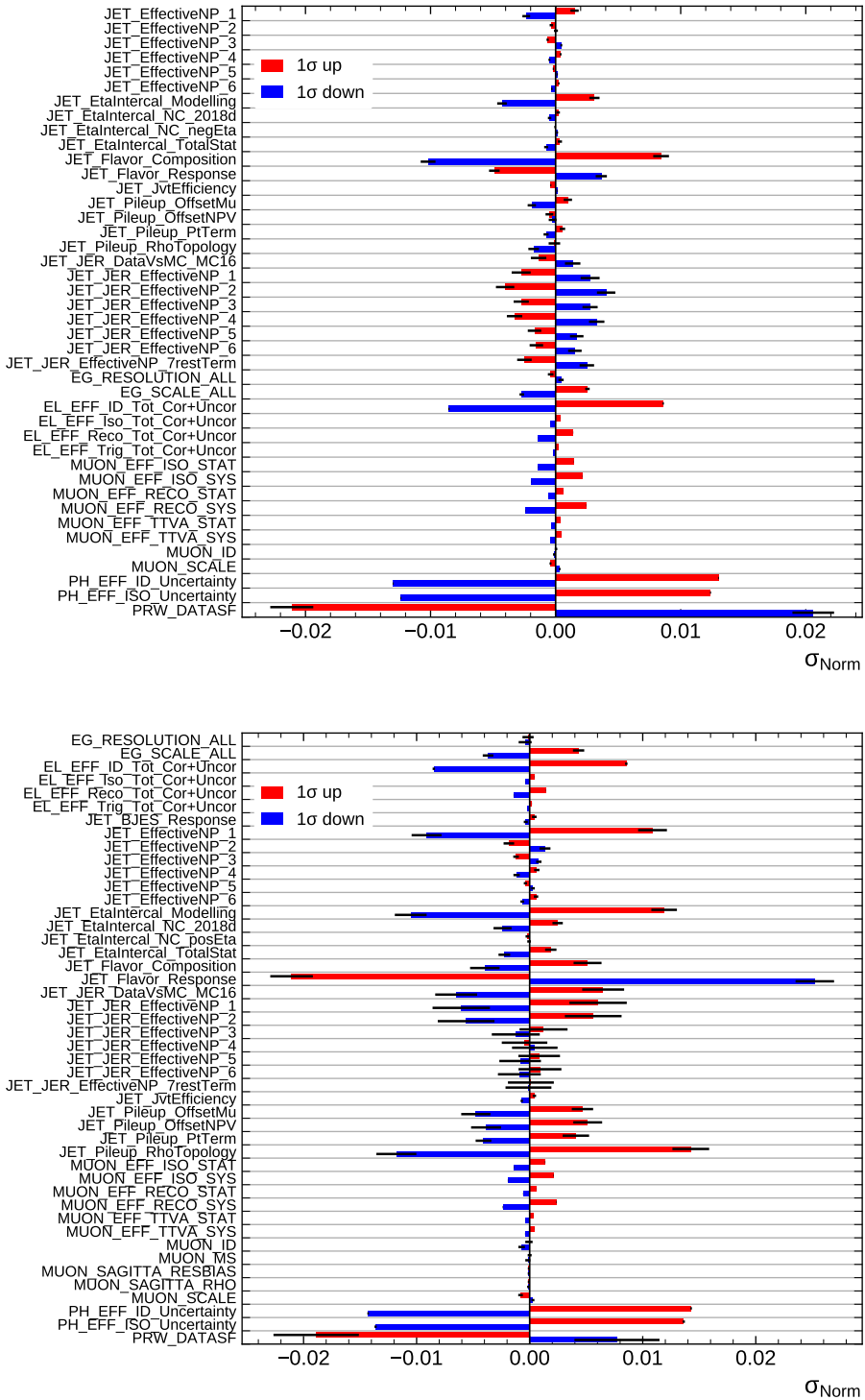


Figure 5.12: Overall normalisation uncertainty,  $\sigma_{\text{Norm}}$ , in the SR for the EW (top) and QCD (bottom) samples. Values for the largest experimental systematic uncertainties are shown, any with a value below  $5 \times 10^{-4}$  are omitted. The black bars represent the statistical uncertainty on the value.

### 5.8.3 Determining overall yield impact

Any systematic uncertainty determined to not impact the shape of the  $m_{jj}$  distribution can of course still affect the overall yield of events, and therefore require sufficient treatment in the fit. This could be done by assigning a single nuisance parameter to every remaining uncertainty, as all will have an effect on some scale. To reduce the number of nuisance parameters required however, the less significant uncertainties are pruned.

In this case significance is determined by whether or not a systematic uncertainty is consistent with zero. Taking the value of the systematic, per Equation 5.4, and its statistical uncertainty as the standard deviation, if the value is within one standard deviation of zero it is considered consistent with zero.

All systematic uncertainties not passing the shape significance test but not consistent with zero have a dedicated nuisance parameter in the fit. All remaining uncertainties are pruned. The relative change in yield from each of the largest experimental systematic uncertainties is shown in Figure 5.12.

## 5.9 Results

Fitted  $m_{jj}$  distributions are shown in Figure 5.13. The measured signal strength in the fit is

$$\begin{aligned}\mu_{\text{EW}} &= 0.95^{+0.14}_{-0.13} \\ &= 0.95 \pm 0.08 \text{ (stat.)} \pm 0.11 \text{ (syst.)}.\end{aligned}$$

This corresponds to an observed(expected) significance of 10(11) standard deviations, and is the first observation of this process by the ATLAS collaboration. As the measurement is consistent with  $\mu_{\text{EW}} = 1$ , the rate seen in data is consistent with the SM expectation.

The fiducial cross-section of the EW production of  $Z\gamma jj$  in this VBS-like phase space is therefore measured as

$$\sigma_{\text{EW}} = 4.49 \pm 0.40 \text{ (stat.)} \pm 0.42 \text{ (syst.) fb.}$$

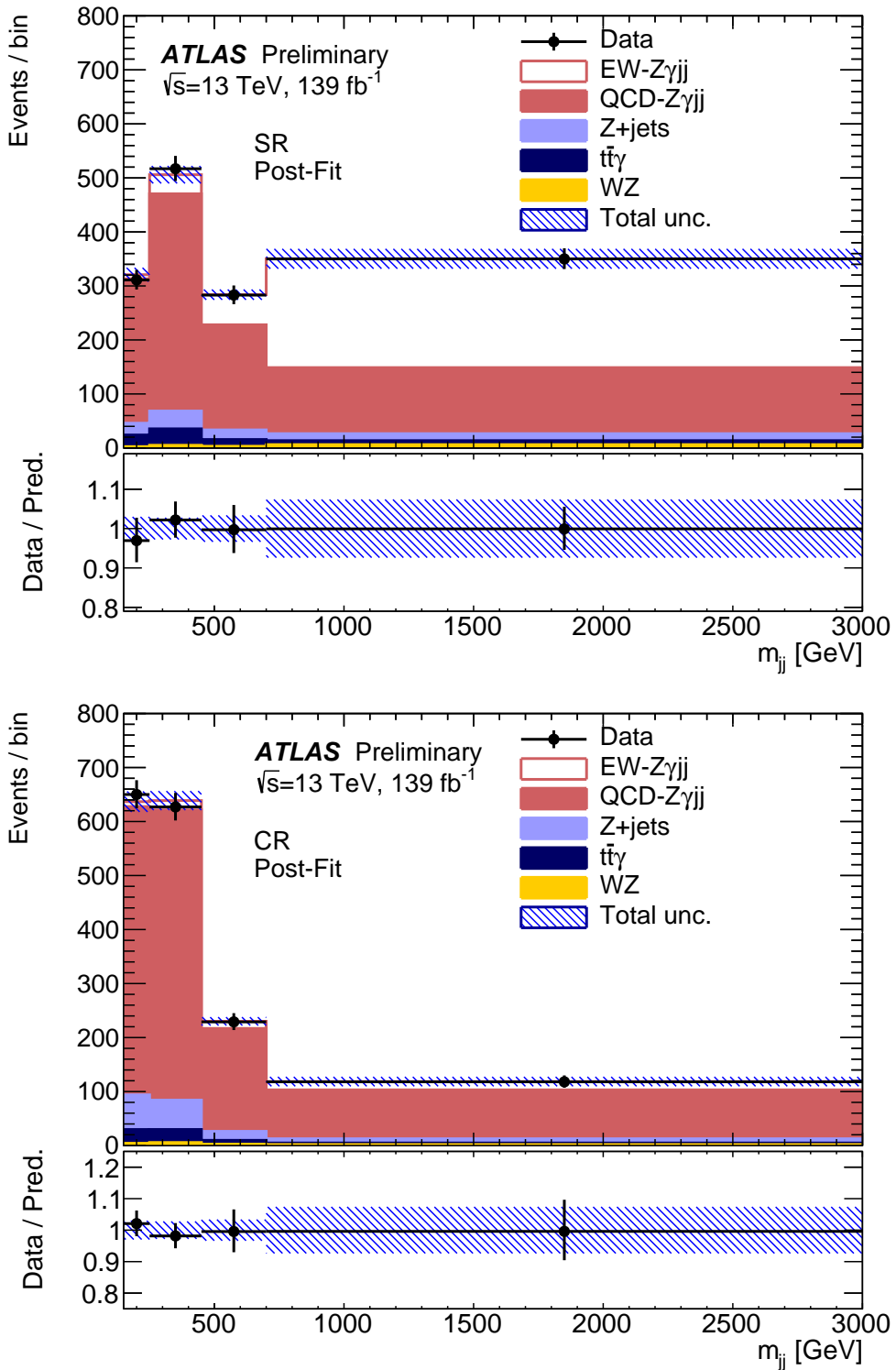


Figure 5.13: Post-fit distributions of dijet mass,  $m_{jj}$ , in the SR (top) and CR (bottom). The uncertainty band is the combination of all uncertainties, taken from the fit. Overflow events are included in the last bin. [63]

# CHAPTER 6

---

## Search for triboson production of $VZ\gamma$ through its semileptonic decay mode

---

### 6.1 Introduction

Triboson production of a Z boson; a photon; and an additional, hadronically decaying, vector boson is another production mechanism for the  $Z\gamma jj$  final state. This additional boson, denoted as a ‘V’ boson, can be a W or a Z boson. Measuring this  $VZ\gamma$  triboson process thus constitutes an inclusive measurement of both  $WZ\gamma$  and  $ZZ\gamma$  triboson production.

Figure 6.1 gives tree-level Feynman diagrams for  $WZ\gamma$  and  $ZZ\gamma$  production. Notably,  $WZ\gamma$  production is sensitive to the same QGC and TGC vertices as VBS  $Z\gamma$  production.  $ZZ\gamma$  is more limited by the lack of neutral QGCs and TGCs in the SM, but is therefore more sensitive to potential anomalous couplings. The reliance

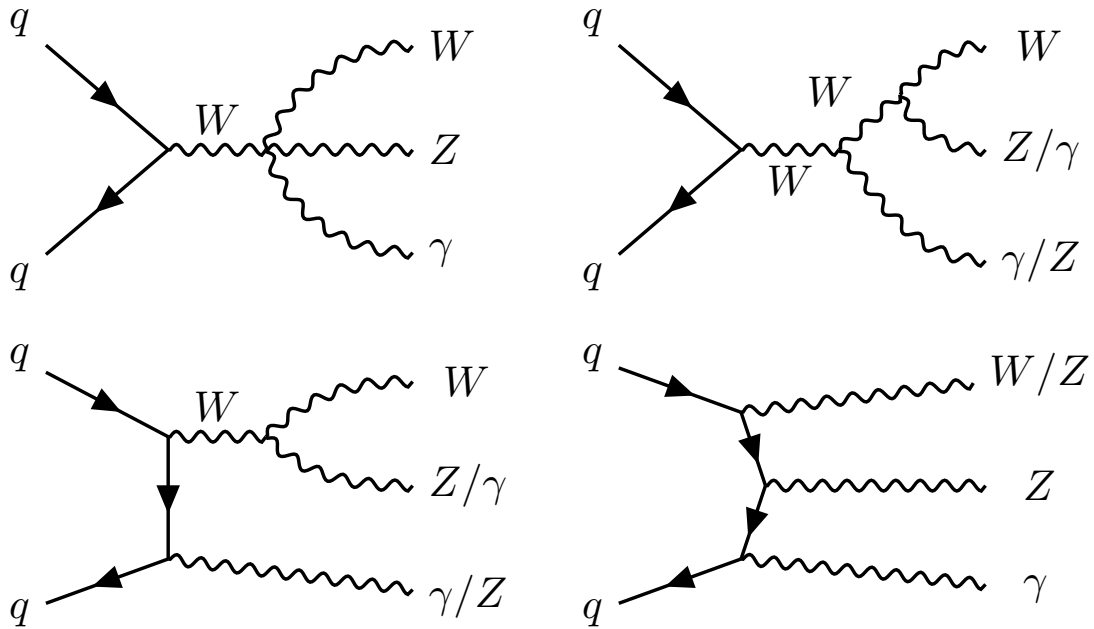


Figure 6.1: A selection of SM production mechanisms for the  $VZ\gamma$  triboson final state, depicted in Feynman diagrams.

on these rare multiboson interactions means that the triboson process has a low cross-section, similar to that of VBS  $Z\gamma$ . Without the distinct VBS jet signature to select on, measuring this low cross-section process is challenging.

The two jets, here a product of a boson decay, have kinematic properties that distinguish them from background events, notably: a dijet mass peaked around the  $W/Z$  masses, small rapidity separation between the two jets, and an angular distribution consistent with boson decay products. Additionally, more subtle differences are also present in many other variables. Selecting  $W/Z$  boson decays to leptons is relatively straightforward, but the more limited jet resolution and more dominant jet background makes doing this in the hadronic decay channel more difficult. This analysis employs machine-learning techniques to interpret this complicated phase space; pushing sensitivity beyond what is achievable with a traditional cut-based analysis.

Despite the differing jet phase space, the backgrounds for this analysis are the same as for the VBS  $Z\gamma$  analysis. QCD  $Z\gamma jj$  production is the dominant competing pro-

cess; the key difference between this background and the signal is the kinematics of the jets, as both have a real Z boson and photon produced. The QCD  $Z\gamma$  background has a yield X times higher than the signal after applying selection on the Z boson and photon. This illustrates the need for effective jet selection to manage this background.

The goal of this analysis is to measure the fiducial cross-section of this rare process in order to compare it to the standard model expectation. This measurement is extracted from a template fit to the ‘signal rarity’ distribution, derived from the output of a machine-learning model. If the observed significance is sufficient, this will provide evidence for or an observation of this process. If the significance does not meet these thresholds, the measurement will be used to place limits on the rate of this process. These limits can be used to constrain theories that might enhance the cross-section of this process.

## 6.2 Event Selection

Events in data and simulation, from the samples discussed in Section 4.2, undergo selection to create an analysis region sensitive to  $VZ\gamma$  triboson production. This section discusses an initial pre-selection applied to samples and the additional requirements used to define the signal sample. Measures to further refine the analysis region are discussed in Section 6.3.

### 6.2.1 Analysis region definition

A selection is applied to events to impose a loose triboson-like phase space, before more precise signal and control regions are defined with the help of the BDT discriminant discussed in Section 6.3.

The  $Z\gamma$  selection defined in Section 4.4 is first applied to events. Events are then

VZ $\gamma$ selection	
Z $\gamma$ system	Z $\gamma$ selection (Table 4.2)
Jet	$N_j \geq 2$ $ y_j  < 4.4$ $p_T^{j,1} > 40$ GeV $p_T^{j,2} > 30$ GeV
Dijet system	$m_{jj} < 150$ GeV $ \Delta y_{jj}  < 2$

 Table 6.1: Summary of event selection criteria defining the VZ $\gamma$  analysis region.

required to have at least two jets, each with rapidity  $|y_j| < 4.4$ . The leading jet must have a transverse momentum of at least 40 GeV, and the sub-leading jet at least 30 GeV. The invariant mass of the dijet system must satisfy  $m_{jj} < 150$  GeV, and the rapidity separation of the jets  $|\Delta y_{jj}| < 2$ . These cuts are summarised in Table 6.1.

Many of these jet variables are later employed by the BDT to refine selection but adding loose preselection reduces complexity at no cost to performance, see Section 6.3 for a more detailed discussion. The  $m_{jj}$  cut ensures that this analysis is orthogonal to the VBS Z $\gamma$  analysis (which uses a cut of  $m_{jj} > 150$  GeV), and is also compatible with the expected signal values of  $m_{jj} \sim m_W, m_Z$ .

These cuts define the full analysis region, further cuts on the BDT output and  $m_{jj}$  are used to define the SR and CRs, discussed in Section X.

### 6.2.2 EW VZ $\gamma$ definition

Triboson VZ $\gamma$  production forms a subset of the processes under the umbrella of EW Z $\gamma$ jj production. Only interactions where the two jets are a product of a boson decay should contribute to the signal process. Other forms of EW Z $\gamma$ jj production, such as the diagrams in Figures 5.1 and 5.2, should ideally be considered as a source of background.

This analysis defines two samples as orthogonal subsets of the EW  $Z\gamma jj$  production sample detailed in Section 4.2: EW  $VZ\gamma$  (the signal sample) and EW  $Z\gamma jj$  background (or the EW background). These samples are separated using truth information.

Two variables are used to test if the jets are products of a W or Z boson decay:  $m_{jj}^{\text{truth}}$ , the invariant mass of the dijet system calculated at truth level, and `PartonTruthLabelID`, which indicates the flavour of the parton initiating each jet<sup>1</sup>. The constraint  $74 \leq m_{jj}^{\text{truth}} \geq 99$  GeV is applied for events included in the  $VZ\gamma$  sample, chosen as it contains 95% of the combined W and Z boson lineshape and so should select 95% of W/Z( $\rightarrow jj$ ) events. Events included in  $VZ\gamma$  are also required to have `PartonTruthLabelID` values compatible with quark flavours from a W or Z decay, i.e. both jets are quark-initiated and either both the same flavour (e.g. both up quarks as in  $Z \rightarrow u\bar{u}$ ) or one up-type and one down-type quark (e.g. an up and a strange quark as in  $W \rightarrow u\bar{s}$ ). Any events failing either of these cuts are included in the EW background sample.

This selection is not 100% efficient and as such there is some cross-contamination between the samples. Nevertheless, applying this truth selection increases the probability that any event considered signal contains the physics processes of interest, direct multiboson interactions. Of the events passing the preselection in Table 6.1 for the full EW  $Z\gamma jj$  sample, 31% are accepted to the  $VZ\gamma$  signal sample and the remaining 69% make up the EW background.

### 6.3 Discriminating against QCD $Z\gamma$ production

The biggest challenge in this analysis is managing the dominant background, QCD  $Z\gamma jj$  production. Like the signal process, this background has a real Z boson and photon. The difference is the origin of the jets, here not from a boson decay but

---

<sup>1</sup>This variable informs on whether the parton is a quark or a gluon and the quark flavour (e.g. up, down, strange, etc.) but does not distinguish between a quark and an anti-quark, that information was not available in the sample.

more likely radiated from the initial or final state. Identifying and exploiting the differences in jet kinematics between this background and the signal is therefore key to maximising the sensitivity of the measurement. This section is dedicated to discussing this problem; the word ‘signal’ is used here to refer to EW  $VZ\gamma$  production and ‘background’ refers solely to QCD  $Z\gamma jj$  production.

There are a small number of kinematic distributions which exhibit a large difference between signal and background that could be exploited effectively by a cut. The dijet mass,  $m_{jj}$ , is an obvious example as for the signal it peaks around the W/Z boson mass but for the background resembles a continuum.

For many more variables however, the differences are more subtle. There may be an obvious difference in shape between signal and background but there is no obvious cut or set of cuts that would create a signal-rich region. Figure 6.2 shows some distributions with the largest signal-background discrepancies.

Building a cut-based selection with sensitivity to the signal is difficult, more advanced methods might push the background rejection further. This section explores and compares two methods for defining a signal-sensitive phase space for the analysis: a cut-based approach and a BDT, a machine learning classifier introduced in Section [BDT section in theory chapter].

The dijet mass variable is excluded from being used for selection in either of these methods. This allows it to be used to define CRs with a low signal purity in order to validate background estimates with comparisons to data. For more detail on the definition and use of these CRs, see Section X.

These initial investigations were performed before many details of the analysis were established and so have a unique phase space, detailed below.

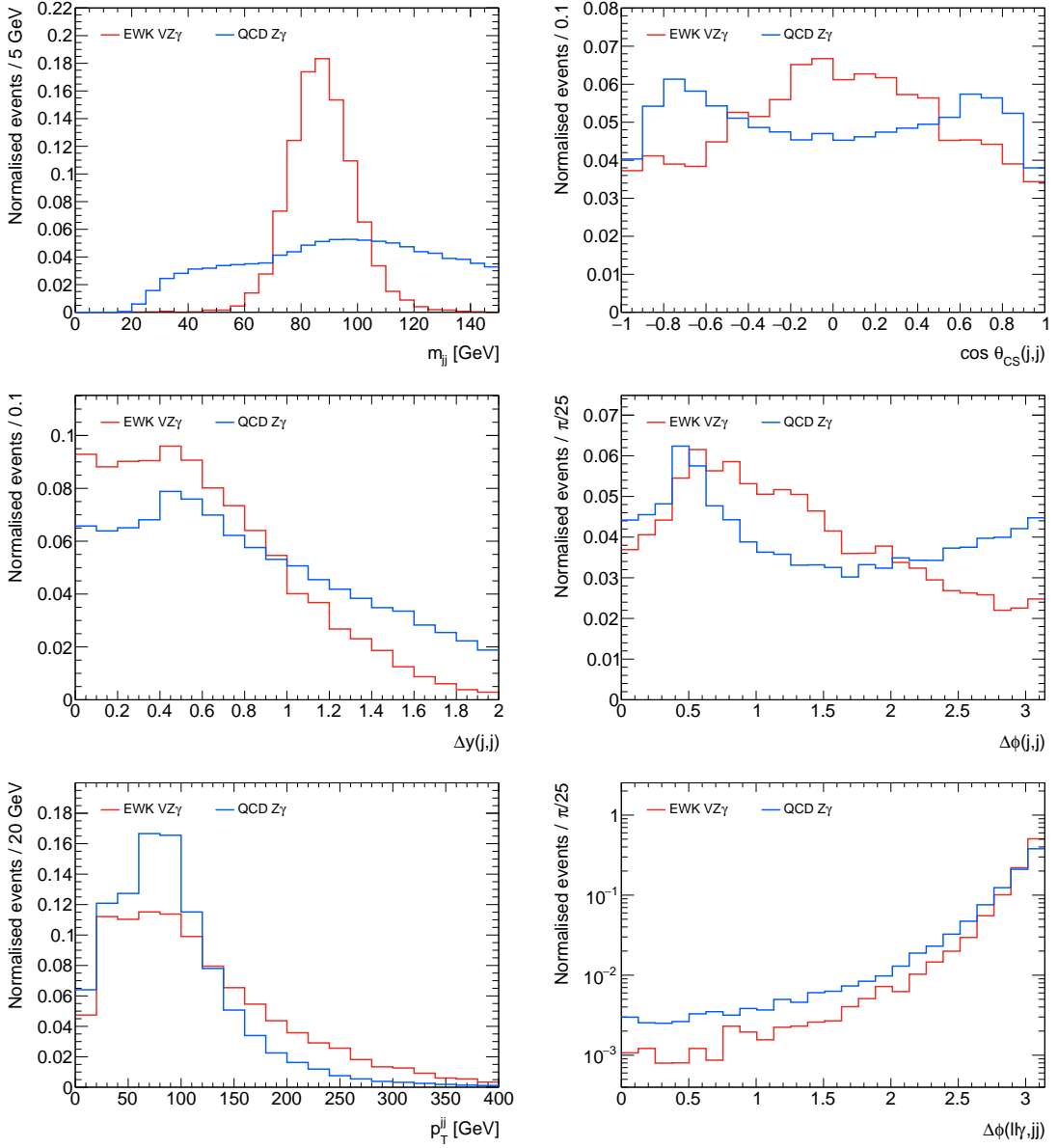


Figure 6.2: Kinematic distributions, comparing EW  $VZ\gamma$  production (red) to QCD  $Z\gamma jj$  production (blue). Generated from the corresponding MC samples with  $VZ\gamma$  preselection applied. Events are normalised to compare the shape of distributions between the two samples.

Table 6.2: Selection for events used in background rejection studies for the VZ $\gamma$  triboson analysis. This is the same as the Z $\gamma$  selection in Table 4.2 but with a looser photon  $p_T$  cut and no FSR cut.

Background rejection studies preselection	
Photon	$N_\gamma \geq 1$ $ \eta_\gamma  < 2.37$ (excludes $1.37 <  \eta_\gamma  < 1.52$ ) $p_T^\gamma > 15$ GeV
Lepton	$N_l = 2$ (OSSF) $ \eta_e  < 2.47$ (excludes $1.37 <  \eta_e  < 1.52$ ) $ \eta_\mu  < 2.5$ $p_T^{l,1} > 30$ GeV $p_T^{l,2} > 20$ GeV
Boson	$m_{ll} > 40$ GeV

### 6.3.1 Phase space for preliminary studies

The studies presented in this section use events from the EW VZ $\gamma$  sample (as defined in Section 6.2.2) as the signal and from the QCD Z $\gamma$  sample as the background. All events are subject to the preselection in Table 6.2. These cuts select Z $\gamma$  events with an earlier version of the full Z $\gamma$  selection presented in Section 4.4. No cuts are placed on the jets at this stage. Isolation, identification, and overlap removal for all objects are the same as discussed in Section 4.4.

### 6.3.2 Comparison metric

A metric is needed in order to evaluate the performance of a given selection. Since the desired selection will be one that grants the most sensitivity to the VZ $\gamma$  signal, a significance of the signal considering a background-only hypothesis is used. This will emulate the significance calculation used for the final measurement, though much simplified as it deals with only a single background and no systematic uncer-

tainties. Whilst the significances given here are not comparable to that from a full measurement, they are comparable with each other and will indicate which selection generates more sensitivity to the signal process.

As the  $m_{jj}$  distribution is not used for selection, it is used here to calculate significance with a binned likelihood method. Consider  $n_b^i$  as the number of background events in bin  $i$ , and  $n_s^i$  the number of signal events, from the relevant MC samples after selection. The likelihood of observing  $n_{\text{obs}}^i$  events in bin  $i$  is given by a Poisson distribution with a mean of  $n_b^i + \mu \cdot n_s^i$ , where  $\mu$  is a signal strength parameter with  $\mu = 0$  for the background-only hypothesis or  $\mu = 1$  for alternate hypothesis with signal included. The likelihood,  $\mathcal{L}$ , of observing the set of  $\{n_{\text{obs}}^i\}$  in each bin is then the product of each of the per-bin likelihoods.

Constructing the likelihood ratio

$$\lambda = \frac{\mathcal{L}(\{n_{\text{obs}}^i\}; \mu = 0)}{\mathcal{L}(\{n_{\text{obs}}^i\}; \mu = 1)},$$

enables a likelihood-ratio test, with the test statistic  $-2 \ln \lambda$  distributed as  $\chi^2(1)$  [66], to calculate the significance of observing  $\{n_{\text{obs}}^i\}$ .

To obtain integer values for  $n_{\text{obs}}^i$  from the MC prediction, as required by the use of the Poisson distribution, random toy experiments are run. For each experiment,  $n_{\text{obs}}^i$  is picked at random from a Poisson distribution with mean  $n_b^i + n_s^i$ . Running 1000 of these experiments, calculating the significance for each, and taking the mean of the results gives an estimate for the significance.

These significances are calculated for each selection tested, given as a number of standard deviations.

### 6.3.3 Selection variables

Building a selection to reject the QCD Z $\gamma$  background relies on identifying differences in jet kinematics, and therefore placing selection requirements on jet-based kinematic variables. A number of variables are considered, with the full list given in Table 6.3.

The variable  $p_T^{\text{balance}}$  is given by the equation

$$p_T^{\text{balance}} = \frac{(p_T^{jj} - p_T^{ll\gamma})}{(p_T^{jj} + p_T^{ll\gamma})}. \quad (6.1)$$

### 6.3.4 Cut-based background rejection

The task at hand is to find a set of cuts to make, on variables from Table 6.3, in order to maximise sensitivity to the signal process. Truly optimising this, finding the best value for each cut given the values of every other cut, is a many-dimensional problem with no reasonable solution. Instead an iterative approach is taken: find the best cut on each variable individually, take the variable with the cut gives the best improvement in sensitivity and add it to the selection, then re-test all other cuts on the new subset of events.

Identifying the ‘best’ cut to make at any stage is a little subjective. For instance, when applying the first cut, the selection that would result in the best significance for the signal sample is likely too aggressive to allow for multiple effective cuts afterwards. The method used is to calculate background rejection (1/fraction of background events passing a cut) as a function of signal efficiency (fraction of signal events passing a cut) for each variable. By eye, these distributions can then be scanned to identify a possible cut which gives large background rejection but maintains a high signal efficiency. This allows for multiple variables to be included in the selection before the phase space becomes too constrained.

Figure 6.3 shows the background rejection against signal efficiency for  $p_T^j, 2$ , which

Table 6.3: Variables considered for selection to reject QCD  $Z\gamma$  events for the  $VZ\gamma$  triboson analysis.

Variable	Definition
$y_{j,1}$	Rapidity of the leading jet in the event.
$y_{j,2}$	Rapidity of the sub-leading jet in the event.
$y_{jj}$	Rapidity of the $jj$ system.
$p_T^{j,1}$	Transverse momentum of the leading jet in the event.
$p_T^{j,2}$	Transverse momentum of the sub-leading jet in the event.
$p_T^{jj}$	Transverse momentum of the $jj$ system.
$p_T^{\text{balance}}$	Relative difference between transverse momenta of the $jj$ and $ll\gamma$ systems, given by Equation 6.1.
$N_j$	Number of jets in the event, reconstructed with a minimum $p_T$ of 25 GeV.
$N_j^{\text{gap}}$	Number of jets, satisfying $p_T > 25$ GeV found in the rapidity region between the two leading jets.
$m_{j,1}$	Mass of the leading jet in the event.
$m_{j,2}$	Mass of the sub-leading jet in the event.
$m(ll\gamma jj)$	Mass of the triboson system.
$ \Delta y_{jj} $	Absolute rapidity difference between the two leading jets.
$\Delta\phi_{jj}$	Smallest difference between the azimuthal angles of the two leading jets.
$\Delta R_{jj}$	$\Delta R$ value between the two leading jets.
$ \Delta y(ll\gamma, jj) $	Absolute rapidity difference between the $ll\gamma$ and $jj$ systems.
$\Delta\phi(ll\gamma, jj)$	Smallest difference between the azimuthal angles of the $ll\gamma$ and $jj$ systems.
$\Delta R(ll\gamma, jj)$	$\Delta R$ value between the $ll\gamma$ and $jj$ systems.
$\Delta R_{\min}(\gamma, j)$	Minimum $\Delta R$ value between any photon and jet in the event.
$\cos\theta^*(jj)$	Cosine of $\theta^*(jj)$ , the angle of the leading jet in the dijet centre-of-mass frame relative to the direction of motion of the $jj$ system.
$\cos\theta_{\text{CS}}(jj)$	Cosine of $\theta_{\text{CS}}(jj)$ , the angle between the two jets in the Collins-Soper frame [67]. Jet charge information isn't available so the angle is taken relative to the leading jet.
$\zeta(ll\gamma)$	Centrality of the $ll\gamma$ system, given by Equation 5.1.

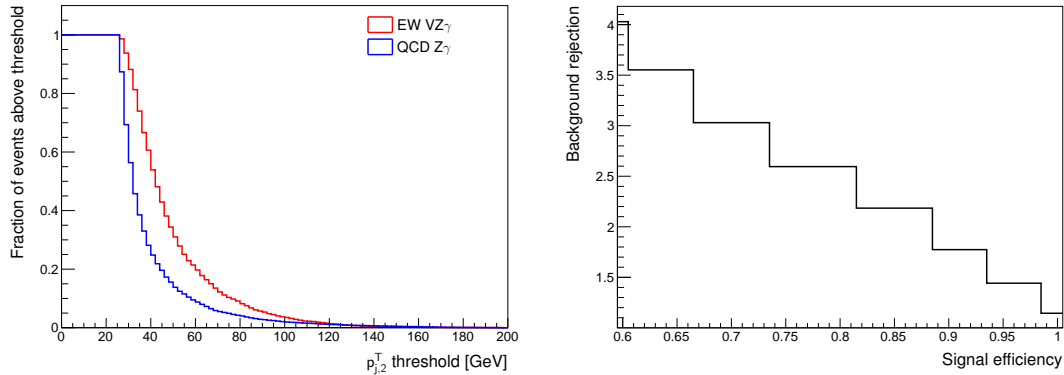


Figure 6.3: Distributions to identify a cut on  $p_T^{j,2}$ . Shown are fraction of events for each sample that are above a given threshold value in  $p_T^{j,2}$  (left) and background rejection as a function of the signal efficiency achievable using the same  $p_T^{j,2}$  threshold (right).

is the variable chosen to apply a cut on first. A cut of  $p_T^{j,2} > 35$  GeV is chosen, with a signal efficiency of 74% and a background rejection factor of 2.6.

Continuing this process, the most performant selection found consisted of five cuts, listed in Table 6.4. Using the method described in Section 6.3.2, the significance calculated for events passing this selection is 1.2 standard deviations.

Table 6.4: Selection derived for baseline cut-based version of the analysis. Cuts are applied to the  $VZ\gamma$  signal sample and the QCD  $Z\gamma$  background for events passing the preliminary selection given in Table 6.2.

Cut-based selection
$p_T^{j,2} > 35\text{GeV}$
$ \Delta y_{jj}  < 1.5$
$\Delta R(l\ell\gamma, jj) > 3.0$
$\Delta\phi(l\ell\gamma, jj) > 2.8$
$p_T^{\text{balance}} > -0.1$

### 6.3.5 BDT for background rejection

The cut-based selection provides a baseline performance against which to evaluate a BDT-based selection. The BDT can take many variables as input and determine how likely an event is to be signal or background based on the value of those variables,

having first learned how the variables are distributed differently between signal and background events.

The first step is to train a BDT to identify these differences between signal and background. Once trained, the BDT is tested on an independent set of events to evaluate its performance and test for overtraining. To accommodate this train-test cycle, the signal and background samples are each split evenly into two, one half used for training and the other for testing.

[Overtraining will be discussed in theory section]

Several aspects of the BDT are tuned to improve performance: the input variables used by the BDT, preselection applied to events before training, and hyperparameters of the BDT itself. These are discussed in the sections below.

#### 6.3.5.1 Input variable selection

The benefit of the BDT is its ability to handle many input variables and generate a phase space sensitive to the signal. However, giving too many variables to the BDT creates an overly complex model and allows for overtraining. Many iterations of input variables were tested to find a set that is sufficiently small to prevent overtraining but with enough variables to allow the BDT to maximise the sensitivity.

For each set of variables tested, a simple overtraining check is used. For a cut on the BDT output resulting in a background rejection factor of 10, the corresponding signal efficiency is compared between the training sample and the test sample. Overtraining would result in a higher signal efficiency in the training sample than in the test sample. A requirement that the test sample signal efficiency is within 10% of the training sample is used to mitigate overtraining in the BDT model.

Sensitivity attained by a BDT trained on a given variable set is evaluated by calculating the significance through the method discussed in Section 6.3.2. To do this, a cut must first be placed on the BDT output. The value chosen for this cut will

affect the sensitivity, so in each instance many cut values are tested and the highest significance is taken to represent the sensitivity of the BDT.

After using these tests to compare many combinations of variables, the most performant set was chosen. The final set of 16 input variables is shown in Table 6.5 ranked by their ‘importance’ as determined by the BDT. See section [BDT section in theory chapter] for details on how variable importance is calculated.

Table 6.5: Ranking of variables used by the BDT to discriminate between signal and background for the  $VZ\gamma$  analysis.

Rank	Variable	Relative importance
1	$ \Delta y_{jj} $	$7.46 \times 10^{-2}$
2	$p_T^{j,2}$	$7.27 \times 10^{-2}$
3	$\Delta\phi_{jj}$	$7.24 \times 10^{-2}$
4	$m_{j,2}$	$7.06 \times 10^{-2}$
5	$p_T^{\text{balance}}$	$7.05 \times 10^{-2}$
6	$\Delta R_{\min}(y, j)$	$6.50 \times 10^{-2}$
7	$y_{j,2}$	$6.32 \times 10^{-2}$
8	$\Delta\phi(ll\gamma, jj)$	$6.15 \times 10^{-2}$
9	$\cos\theta_{\text{CS}}(jj)$	$6.10 \times 10^{-2}$
10	$p_T^{j,1}$	$5.76 \times 10^{-2}$
11	$y_{j,1}$	$5.70 \times 10^{-2}$
12	$p_T^{jj}$	$5.68 \times 10^{-2}$
13	$\Delta R(ll\gamma, jj)$	$5.68 \times 10^{-2}$
14	$m_{j,1}$	$5.60 \times 10^{-2}$
15	$\log\zeta(ll\gamma)$	$5.48 \times 10^{-2}$
16	$y_{jj}$	$4.96 \times 10^{-2}$

The logarithm of the centrality,  $\zeta(ll\gamma)$ , is taken rather than the centrality itself as it extends to very high values. The method of binning variables employed by the BDT left little available discrimination power with the original form of the variable. Figure 6.4 shows the effect of the logarithm.

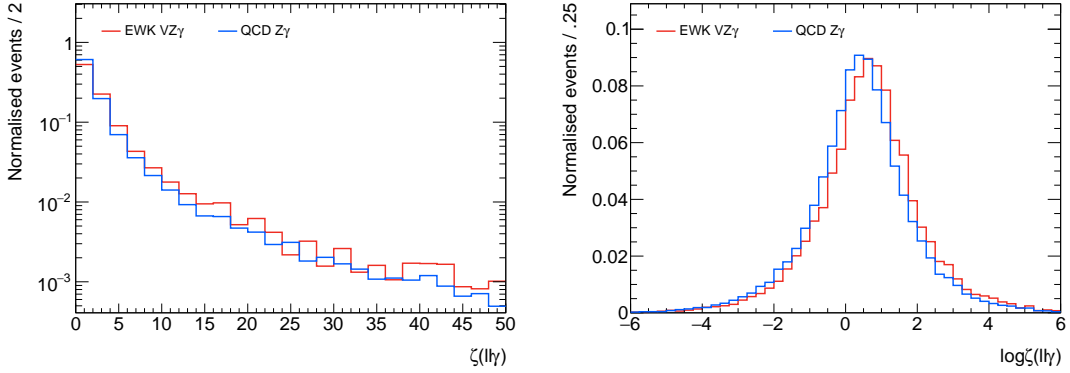


Figure 6.4: Distribution of centrality,  $\zeta(ll\gamma)$ , both without (left) and with (right) the logarithm applied. Normalised events are shown for the  $VZ\gamma$  signal sample and the QCD  $Z\gamma$  background.

### 6.3.5.2 Preselection and training cuts

Another route to improving performance of the BDT is constraining the phase space to further simplify the signature the BDT is trying to identify. Even in cases where there is no performance increase, reducing the phase space without significant loss in signal efficiency is still beneficial as it can help to reduce the impact of systematic uncertainties. It also improves the interpretability of the analysis phase space; cuts on simple kinematic variables are much more easily understood than a cut on a BDT output.

Two types of selection are used for this purpose: preselection applied to all events, including those input to the BDT, and training cuts applied only to events when provided to the BDT for training. Preselection will narrow the whole analysis phase space whilst training cuts give the BDT a more focused view of the signal and background.

Three preselection cuts are applied, on top of the baseline selection for these studies given in Table 6.2. Minimum jet transverse momentum is included for both leading and sub-leading jets. Each is set to the highest value that did not degrade the sensitivity of the BDT:  $p_T^{j,1} > 40$  GeV and  $p_T^{j,2} > 30$  GeV. This reduces the impact of any systematic uncertainties that behave poorly for low- $p_T$  jets. A requirement is also placed on the rapidity difference  $|\Delta y_{jj}|$ . Artefacts were found in the BDT

response for background events with high  $|\Delta y_{jj}|$ ; a cut of  $|\Delta y_{jj}| < 2$  was found to remove these issues and have no impact on sensitivity.

A training cut is made on the dijet mass,  $m_{jj}$ , to focus on a more signal-rich region. Applying a training cut of  $60 < m_{jj} < 115$  GeV was found to improve BDT performance. Tighter mass window cuts were tested and no further improvements were found. This cut is only applied for training the BDT, and not as a preselection cut, to preserve its use for defining CRs.

### 6.3.5.3 Hyper-parameter optimisation

A BDT implementation has hyper-parameters that instruct it on how to build decision trees during training, as discussed in Section [theory:BDT]. Four hyper-parameters were investigated to optimise performance of the BDT used for this analysis: the number of cuts tested across the range of a variable when splitting nodes,  $N_{\text{cuts}}$ ; the number of trees in the forest,  $N_{\text{trees}}$ ; the maximum allowed depth of each decision tree,  $d_{\max}$ ; and the  $\beta$  parameter which controls the rate of learning by modifying the boost weights.

Each parameter was tested in turn, training and testing the BDT to evaluate overtraining and sensitivity through the same procedure as in Section 6.3.5.1. Values for  $N_{\text{cuts}}$  between 2 and 500 were tested and the greatest sensitivity was achieved with  $N_{\text{cuts}} = 90$ , with no significant overtraining. Numbers of trees between 300 and 1500 were tested, with optimal sensitivity obtained for  $N_{\text{trees}} = 850$ . The  $d_{\max}$  hyper-parameter was tested for values from 1 to 9 and the sensitivity was found to increase for increasing  $d_{\max}$ . However, deeper trees also became more prone to overtraining. A value of  $d_{\max} = 3$  was chosen as the best balance between sensitivity and overtraining. The boost  $\beta$  parameter was tested with a range of values between 0 and 1,  $\beta = 0.5$  was chosen with the best sensitivity and no significant overtraining.

### 6.3.5.4 Overall performance

With all of the optimisations made, the best significance obtained for events passing a BDT cut is 1.5 standard deviations. This represents a sizeable improvement over the 1.2 standard deviations obtained with the cut-based approach, and motivates use of the BDT in this analysis.

## 6.4 Signal and control regions definition

Given the baseline selection from Section 6.2 and the BDT discriminant developed in Section 6.3, additional selection cuts can be applied to define signal and control regions for use in the fit. By further constraining the analysis region in constructing the SR, the sensitivity to the analysis to the signal process is improved. Additionally, the use of orthogonal CRs with minimal signal leakage enables data-MC comparisons before unblinding, to confirm validity of background modelling, and also gives the fit more data with which to constrain systematic uncertainties.

One SR and three CRs are used for this analysis. The four regions are divided by two variables:  $m_{jj}$  and signal rarity. Signal rarity, or  $\mathcal{R}_{\text{BDT}}^{\text{sig}}$ , is a transformation of the BDT output defined in Section [theory:BDT]. These two variables are plotted in Figure 6.5, for events in the analysis region.

The dijet mass distribution is split into three regions, a lower sideband ( $30 < m_{jj} < 65$  GeV), the on-peak region ( $70 < m_{jj} < 100$  GeV), and an upper sideband( $110 < m_{jj} < 150$  GeV). The lower and upper sidebands form CRs for the analysis, and the on-peak region is further divided by a cut on signal rarity into the SR ( $\mathcal{R}_{\text{BDT}}^{\text{sig}} > 0.8$ ) and the BDT CR ( $\mathcal{R}_{\text{BDT}}^{\text{sig}} < 0.8$ ).

The  $m_{jj}$  cut defining the on-peak region was roughly optimised by approximating the significance obtained for each pair of minimum and maximum  $m_{jj}$  cuts, given the number of signal and background events from all samples passing the cut. Figure 6.6

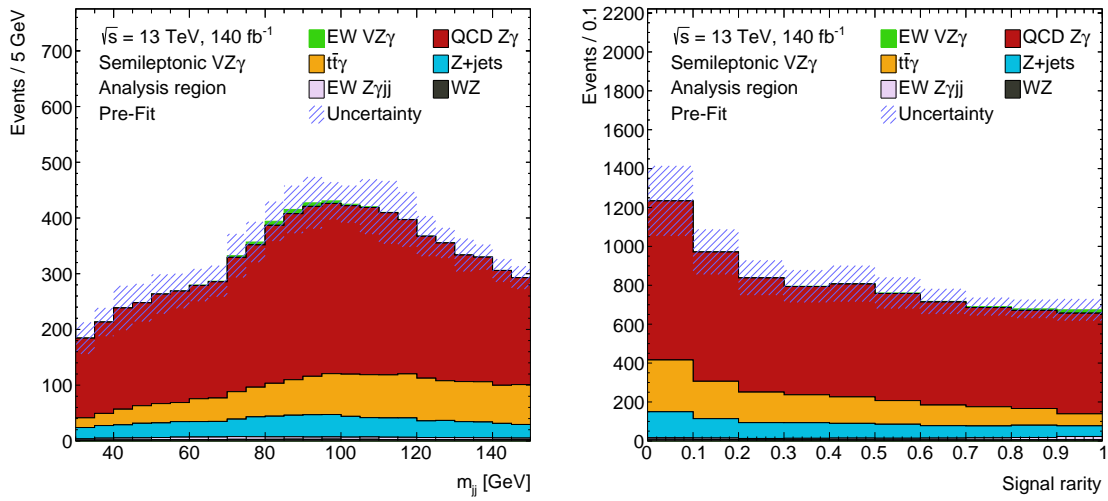


Figure 6.5: Distribution of dijet mass (left) and signal rarity (right) for events in the analysis region, defined by the selection in Table 6.1. Yields for the signal process and all backgrounds are shown stacked atop one another. The error band represents the total pre-fit uncertainty from all sources of systematic uncertainty.

shows this 2D significance scan. A gap is included between the on-peak region and the sidebands to minimise signal leakage; this is chosen such that no more than 5% of the total signal events fall in the sideband regions. Figure 6.7 shows the  $m_{jj}$  cuts employed, in the context of the shape of the signal and background distributions.

## 6.5 Background estimation

This analysis considers the same background processes discussed in Section 4.6: QCD  $Z\gamma$ ,  $Z+jets$ ,  $t\bar{t}\gamma$ , and  $WZjj$ . In addition to these,  $EW Z\gamma jj$  events not matching the signal definition given in Section 6.2.2 are also considered as a background.  $Z+jets$ ,  $t\bar{t}\gamma$ , and  $WZjj$  are all estimated following the procedure in Section 4.6. The QCD  $Z\gamma$  and  $EW Z\gamma jj$  backgrounds are taken directly from their MC estimates.

More complex treatment for the QCD  $Z\gamma$  background was considered, as in the VBS  $Z\gamma$  analysis. However, the phase space of this analysis is not known to be affected by the mismodelling for high dijet masses and Data-MC comparisons, made in the three analysis CRs, show a level of agreement within uncertainties. It is therefore

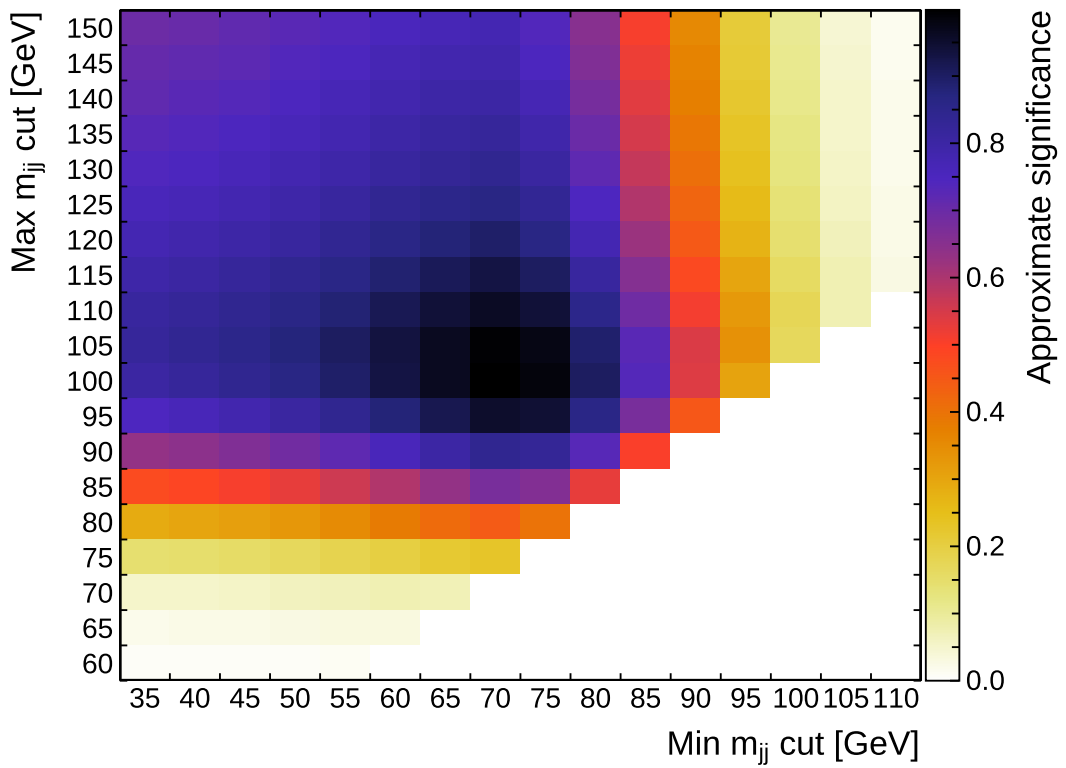


Figure 6.6: Approximate significance calculated with  $s/\sqrt{b}$  for a number of signal events  $s$  and background events  $b$  with an  $m_{jj}$  value between the minimum value given on the  $x$ -axis and the maximum on the  $y$ -axis. The number of signal events is calculated from the EW VZ $\gamma$  sample and all background samples are included for the background estimate. Events are required to pass the analysis region selection from Table 6.1. The maximum significance is obtained for a cut of  $70 < m_{jj} < 100$  GeV.

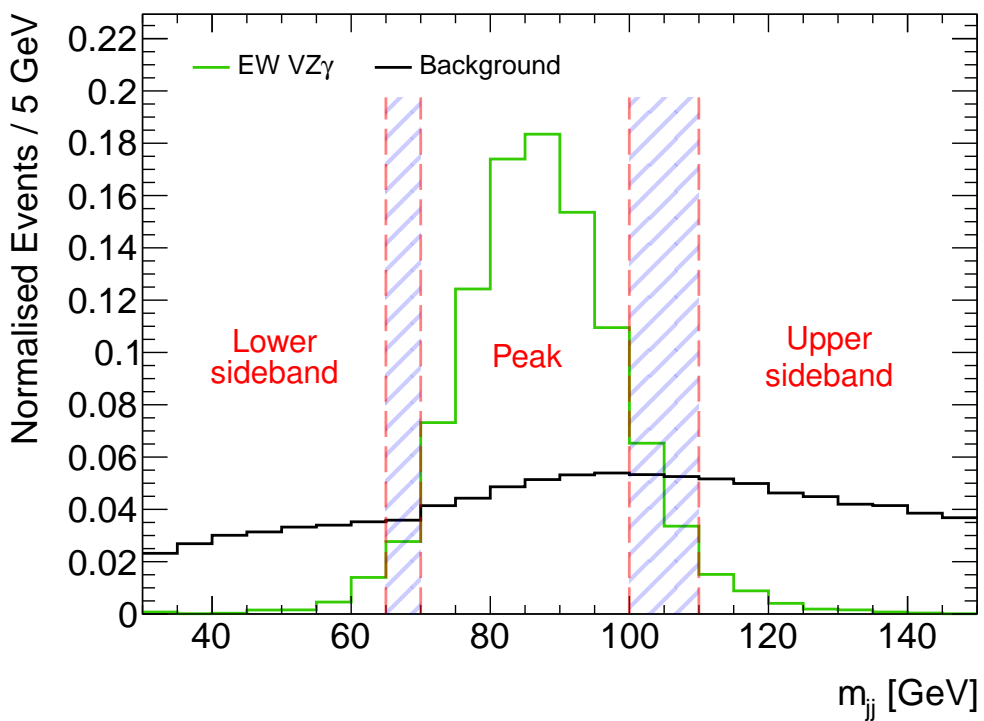


Figure 6.7: Illustration of the three  $m_{jj}$  regions used in the analysis: the lower sideband ( $30 < m_{jj} < 65$  GeV), the upper sideband ( $110 < m_{jj} < 150$  GeV), and the peak ( $70 < m_{jj} < 100$  GeV) region which is then subdivided into the SR and BDT CR. The distributions shown represent events passing the analysis region selection for both the signal (shown in green) and the sum of all backgrounds (in black). Both distributions are normalised by their total event yield.

considered that additional normalisation factors are not necessary, the estimate from MC is sufficient.

## 6.6 Systematic Uncertainties

This analysis considers the sources of systematic uncertainty discussed in Section 4.7. As well as being applied to the signal and QCD  $Z\gamma$  background, full experimental and theory systematic uncertainties are applied for the EW  $Z\gamma jj$  background. A different pruning procedure is used here to the VBS analysis, and is discussed below.

### 6.6.1 Pruning

Given the large number of systematic uncertainties, a pruning procedure is implemented in order to reduce the number of nuisance parameters necessary in the fit. The pruning used for this analysis is less detailed than the one used for the VBS  $Z\gamma$  analysis, it does not rely on statistical uncertainties on the estimates of systematic uncertainties.

Pruning is done individually in each of the four regions used in the fit. The impact of each uncertainty on the normalisation and shape of the signal rarity distribution is considered; shape and normalisation impact are decoupled such that either can be removed if the effect is small. As a result, there are four outcomes for each systematic uncertainty: it is retained in full with normalisation and shape effect, its shape effect is dropped but normalisation kept, its normalisation effect is dropped but shape effect retained, or the uncertainty is dropped entirely.

If the normalisation effect of an uncertainty is retained in the fit, one nuisance parameter is included which allows the uncertainty estimate to be adjusted by the fit, changing the overall normalisation for the associated background or signal estimate. When the shape effect of a systematic uncertainty is used in the fit, per-bin nuisance

parameters are used which allow the yield in each bin to be adjusted by the fit; these per-bin parameters are constrained so as not to affect the overall uncertainty.

The threshold for dropping a normalisation component of an uncertainty is set at 0.2%, i.e. the normalisation is dropped from the fit if its estimated effect on the overall normalisation of the sample is less than 0.2% of the yield. The threshold for dropping a shape component is also set at 99.8%. In this case the is a threshold in the probability of the uncertainty having a different shape to the nominal distribution. The probability is calculated through the Kolmogorov-Smirnov (KS) test [68, 69, 70]; the  $p$ -value given by the test represents compatibility between the nominal and systematic varied distributions. If the  $p$ -value is greater than 0.998 (99.8%) then the differences are considered sufficiently small and the shape component is dropped.

The results of the pruning performed are shown in Figure 6.8, where for each sample, region, and background the treatment of each systematic uncertainty is indicated.

## 6.7 Template fit

The signal process is measured through a fit to the signal rarity distribution in the signal and control regions. The signal strength of EW  $VZ\gamma$ ,  $\mu_{\text{EW}}$ , is the parameter of interest (PoI) in the fit. This parameter follows the definition in Equation 5.3, such that a measured value of  $\mu_{\text{EW}} = 1$  means that the process is measured to occur at rate expected in the SM.

Estimates for each background are used as templates for the fit, and combine with a signal estimate taken from MC to give the total predicted events per-bin in signal rarity. The fit adjusts the value of  $\mu_{\text{EW}}$ , as well as the values of the nuisance parameters representing systematic uncertainties, to best match these templates to the data yield observed in each bin of the distribution.

Four bins are used for the signal rarity distribution in the SR. This binning creates some significant MC statistical uncertainties, but provides a balance between these

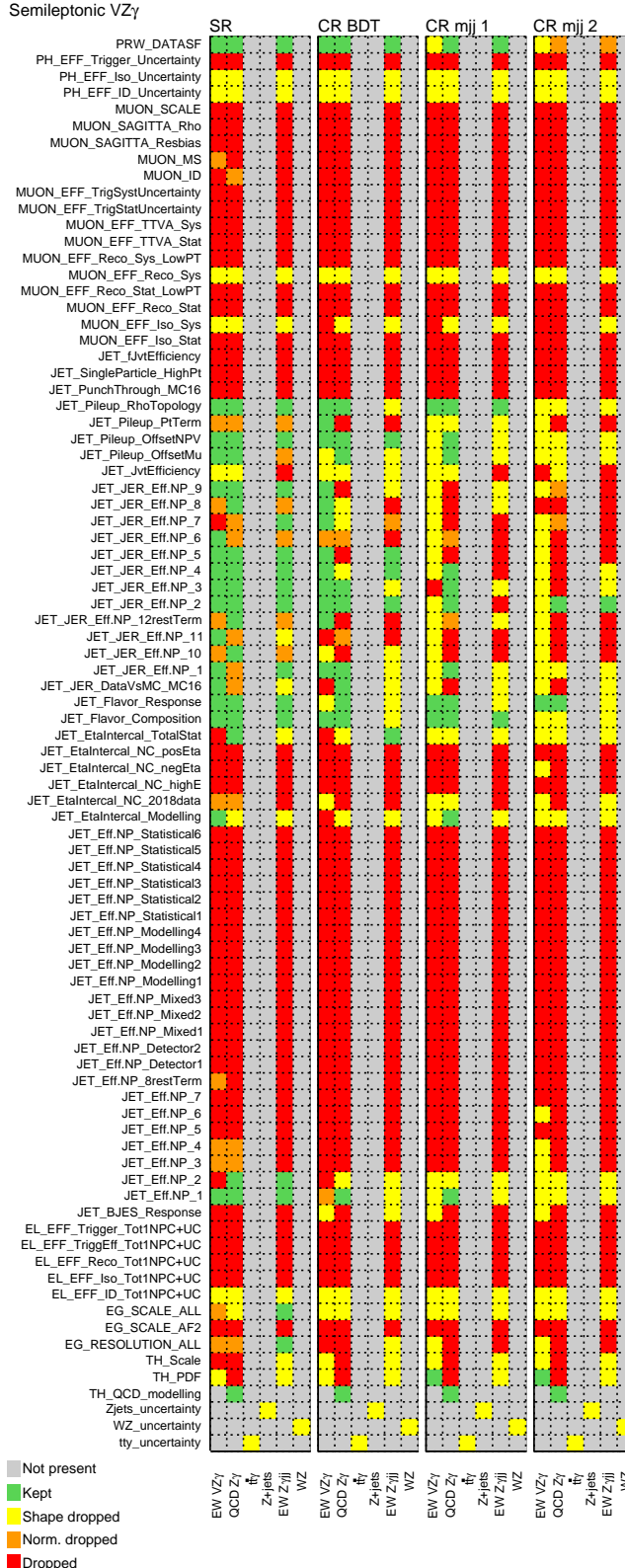


Figure 6.8: Pruning results for systematics in the VZ $\gamma$  analysis. The colours indicate whether a systematic shape and normalisation uncertainty components were each retained for the fit or dropped, for each sample and region used in the fit.

uncertainties and sensitivity to the signal. The low MC statistics is a side effect of the heavily constrained phase space necessary to measure such a low-rate process; these could be reduced by creating larger MC samples or samples weighted towards the relevant phase space, but there was not sufficient time to achieve this.

### 6.7.1 Fitting parameter values

In order to find which values for  $\mu_{\text{EW}}$  and the nuisance parameters give the best agreement with the data, a likelihood model is built. The likelihood is the product of several terms, primarily: a Poisson term for each bin in the fit, describing the probability of obtaining the observed data yield given the estimates from the templates; and a constraint function for each nuisance parameter. Given that each nuisance parameter has only an up variation, down variation, and nominal value, the constraint functions must be interpolated. This is done using a linear interpolation for shape uncertainties and an exponential interpolation for normalisation uncertainties; these interpolations are discussed in Reference [71].

Once constructed, the maximum value for the likelihood must be found. This is achieved by minimising the negative logarithm of the likelihood through the Davidon-Fletcher-Powell approach [72, 73, 74] implemented in Minuit’s MIGRAD algorithm [75]. The values of parameters that minimise the negative log likelihood are taken as the fitted values for the PoI and nuisance parameters. Uncertainties for these parameters are given by the covariance matrix calculated during minimisation. The MINOS technique [75] is used to obtain a more accurate estimate of the uncertainties on  $\mu_{\text{EW}}$ .

### 6.7.2 Fit closure

To test the fitting procedure is stable and self-consistent, a fit is performed using Asimov datasets in all regions. This pseudo-data setup runs the fit with ‘data’ yields

equal to the total expected MC yield in all regions. By construction, this should give a fitted value of  $\mu_{\text{EW}} = 1$ ; any significant deviation would indicate a problem with the fit. This Asimov-only fit produces the result

$$\mu_{\text{EW}} = 0.9994 \pm 1.1272,$$

deviating only slightly from 1 and thus not indicating any issues.

### 6.7.3 Mixed fit

In order to estimate the full sensitivity of the analysis without using observed data in the SR, a mixed data-Asimov fit is used: here the observed data yields are used in the three CRs and an Asimov dataset in the SR. This Asimov dataset is generated by first performing a fit to data in the CRs with the value of  $\mu_{\text{EW}}$  fixed to 1. This allows the values of the systematic uncertainties to vary and account for any small data-MC discrepancies. The post-fit values for these parameters are then used in the estimate for the number of events in the SR used for the Asimov data.

The results of this fit represent the SM expectation for the analysis results, and thus demonstrate the sensitivity. Full expected results are presented in Section 6.8 alongside the observed results.

Running this mixed fit gives a fitted value for the  $\mu_{\text{EW}}$  parameter of

$$\begin{aligned} \mu_{\text{EW}} &= 1.599^{+1.204}_{-1.149} \\ &= 1.599^{+0.945}_{-0.915} (\text{stat.})^{+0.677}_{-0.632} (\text{syst.})^{+0.313}_{-0.288} (\text{MC stat.}) \end{aligned} \tag{6.2}$$

where the component of the error from MC statistics has been factored out of the systematic uncertainty (for this instance only). This result shows an apparent deviation from the expected SM value of  $\mu_{\text{EW}} = 1$ , despite not including data in the SR. This bias may be introduced by the large MC statistical uncertainties, with their contribution to the total uncertainty indicated in Equation 6.2. It may be

possible to correct for this effect, but there was not sufficient time to gain a sufficient understanding as to be able to assign an uncertainty to this correction. For the purposes of this analysis, this  $\mu_{\text{EW}}$  value is considered an upward fluctuation of the MC statistical error (compatible at the  $\sim 2\sigma$  level) and thus consistent with the expectation.

#### 6.7.4 Data fit

Once the SR is unblinded, the fit can be performed using observed data yields in all four regions. As with the mixed fit, the  $\mu_{\text{EW}}$  value and all nuisance parameters are minimised simultaneously across all regions, allowing their values to be constrained by data in CRs as well as the SR. Results from this fit are presented in Section 6.8.

### 6.8 Results

The signal strength for EW VZ $\gamma$  measured from the full fit is

$$\begin{aligned}\mu_{\text{EW}} &= 1.406^{+1.195}_{-1.142} \\ &= 1.406^{+0.930}_{-0.901} \text{ (stat.)}^{+0.750}_{-0.701} \text{ (syst.)},\end{aligned}$$

and is compatible with the SM expectation. Post-fit distributions in the four regions are shown in Figure 6.9.

The observed significance of the signal process is 1.24 standard deviations, from an expected significance of 1.40 standard deviations. This does not meet the threshold to provide evidence on the existence of the process. Instead a limit is set on the rate of production for signal events at 3.46 times the SM expectation. This can be used to constrain any new physics models that would enhance the cross-section for triboson VZ $\gamma$  production.

Statistical uncertainties make the largest contribution to the measurement, but sys-

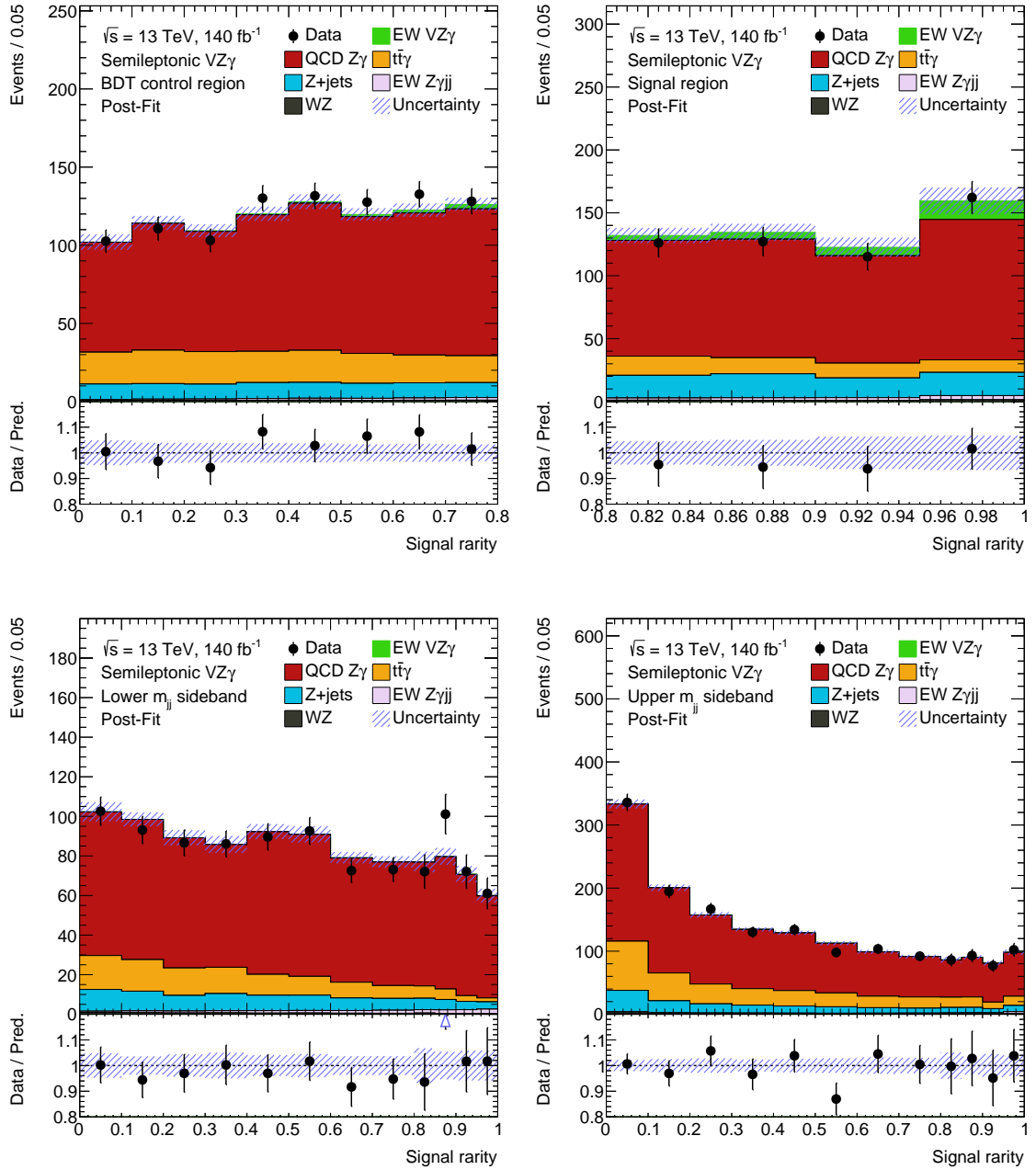


Figure 6.9: Post-fit signal rarity distributions in each of the four regions used in the fit, as labelled. Uncertainty bands represent the combined uncertainties in each bin, with values constrained by the fit.

tematic uncertainties make a significant contribution. The largest systematic contributions are shown in Figure 6.10. Pileup reweighting is the largest individual contribution, likely due to the limited data statistics (see Section 6.9). Section 4.7 discusses the origin of pileup reweighting uncertainties. The second largest contribution is from jet flavour composition. This uncertainty is reducible, as was done for the VBS  $Z\gamma$  analysis, but there was not sufficient time to implement it for this analysis. Several more of the largest uncertainties are MC statistics uncertainties in signal bins; these are also reducible given large MC samples. The effect of reducing some of these systematic uncertainties is discussed in Section 6.9.

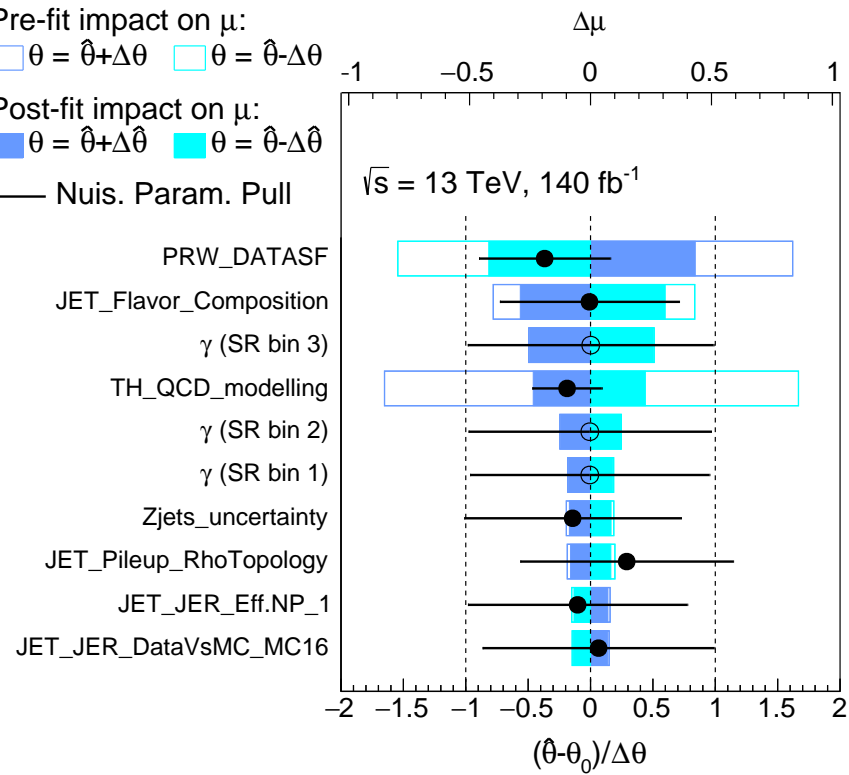


Figure 6.10: Systematic uncertainties ranked by their post-fit impact on  $\mu_{EW}$ . Uncertainties labelled  $\gamma$  represent MC statistics uncertainties in the given bin.

## 6.9 Projected results

To test what sensitivity might be possible with more time or data available for this analysis, projected future results are explored. Firstly the reducible uncertainties,

jet flavour composition and response and MC statistics, are removed. This simulates processing larger datasets, to reduce MC statistics uncertainties, and including gluon fraction information, to reduce jet flavour uncertainties. With the existing analysis and dataset this would give a measurement of

$$\mu_{\text{EW}} = 1.43 \pm 1.08,$$

calculated from performing a fit without these uncertainties included.

This is a small improvement by itself, but combined with an expanded dataset this could greatly enhance sensitivity. By scaling up the luminosity of the templates in the fit, performing the analysis with a larger dataset can be simulated. This is a naïve estimate as with a significantly larger dataset the analysis would need to be re-optimised to take advantage of the available data.

To estimate sensitivity possible with a Run 2 and Run 3 combined dataset, templates are scaled to a luminosity of  $420 \text{ fb}^{-1}$ . The measured signal strength from this fit is

$$\begin{aligned}\mu_{\text{EW}} &= 1.00 \pm 0.63 \\ &= 1.00 \pm 0.53 \text{ (stat.)} \pm 0.35 \text{ (syst.)},\end{aligned}$$

corresponding to a significance of 2.09 standard deviations. This still falls short of the evidence threshold of 3 standard deviations. Whilst proper optimisation for the larger dataset might make obtaining evidence achievable, the initial indication would be that additional data beyond Run 3 will be needed to reach the  $3\sigma$  threshold.

The largest systematic uncertainties for the  $420 \text{ fb}^{-1}$  projected fit are shown in Figure 6.11. It is noticeably that pileup reweighting is still the dominant systematic uncertainty, but much reduced from its post-fit scale seen in Figure 6.10. Indeed running fits with luminosities scaled even higher sees further reduction in the impact of this uncertainty; likely it is so dominant for the current analysis because of the limited statistics in the phase space.

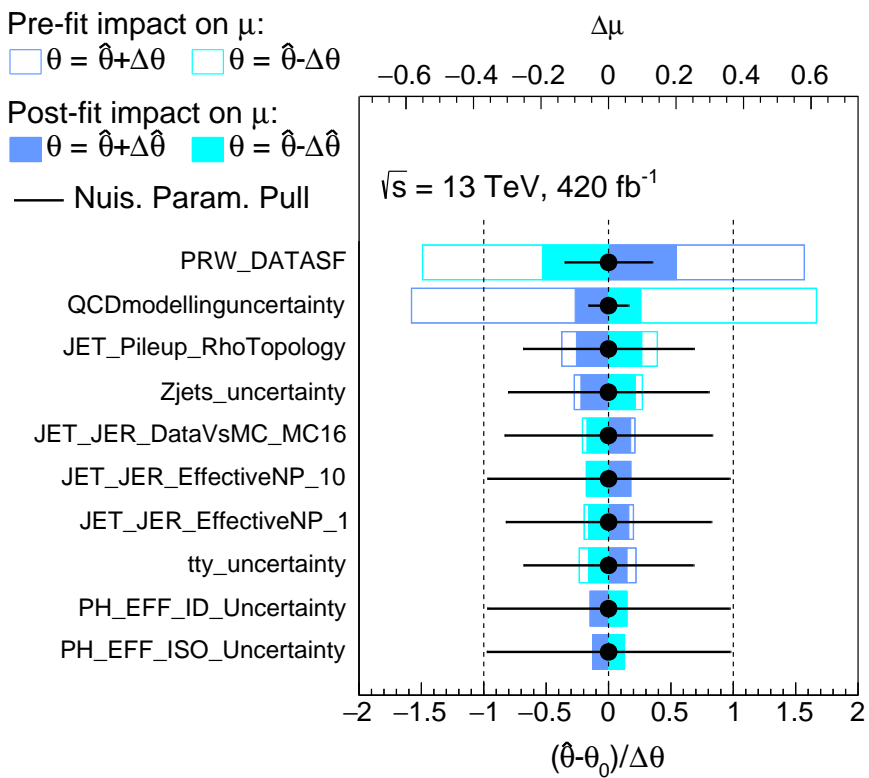


Figure 6.11: Systematic uncertainties ranked by their post-fit impact on  $\mu_{\text{EW}}$ , for a projected fit scaled to a luminosity of  $420 \text{ fb}^{-1}$ . Uncertainties from MC statistics and jet flavour were removed from this fit.

---

## Conclusions

---

---

## REFERENCES

---

- [1] S. Weinberg. *The Quantum Theory of Fields*, volume 1. Cambridge University Press, Cambridge, first edition (1995). ISBN 0521550017.
- [2] P. A. M. Dirac. *A theory of electrons and protons*. Proc. R. Soc. London. Ser. A, Contain. Pap. a Math. Phys. Character 126(801) (Jan 1930) pp. 360–365. ISSN 0950-1207. <http://dx.doi.org/10.1098/rspa.1930.0013>.
- [3] W. Pauli. *Über den Zusammenhang des Abschlusses der Elektronengruppen im Atom mit der Komplexstruktur der Spektren*. Zeitschrift für Phys. 31(1) (Feb 1925) pp. 765–783. ISSN 00443328. <http://dx.doi.org/10.1007/BF02980631>.
- [4] V. F. Weisskopf. *The development of field theory in the last 50 years*. Phys. Today 34(11) (Nov 1981) pp. 69–85. ISSN 19450699. <http://dx.doi.org/10.1063/1.2914365>.
- [5] M. Thomson. *Modern Particle Physics*. Cambridge University Press, Cambridge, first edition (2013). ISBN 9781107034266.
- [6] M. Gell-Mann. *The eightfold way: A theory of strong interaction symmetry* (1961). <http://dx.doi.org/10.2172/4008239>.
- [7] M. E. Peskin and D. V. Schroeder. *An Introduction to Quantum Field Theory* (1995).
- [8] C. N. Yang and R. L. Mills. *Conservation of isotopic spin and isotopic gauge invariance*. Phys. Rev. 96(1) (Oct 1954) pp. 191–195. ISSN 0031899X. <http://dx.doi.org/10.1103/PhysRev.96.191>.

- [9] Particle Data Group. *Review of Particle Physics – Quantum Chromodynamics*. Prog. Theor. Exp. Phys. 2022 (2022) p. 083C01. <http://dx.doi.org/10.1093/ptep/ptac097>.
- [10] M. Thomson. *Modern Particle Physics – Errata* (2018). [https://www.hep.phy.cam.ac.uk/\\$\sim\\$thomson/MPP/ModernParticlePhysics\\_Errata.pdf](https://www.hep.phy.cam.ac.uk/$\sim$thomson/MPP/ModernParticlePhysics_Errata.pdf).
- [11] R. D. Ball et al. *Parton distributions from high-precision collider data*. Eur. Phys. J. C 2017 7710 77(10) (Oct 2017) pp. 1–75. ISSN 1434-6052. <http://dx.doi.org/10.1140/EPJC/S10052-017-5199-5>.
- [12] J. Alwall et al. *The automated computation of tree-level and next-to-leading order differential cross sections, and their matching to parton shower simulations*. J. High Energy Phys. 2014 20147 2014(7) (Jul 2014) pp. 1–157. ISSN 1029-8479. [http://dx.doi.org/10.1007/JHEP07\(2014\)079](http://dx.doi.org/10.1007/JHEP07(2014)079). 1405.0301.
- [13] E. Bothmann et al. *Event generation with Sherpa 2.2*. SciPost Phys. 7(3) (Sep 2019) p. 034. ISSN 25424653. <http://dx.doi.org/10.21468/SCIPOSTPHYS.7.3.034/PDF>. 1905.09127.
- [14] T. Sjöstrand et al. *An introduction to PYTHIA 8.2*. Comput. Phys. Commun. 191(1) (Jun 2015) pp. 159–177. ISSN 0010-4655. <http://dx.doi.org/10.1016/J.CPC.2015.01.024>. 1410.3012.
- [15] S. Frixione, P. Nason, and C. Oleari. *Matching NLO QCD computations with parton shower simulations: The POWHEG method*. J. High Energy Phys. 2007(11) (Nov 2007) p. 070. ISSN 11266708. <http://dx.doi.org/10.1088/1126-6708/2007/11/070>. 0709.2092.
- [16] M. Bähr et al. *Herwig++ physics and manual*. Eur. Phys. J. C 2008 584 58(4) (Nov 2008) pp. 639–707. ISSN 1434-6052. <http://dx.doi.org/10.1140/EPJC/S10052-008-0798-9>. 0803.0883.
- [17] B. Andersson et al. *Parton fragmentation and string dynamics*. Phys. Rep. 97(2-3) (Jul 1983) pp. 31–145. ISSN 0370-1573. [http://dx.doi.org/10.1016/0370-1573\(83\)90080-7](http://dx.doi.org/10.1016/0370-1573(83)90080-7).
- [18] S. Agostinelli et al. *Geant4—a simulation toolkit*. Nucl. Instruments Methods Phys. Res. Sect. A Accel. Spectrometers, Detect. Assoc. Equip. 506(3) (Jul 2003) pp. 250–303. ISSN 0168-9002. [http://dx.doi.org/10.1016/S0168-9002\(03\)01368-8](http://dx.doi.org/10.1016/S0168-9002(03)01368-8).
- [19] The ATLAS Collaboration. *The ATLAS Simulation Infrastructure*. Eur. Phys. J. C 70(3) (Sep 2010) pp. 823–874. ISSN 14346052. <http://dx.doi.org/10.1140/epjc/s10052-010-1429-9>. 1005.4568.
- [20] O. S. Brüning et al. *LHC Design Report Vol. I: The LHC Main Ring*. CERN Yellow Reports: Monographs. CERN, Geneva (2004). <http://dx.doi.org/10.5170/CERN-2004-003-V-1>.

- [21] O. S. Brüning et al. *LHC Design Report Vol. II: The LHC infrastructure and general services*. CERN Yellow Reports: Monographs. CERN, Geneva (2004). <http://dx.doi.org/10.5170/CERN-2004-003-V-2>.
- [22] M. Benedikt et al. *LHC Design Report Vol. III: The LHC injector chain*. CERN Yellow Reports: Monographs. CERN, Geneva (2004). <http://dx.doi.org/10.5170/CERN-2004-003-V-3>.
- [23] R. Assmann, M. Lamont, and S. Myers. *A Brief History of the LEP Collider*. Nucl. Phys. B, Proc. Suppl. 109(2-3) (Apr 2002) pp. 17–31. ISSN 09205632. [http://dx.doi.org/10.1016/S0920-5632\(02\)90005-8](http://dx.doi.org/10.1016/S0920-5632(02)90005-8).
- [24] The ATLAS Collaboration. *Observation of a new particle in the search for the Standard Model Higgs boson with the ATLAS detector at the LHC*. Phys. Lett. B 716(1) (Sep 2012) pp. 1–29. ISSN 0370-2693. <http://dx.doi.org/10.1016/J.PHYSLETB.2012.08.020>. [1207.7214](#).
- [25] The CMS Collaboration. *Observation of a new boson at a mass of 125 GeV with the CMS experiment at the LHC*. Phys. Lett. B 716(1) (Sep 2012) pp. 30–61. ISSN 0370-2693. <http://dx.doi.org/10.1016/J.PHYSLETB.2012.08.021>. [1207.7235](#).
- [26] The CMS Collaboration. *Observation of a new boson with mass near 125 GeV in pp collisions at  $\sqrt{s} = 7$  and 8 TeV*. J. High Energy Phys. 2013 2013(6) (Jun 2013) pp. 1–127. ISSN 1029-8479. [http://dx.doi.org/10.1007/JHEP06\(2013\)081](http://dx.doi.org/10.1007/JHEP06(2013)081). [1303.4571](#).
- [27] E. Mobs. *The CERN accelerator complex - August 2018*. CERN (Aug 2018). <https://cds.cern.ch/record/2636343>.
- [28] R. Ostojic. *The LHC insertion magnets*. In *IEEE Trans. Appl. Supercond.* CERN (Mar 2002), volume 12. ISSN 10518223, pp. 196–201. <http://dx.doi.org/10.1109/TASC.2002.1018382>.
- [29] R. Steerenberg et al. *Operation and performance of the CERN Large Hadron Collider during proton Run 2*. 10th Int. Part. Accel. Conf. (10) (2019) pp. 504–507. <http://dx.doi.org/10.18429/JACoW-IPAC2019-MOPMP031>.
- [30] The ATLAS Collaboration. *The ATLAS Experiment at the CERN Large Hadron Collider*. J. Instrum. 3(08) (Aug 2008) p. S08,003. ISSN 1748-0221. <http://dx.doi.org/10.1088/1748-0221/3/08/S08003>.
- [31] The ATLAS Collaboration. *Performance of the ATLAS Track Reconstruction Algorithms in Dense Environments in LHC Run 2*. Eur. Phys. J. C 77(10) (Apr 2017) p. 673. <http://dx.doi.org/10.1140/epjc/s10052-017-5225-7>. [1704.07983](#).
- [32] M. Capeans et al. *ATLAS Insertable B-Layer Technical Design Report* (Sep 2010). <https://cds.cern.ch/record/1291633>.

- [33] J. Pequenao. *Computer Generated image of the ATLAS calorimeter* (Mar 2008). <https://cds.cern.ch/record/1095927>.
- [34] J. Pequenao. *Computer generated image of the ATLAS Muons subsystem* (Mar 2008). <https://cds.cern.ch/record/1095929>.
- [35] The ATLAS Collaboration. *Operation of the ATLAS trigger system in Run 2*. J. Instrum. 15(10) (Oct 2020) p. P10,004. ISSN 1748-0221. <http://dx.doi.org/10.1088/1748-0221/15/10/P10004>.
- [36] R. Achenbach et al. *The ATLAS Level-1 Calorimeter Trigger*. J. Instrum. 3(03) (Mar 2008). ISSN 1748-0221. <http://dx.doi.org/10.1088/1748-0221/3/03/P03001>.
- [37] G. Avoni et al. *The new LUCID-2 detector for luminosity measurement and monitoring in ATLAS*. J. Instrum. 13(07) (Jul 2018). ISSN 1748-0221. <http://dx.doi.org/10.1088/1748-0221/13/07/P07017>.
- [38] G. Aad et al. *ATLAS data quality operations and performance for 2015-2018 data-taking*. J. Instrum. 15(4) (Apr 2020). ISSN 1748-0221. <http://dx.doi.org/10.1088/1748-0221/15/04/P04003>. [1911.04632](https://arxiv.org/abs/1911.04632).
- [39] The ATLAS Collaboration. *Luminosity determination in pp collisions at  $\sqrt{s} = 13 \text{ TeV}$  using the ATLAS detector at the LHC* (Jun 2019). <https://cds.cern.ch/record/2677054>.
- [40] I. Brawn. *L1Calo Overview, Status, Installation & Commissioning* (Oct 2019). <https://indico.cern.ch/event/829769/contributions/3572289>. [ATLAS Internal].
- [41] The ATLAS Collaboration. *Technical Design Report for the Phase-I Upgrade of the ATLAS TDAQ System*. Technical Report ATLAS-TDR-023-2013 (2013). [http://cds.cern.ch/record/1602235/](https://cds.cern.ch/record/1602235/).
- [42] The ATLAS Collaboration. *Technical Design Report for the Phase-II Upgrade of the ATLAS TDAQ System*. Technical Report ATLAS-TDR-029, CERN, Geneva (2017). <https://cds.cern.ch/record/2285584>.
- [43] T. Sjöstrand, S. Mrenna, and P. Skands. *A brief introduction to PYTHIA 8.1*. Comput. Phys. Commun. 178(11) (Jun 2008) pp. 852–867. ISSN 00104655. <http://dx.doi.org/10.1016/j.cpc.2008.01.036>. [0710.3820](https://arxiv.org/abs/0710.3820).
- [44] The ATLAS Collaboration. *Performance of electron and photon triggers in ATLAS during LHC Run 2*. Eur. Phys. J. C 80(1) (Jan 2020) pp. 1–41. ISSN 1434-6052. <http://dx.doi.org/10.1140/EPJC/S10052-019-7500-2>. [1909.00761](https://arxiv.org/abs/1909.00761).
- [45] The ATLAS Collaboration. *Performance of the ATLAS muon triggers in Run 2*. J. Instrum. 15(09) (Sep 2020). ISSN 1748-0221. <http://dx.doi.org/10.1088/1748-0221/15/09/P09015>.

- [46] J. Bellm et al. *Herwig++ 2.7 Release Note* (Oct 2013). <http://dx.doi.org/10.48550/arXiv.1310.6877>. [1310.6877](https://arxiv.org/abs/1310.6877).
- [47] R. D. Ball et al. *Parton distributions for the LHC run II*. J. High Energy Phys. 2015 20154 2015(4) (Apr 2015) pp. 1–148. ISSN 1029-8479. [http://dx.doi.org/10.1007/JHEP04\(2015\)040](http://dx.doi.org/10.1007/JHEP04(2015)040). [1410.8849](https://arxiv.org/abs/1410.8849).
- [48] P. Nason. *A new method for combining NLO QCD with shower Monte Carlo algorithms*. J. High Energy Phys. 8(11) (Dec 2004) pp. 1097–1124. ISSN 10298479. <http://dx.doi.org/10.1088/1126-6708/2004/11/040>. [0409146](https://arxiv.org/abs/0409146).
- [49] S. Alioli et al. *A general framework for implementing NLO calculations in shower Monte Carlo programs: The POWHEG BOX*. J. High Energy Phys. 2010(6) (Jun 2010) pp. 1–58. ISSN 10298479. [http://dx.doi.org/10.1007/JHEP06\(2010\)043](http://dx.doi.org/10.1007/JHEP06(2010)043). [1002.2581](https://arxiv.org/abs/1002.2581).
- [50] H. L. Lai et al. *New parton distributions for collider physics*. Phys. Rev. D - Part. Fields, Gravit. Cosmol. 82(7) (Oct 2010) p. 074,024. ISSN 15507998. <http://dx.doi.org/10.1103/PhysRevD.82.074024>. [1007.2241](https://arxiv.org/abs/1007.2241).
- [51] The ATLAS Collaboration. *Measurement of the  $Z/\gamma^*$  boson transverse momentum distribution in  $pp$  collisions at  $\sqrt{s} = 7$  TeV with the ATLAS detector*. J. High Energy Phys. 2014(9) (Sep 2014) pp. 1–47. ISSN 10298479. [http://dx.doi.org/10.1007/JHEP09\(2014\)145](http://dx.doi.org/10.1007/JHEP09(2014)145). [METRICS. 1406.3660](https://arxiv.org/abs/1406.3660).
- [52] R. D. Ball et al. *Parton distributions with LHC data*. Nucl. Phys. B 867(2) (Feb 2013) pp. 244–289. ISSN 05503213. <http://dx.doi.org/10.1016/j.nuclphysb.2012.10.003>. [1207.1303](https://arxiv.org/abs/1207.1303).
- [53] The ATLAS Collaboration. *The Pythia8 A3 tune description of ATLAS minimum bias and inelastic measurements incorporating the Donnachie-Landshoff diffractive model*. ATL-PHYS-PUB-2016-017 (Aug 2016). <https://cds.cern.ch/record/2206965><https://inspirehep.net/record/1477266>.
- [54] The ATLAS Collaboration. *Electron and photon energy calibration with the ATLAS detector using 2015–2016 LHC proton-proton collision data*. J. Instrum. 14(03) (Mar 2019) p. P03,017. ISSN 1748-0221. <http://dx.doi.org/10.1088/1748-0221/14/03/P03017>. [1812.03848](https://arxiv.org/abs/1812.03848).
- [55] The ATLAS Collaboration. *Photon identification in 2015 ATLAS data* (Aug 2016). <https://cds.cern.ch/record/2203125>.
- [56] The ATLAS Collaboration. *Electron reconstruction and identification in the ATLAS experiment using the 2015 and 2016 LHC proton-proton collision data at  $\sqrt{s} = 13$  TeV*. Eur. Phys. J. C 79(8) (Feb 2019). <http://dx.doi.org/10.1140/epjc/s10052-019-7140-6>. [1902.04655v2](https://arxiv.org/abs/1902.04655v2).
- [57] The ATLAS Collaboration. *Muon reconstruction and identification efficiency in ATLAS using the full Run 2  $pp$  collision data set at  $\sqrt{s} = 13$  TeV*. Eur.

- Phys. J. C 2021 817 81(7) (Jul 2021) pp. 1–44. ISSN 1434-6052. <http://dx.doi.org/10.1140/EPJC/S10052-021-09233-2>. 2012.00578.
- [58] M. Cacciari, G. P. Salam, and G. Soyez. *The anti- $kt$  jet clustering algorithm*. J. High Energy Phys. 2008(04) (Apr 2008) p. 063. ISSN 1126-6708. <http://dx.doi.org/10.1088/1126-6708/2008/04/063>. 0802.1189.
- [59] The ATLAS Collaboration. *Topological cell clustering in the ATLAS calorimeters and its performance in LHC Run 1*. Eur. Phys. J. C 77(7) (2017) p. 490. ISSN 1434-6052. <http://dx.doi.org/10.1140/epjc/s10052-017-5004-5>.
- [60] The ATLAS Collaboration. *Jet reconstruction and performance using particle flow with the ATLAS Detector*. Eur. Phys. J. C 77(7) (2017) p. 466. ISSN 1434-6052. <http://dx.doi.org/10.1140/epjc/s10052-017-5031-2>.
- [61] The ATLAS Collaboration. *Jet energy scale measurements and their systematic uncertainties in proton-proton collisions at  $\sqrt{s} = 13$  TeV with the ATLAS detector* (2017). <http://dx.doi.org/10.1103/PhysRevD.96.072002>.
- [62] The ATLAS Collaboration. *Light-quark and Gluon Jets in ATLAS: Calorimeter Response, Jet Energy Scale Systematics, and Sample Characterization* (Mar 2011).
- [63] The ATLAS Collaboration. *Measurement of the cross-sections of the electroweak and total production of a  $Z\gamma$  pair in association with two jets in  $pp$  collisions at  $\sqrt{s} = 13$  TeV with the ATLAS detector* (Jul 2023). <http://cds.cern.ch/record/2779171><http://arxiv.org/abs/2305.19142>. 2305.19142.
- [64] B. Efron. *Computers and the Theory of Statistics: Thinking the Unthinkable*. SIAM Rev. 21(4) (Oct 1979) pp. 460–480. ISSN 0036-1445. <http://dx.doi.org/10.1137/1021092>.
- [65] B. Efron. *Better Bootstrap Confidence Intervals*. J. Am. Stat. Assoc. 82(397) (Mar 1987) p. 171. ISSN 01621459. <http://dx.doi.org/10.2307/2289144>.
- [66] S. S. Wilks. *The Large-Sample Distribution of the Likelihood Ratio for Testing Composite Hypotheses*. Ann. Math. Stat. 9(1) (Mar 1938) pp. 60–62. ISSN 0003-4851. <http://dx.doi.org/10.1214/aoms/1177732360>.
- [67] J. C. Collins and D. E. Soper. *Angular distribution of dileptons in high-energy hadron collisions*. Phys. Rev. D 16(7) (Oct 1977) pp. 2219–2225. ISSN 05562821. <http://dx.doi.org/10.1103/PhysRevD.16.2219>.
- [68] A. Kolmogoroff. *Sulla determinazione empirica di una legge di distribuzione*. G. dell’Istituto Ital. degli Attuari 4 (1933) pp. 83–91.
- [69] N. Smirnov. *Sur les écarts de la courbe de distribution empirique*. Recl. Mathématique [ Mat. Sb. ] 6(48) (1939) pp. 3–26.

- [70] F. J. Massey. *The Kolmogorov-Smirnov Test for Goodness of Fit*. J. Am. Stat. Assoc. 46(253) (Mar 1951) p. 68. ISSN 01621459. <http://dx.doi.org/10.2307/2280095>.
- [71] K. Cranmer et al. *HistFactory: A tool for creating statistical models for use with RooFit and RooStats* (Jan 2012). <https://cds.cern.ch/record/1456844>.
- [72] W. C. Davidon. *Variable metric method for minimization* (May 1991). <http://dx.doi.org/10.1137/0801001>.
- [73] R. Fletcher. *New approach to variable metric algorithms*. Comput. J. 13(3) (Jan 1970) pp. 317–322. ISSN 00104620. <http://dx.doi.org/10.1093/comjnl/13.3.317>.
- [74] M. J. D. Powell. *Variable Metric Methods for Constrained Optimization*. In *Math. Program. State Art*, Springer, Berlin, Heidelberg (1983). ISBN 978-3-642-68874-4, pp. 288–311. [http://dx.doi.org/10.1007/978-3-642-68874-4\\_12](http://dx.doi.org/10.1007/978-3-642-68874-4_12).
- [75] F. James and M. Winkler. *Minuit2* (2004). <https://root.cern.ch/root/html/doc/guides/minuit2/Minuit2.html>.

